GE QUANTUM DOT FORMATION ON THE CARBON-ALLOYED SILICON (001) SURFACE - A SCANNING TUNNELING MICROSCOPY STUDY

PAR

Oliver LEIFELD

Diplom-Physiker, Universität Gesamthochschule Paderborn, Allemagne
de nationalité allemande

Version abrégée

Les microscopes à effet tunnel (MET, STM en anglais), appliqués à l'observation d'échantillons minces et de grandes tailles, sont souvent mécaniquement instables en raison des résonances propres à basses fréquences du système. Cependant, dans le domaine de l'épitaxie de semi-conducteur, les substrats standards présentent au minimum un diamètre de 4-pouces et une épaisseur excédant rarement 0.5 mm.

Afin de profiter de la technique de microscopie à effet tunnel en dépit de cette difficulté, nous avons construit, dans le cadre de cette thèse, un puissant MET à ultra-haut vide. L'instrument, optimisé pour des substrats 4-pouces, est monté aux cotés d'un système de déposition par épitaxie existant et a été appliqué avec succès à l'étude de la croissance de nanostructures de Ge sur du Si(001) et du Si(001) recouvert avec du carbone. La résolution atomique a été atteinte.

Nous avons étudié les étapes initiales de l'incorporation de carbone dans la surface de Si(001). La déposition de 0.05 à 0.2 monocouche (MC, ML en anglais) de carbone provoque la formation de domaines reconstruits c(4×4). Les images obtenues par le MET, des calculs de densité, ainsi que des simulations de l'énergie totale et de la stabilité thermodynamique révèlent, ensemble, la structure de la reconstruction c(4×4).

La formation consécutives d'îlots de Ge sur une surface de C / Si(001) est étudiée avec une résolution atomique jusqu'à une épaisseur de 6 MC de Ge. Contrairement au mode de croissance dominant sur du Si(001) pur, nous observons la croissance d'îles multicouches au dessous de 1 MC de Ge déjà. Le mode de croissance dominant est du type Volmer-Weber. La répulsion entre le Ge et le C empêche la formation d'une couche de mouillage bi-dimensionnelle (2-D) de Ge dans ce système, et favorise la création d'îlots 3-D (< 10 nm).

Entre 2.5 et 4 MC Ge le MET révèle une forte densité (10^{11} cm^{-2}) d'îlots de Ge non-facettés, de formes irrégulières et ayant des tailles variant entre 10 et 25 nm. L'impact de la température du substrat, de l'épaisseur de Ge et de l'épaisseur de C sur la formation des îlots est étudié grâce à la microscopie électronique par transmission sur des échantillons recouverts par une mince couche de silicium. Des spectres de photoluminescence (PL) indiquent une forte corrélation entre les propriétés structurales et optiques. La présence de points quantiques provoque, pour des épaisseurs de Ge variant de 2.5 à 3 ML sur 0.1 MC C / Si(001), une intense luminescence due à des transitions optiques. Cependant, la recombinaison Auger s'avère le processus dominant.

Au-dessus de 5 MC, les îlots de Ge déposés sur du C / Si(001) présentent une forme plus régulière grâce à la formation de facettes {105}. La densité de ces îlots, dont la forme

ressemble à des 'hut-clusters' dotés d'une facette supérieure plate, est 20 fois plus grande que celle obtenue lors de la croissance sur du Si pur. L'étude détaillée de la nucléation et de la croissance du Ge sur du C / Si(001) ouvre de nouvelles perspectives pour la fabrication de points quantiques de très petites tailles. Des applications optoélectroniques basées sur le Si semblent envisageables.

Abstract

Scanning tunneling microscope (STM) experiments on large and thin samples are often not stable due to the voluminous setup and the inherently low sample Eigenfrequencies. In semiconductor epitaxy, however, a standard substrate has at least a diameter of 4-inch and the thickness rarely exceeds 0.5 mm.

To take advantage of the STM technique despite this difficulty, a powerful ultra-high vacuum STM for 4-inch wafers has been realized in the framework of this thesis. The microscope is combined with an existing multipurpose epitaxy system and has been successfully applied to study the growth of Ge nanostructures on clean and carbon covered Si(001) surfaces down to atomic resolution.

The initial stages of sub-monolayer carbon incorporation into the Si(001) surface have been investigated. Carbon deposition of 0.05 to 0.2 monolayers (ML) induces the formation of carbon-containing c(4×4) reconstructed domains. Based on the STM images, density functional theory calculations, as well as total energy and thermal stability simulations, the atomic structure of the C-induced c(4×4) is uncovered.

Subsequently, Ge island formation on this C / Si(001) surface is investigated with atomic resolution for coverages up to 6 ML. In contrast to growth on bare Si(001), multilayer islands are already observed at submonolayer coverages, indicating, that the growth mode is of the Volmer-Weber type. Due to the repelling interaction between Ge and C, Ge does not form any two dimensional wetting layer like it is observed on bare Si(001), but small 3D islands (<10 nm) nucleate instead.

Between 2.5 and 4 ML Ge, STM images reveal a high density (10^{11} cm^{-2}) of irregularly shaped, non-faceted Ge islands, having sizes between 10 and 25 nm. Related experiments using cross-sectional transmission electron microscopy on Si capped samples show, how the substrate temperature, the Ge thickness and the amount of C predeposition affect the dot formation. A strong correlation between the morphological and optical properties is demonstrated by photoluminescence (PL) spectroscopy. PL spectra exhibit intense luminescence related to radiative transitions due to the presence of dots for Ge coverages of 2.5 to 3 ML on 0.1 ML C / Si(001). However, Auger recombination is found to be dominant in the dot samples.

At coverages above 5 ML the Ge islands on C / Si(001) become more regular in shape by {105}-facet formation. The density of these islands, whose shape is similar to 'hut clusters' with a flat top facet, is 20 times higher compared to Ge on bare Si(001) grown under identical conditions.

The detailed nucleation study of Ge on C / Si(001) points out new routes towards the fabrication of ultra small Ge quantum dots for the potential realization of Si-based optoelectronic devices.

Table of contents

1 Introduction

From the invention of integrated circuits (ICs) in the 1960s to the most recent very large-scale integration (VLSI) technology, silicon has been the most important semiconductor material. The main advantages of silicon are the abundance, the high purity, the mechanical properties, the good heat conductance and, above all, the formation of a stable isolating oxide, which only makes possible the high degree of integration and packaging density in VLSI technology. These advantages have outweighed to date the mediocrity of the material in terms of bulk electronic properties, such as low carrier mobility limiting the speed at which a Si device can be operated, and the inherent lack of an effective light emitter due to the indirect band gap of this group IV material.

Conventional VLSI devices will probably soon reach a performance limit despite the still continuing reduction of the feature sizes to a state of the art $0.18\,\mu m$ and below. The vast number of metallic or semiconductor interconnects linking the active devices in an IC constitute a substantial part of the power drain, and thus heat generation, of the IC. A judicious choice of optical rather than electrical interconnects could potentially master this problem. [1] Hence, a reasonably efficient Si-based light emitting device that could be implemented into the chip compatibly with the established standard VLSI technology is needed.

There are several basic approaches to achieve an increase of the radiative transition probability in the otherwise indirect band-gap material Si: (see e.g. [2] and refs. therein) impurity mediated luminescence, band structure engineering by alloying (SiGe, SiGeC), quantum confinement structures (wires, dots) and a hybrid-approach, growing direct band-gap material onto Si.

The band structure engineering using heterostructures of SiGe alloys has already lead to new high performance electronic devices such as hetero-bipolar transistors [3] and to a number of passive optoelectronic devices like photodetectors and waveguide structures. [4] More important, these structures have proven to be compatible with integrated circuit technology. [5] The addition of small amounts of carbon to the SiGe alloy offers further flexibility in adjusting the energy gap and the strain involved in the heterostructures. [6]

Quantum dots have gained a lot of attention in the recent years due to the discovery, that structures containing Si particles of a few nanometers in diameter can emit intense luminescence. [7, 8] These structures, however, consist of Si particles surrounded by a silicon oxide or nitride matrix, leading to serious problems in contacting the particles and in achieving an optical confinement.

For the above reasons it is appealing to use the SiGe or SiGeC alloy system for the production of low dimensional quantum structures in Si. For this task the naturally occurring phenomenon of self-organization can be exploited and influenced by proper choice of growth conditions. Due to the lattice mismatch involved in the SiGe system, which is about 4% between Si and Ge, heteroepitaxy of Ge on Si leads to the formation of three-dimensional Ge islands, which relieve the compressive strain of the Ge layer. The size of such self-organized quantum dots is a critical issue. In the indirect band-gap group-IV semiconductor system smaller size of confinement structures strongly favors radiative transitions. [9] At usual epitaxial substrate temperatures the dot sizes are in the range of 50 nm and, hence, too large to exhibit zero-dimensional properties. At low growth temperatures, where the smallest dots assemble, [10] the crystallographic quality suffers and no significant luminescence is observed. So another approach for reduction of the Ge dot size is needed. Recently, it has been shown, that Ge islands as small as 10 nm can be fabricated on Si(001) surfaces precovered with a submonolayer of carbon, [11] that exhibit rather intense photoluminescence.

This work aims at the detailed investigation of the Ge island formation on C-precovered Si(001) surfaces grown by molecular beam epitaxy (MBE). A profound knowledge of the island formation process is necessary to be able to control the properties of the self-organized nanostructures by adjustment of external parameters. The morphological properties of the C-restructured substrate surface and of the subsequently formed Ge islands have to be revealed down to the atomic scale. To obtain morphological real space images with atomic resolution, the method of choice is ultra-high vacuum scanning tunneling microscopy (UHV-STM). For this purpose, a unique 4-inch-wafer UHV-STM for in situ studies has been designed and built in the course of this work, that has been combined with a commercial MBE system processing 4-inch substrates, [12, 13] and that routinely allows to study the epitaxially grown Ge / C / Si nanostructures thereon down to atomic resolution.

The challenge of how to combine a large sample UHV-STM with an epitaxy system is addressed first. This includes the brief description of the epitaxy system as one of the key constraints imposed on the STM design. The considerations regarding the special difficulties related to the large sample size are explained and the design of the UHV-STM, including the vacuum system, the scan head, the sample stage and the control electronics is presented in detail. Special emphasis is put on the suppression of wafer Eigenmodes, which is a critical factor for the given substrate dimension. The issues of the new instrument's calibration, the tip preparation and the resolution are also covered.

When studying the self-organized island formation in a rather complex multi-component system like Ge / C / Si, the structure after each stage of the deposition sequence must be known. Several questions arise in the course of these investigations: How does the deposition of a submonolayer of carbon alter the Si(001)(2×1) surface? What exactly causes germanium to form smaller islands after C-predeposition than on bare Si, as reported in Ref. [11]? What do these C-induced Ge islands look like on the atomic scale? Do the morphology and the

optical properties correlate? Which are the crucial parameters to further improve these properties?

To elucidate these questions, first of all the structure of the initial stages of C-incorporation into Si(001) is investigated in detail. The basic finding is the occurrence of domains with c(4×4) reconstruction after submonolayer deposition of C. This reconstruction on Si(001) has been under debate for a long time. [14-18] A careful analysis of STM images at different C coverages demonstrates, that the c(4×4) reconstruction is caused by C incorporation into the Si(001) surface. The comparison of STM images with density functional theory and total energy calculations, assuming different structural models, reveals the atomic structure of this carbon-related c(4×4) reconstructed domains. These C-rich domains turn out to be essential for the later Ge island formation.

The question, how these domains influence the subsequent growth of Ge dot structures on the C-precovered surface is examined next for Ge coverages between 2.5 and 6 ML and compared to the case of Ge on bare Si(001). The morphological properties obtained with STM and cross-sectional transmission electron microscopy (TEM) are compared to the optical properties from photoluminescence (PL) measurements. Conclusions about the origin of the PL and the recombination mechanisms are drawn.

Finally, the initial stages of the Ge-dot nucleation in the coverage range up to 1 ML are studied with STM. Here, the influence of the C-predeposition becomes obvious in that the Ge growth proceeds in pure 3D growth, excluding the formation of a Ge wetting layer. The results from this chapter support many findings from the previous chapter. They also show up the possibility to produce ultra-small Ge dots on Si(001), which are potential candidates for future Si-based luminescent devices.

2 Experimental

Scanning tunneling microscopy (STM) has become a powerful tool in surface science characterizing electrically conducting surfaces from the micrometer down to atomic scale. STM can be applied in various environments, including liquids, e.g. for biological or electrochemical investigations, air and vacuum (for an overview see e.g. Ref. [19]). In order to exploit one of the most outstanding possibilities of the STM technique, the achievement of 'true' atomic resolution in real space, the application of a well-defined and clean environment is generally necessary. For the investigation of epitaxial growth processes from the vapor phase, an ultra-high vacuum (UHV) environment is generally used, as it fulfills the need for atomically clean pure surfaces. Hence, UHV-STM is an ideal tool for the study of metal [20] and semiconductor [21] surfaces. Information about the electronic [22] as well as the morphological surface properties can be obtained.

However, most of the STMs are restricted to sample sizes of ~1 cm^2, limiting their application mainly to custom made sample-preparation and growth systems entirely designed for research applications. In spite of this, in device orientated silicon technology the minimum standard sample size is that of a 4-inch wafer serving as base material for all kinds of processing steps. A combination of STM with molecular beam epitaxy- (MBE) or chemical vapor deposition- (CVD) machines that process such large samples is complicated, since the pumps of the growth chambers are inherent sources of vibrations. Moreover, due to their large diameter and small thickness, for samples like 4-inch semiconductor wafers mechanical Eigenmodes can unintentionally be excited, which makes high-resolution STM measurements difficult or even impossible. Furthermore, the direct implementation of an STM into the growth chamber would require that MBE or CVD operation had to be stopped during STM-investigations [23], which is not acceptable in terms of the epitaxy system production capacity.

In this chapter, we demonstrate that the problems mentioned above can be mastered. We have realized a reliable UHV-STM for in-situ investigations on complete 4-inch wafers. It has been particularly designed for the combination with a preexisting MBE/UHV-CVD system that exclusively processes 4-inch wafers. Despite this sample size atomic resolution is routinely obtained on the silicon / germanium based samples investigated in this work.

This chapter will give insight into the equipment for thin film production, as well as a detailed description of the whole STM design, which includes the separate STM vacuum chamber, the STM scan head and sample holder, the sample transfer from the epitaxy system to the STM and the setup of the STM control electronics.

2.1 Epitaxy system

Fig. 2-1 represents a schematic top view of the whole UHV system for sample fabrication. The UHV system consists of a MBE-chamber (1) combined with a UHV-CVD-reactor (2), both designed for use of 4-inch samples. In addition, a UHV chamber equipped with a DC-plasma source (Balzers UPQ 160) (3) is applied for wafer cleaning with a hydrogen plasma as well as for Si growth by plasma-enhanced CVD.

The UHV chambers are connected to each other by sample transfer chambers (4, 5) individually pumped and separated by UHV gate valves. The central sample transfer chamber (manufactured by Balzers) (5) is located between MBE- and plasma chamber. It contains a sample handling mechanism basically consisting of a movable fork with a depression near its edge. A wafer support ring holding the wafer lies loosely on the fork only centered by the
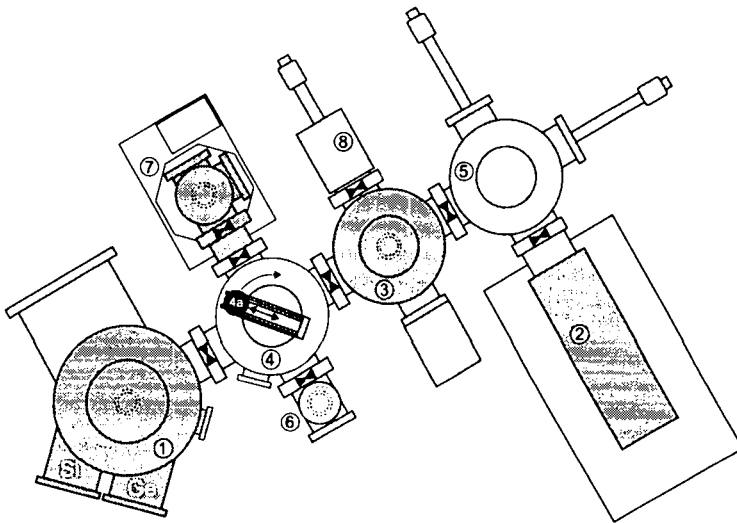
(1)	MBE chamber	(5)	CVD transfer chamber
(2)	UHV-CVD reactor	(6)	multiple-wafer load lock
(3)	plasma chamber	(7)	UHV-STM chamber
(4)	central transfer chamber	(8)	load lock for CVD
(4a)	Si wafer in Si support ring		

Fig. 2-1: Scheme of the growth system for SiGe-based films, consisting of the MBE-chamber, the sample handler and the UHV-CVD reactor. The transportable STM-chamber is attached to the sample handler for in-situ sample transfer and detached for imaging.

depression. The fork can be rotated freely in the horizontal plane and can be extended telescope-like up to 84 cm to bring the samples to the sample holder positions in the adjacent chambers. In addition, the handler fork can be moved between two fixed vertical positions to load/unload the sample onto/from these sample holders.

Attached to this transfer chamber is a smaller multiple-wafer load lock chamber (6), which has been designed and built within this work. In this wafer tray up to six wafers can be loaded and stored under UHV conditions. The tray is vertically movable, so that each wafer can be accessed individually by the sample handler.

Onto the forth flange of the transfer chamber the UHV-STM chamber (7) can be bolted, which will be described in detail in a later section of this chapter.

Another larger load lock (8) is connected to the plasma chamber. This allows loading of individual wafers for plasma processing and loading of quartz wagons carrying up to 20 wafers for the CVD without affecting the operation of the other parts of the system. Quartz wagons are guided on rails and turntables and are pushed/pulled by means of magnetic linear feedthroughs.

As molecular beam epitaxy is the growth method used for all depositions made for this

(1) electron beam evaporators (Balzers EBS 200 U) for Si and Ge

(2) carbon sublimation source (SUKO, MBE - Komponenten GmbH)

(3) high temperature effusion cell for boron doping and low temperature cell for antimony (HTS35 and NTEZ, respectively, MBE - Komponenten GmbH)

(4) 4-inch Si substrate

(5) cryopanel, liquid nitrogen (LN₂) cooled

(6) water cooling jacket / heater jacket

(7) 4 in. HOPG substrate heater

(8) quadrupole mass spectrometer for Si and Ge beam flux monitoring and flux regulation

Fig. 2-2: Cross-section of the molecular beam epitaxy chamber. Equipment like shutters, pumps and pressure gauges is not shown.

thesis, the MBE chamber is described in more detail. It is a commercially available MBE system (Balzers UMS 500) which is optimized for the growth of silicon based material on substrates with a diameter of four inch. The chamber reaches a base pressure of less than $1 \cdot 10^{-10}$ mbar pumped by a 330 l/s turbomolecular pump and a titanium sublimation pump. Pressure is measured by a Bayard-Alpert ionization gauge. A schematic cross-section of the MBE chamber is given in Fig. 2-2.

There are five evaporation sources installed: two electron beam evaporators (Balzers EBS 200 U) for Si and Ge (1), a carbon sublimation source (SUKO 63, MBE - Komponenten GmbH) (2), a high temperature effusion cell for boron doping (HTS 35, MBE - Komponenten GmbH) (3) and a low temperature effusion cell for antimony (NTEZ, MBE–Komponenten GmbH) (3). The sources are installed at the bottom of the chamber and the substrate (4) is located vertically above the sources in the focus on the symmetry axis. The distance between the sources and the substrate is 50 cm. This offers the advantage of a good homogeneity of the source fluxes across the wafer. However, the large distance also necessitates high evaporation rates of the source materials to get the desired growth rates, and thus leads to a high energy and source material consumption, which in turn increases the overall heat load inside the vacuum chamber. Typical operation parameters of the e-beam sources are an electron beam current of about 150 mA at 10 kV (1.5 kW) and filament current of 100A at 14V (1.4 kW) for the carbon sublimation source.

In order to cope with the heat radiation, the MBE chamber has two cooling circuits. First, a liquid nitrogen-cooled (LN$_2$) cryopanel (5) in the lower part of the chamber shields the upper chamber parts from a large portion of the radiated heat as well as from unwanted material deposit. The panel has suitable holes that allow the molecular beam flux from the sources to reach the substrate. Secondly, the whole growth chamber is covered with a water-cooling jacket (6), keeping the chamber walls cool during operation. In addition all sources (except Sb) possess their own water cooling. These measures allow to keep the pressure below $2 \cdot 10^{-8}$ mbar during operation of all sources. The cooling jacket is additionally equipped with electrical heaters for chamber bakeout.

The 4-inch substrate is held at a distance of about 5 mm below a pyrolithic graphite (HOPG) heater (7) of the same diameter. The heat is entirely transferred by radiation, giving a homogeneous temperature distribution across the wafer. Substrate temperature is measured with a thermocouple behind the heater, which gives a value that is reproducibly related to the temperature at the substrate surface. However, one has to state, that the thermocouple temperature value surely deviates from the effective substrate surface temperature by an unknown but reproducible value, i.e. the thermocouple reading is higher than the real surface temperature. All temperatures in this work refer to the thermocouple value only. In the literature a deviation of more than 50°C has been reported for a very similar setup of a 4-inch wafer heater, [24] determined by a complicated procedure involving thermocouples bonded to the wafer surface. Such a calibration could not be performed in our MBE system. But the

actual deviation is presumably similar in our case. Temperature differences ΔT can of course be more accurate than absolute values. The heater temperature control and regulation is accomplished by a PID feedback loop controller (Eurotherm 930 series) via the thermocouple and an adjustable DC-power supply. Temperatures up to 1000°C can be achieved. A sample rotation mechanism allows the sample to be rotated under the heater driven by an electric motor, which assures film homogeneity across the whole 10 cm wafer better than 10% for all source materials.

The MBE machine is computer controlled (DEC VAX workstation), including vacuum and process control for deposition. The beam fluxes of the Si and Ge e-beam evaporators are permanently monitored by a quadrupole mass spectrometer (Balzers QMA 400) (8). The actual flux is evaluated by a feedback loop in order to regulate the flux exactly to the set point value by changing the electron emission current and the beam focus in the crucibles. In this way, a very good flux stability and fast flux transients are guaranteed. The two high temperature effusion cells with direct current heated HOPG filaments (B and C) are either temperature controlled (Eurotherm 930 series controller), or are used with a constant current that is reproducibly related to the flux. The low temperature cell for Sb is always operated with a temperature control loop.

An electron gun (Focus GmbH) allows for in situ reflection high-energy electron diffraction (RHEED) experiments in the MBE chamber. It is equipped with two electrostatic octupoles to control the angle of incidence and the beam position on the wafer independently without substrate tilt. The azimuth is set by manually rotating the substrate into the proper direction. The diffraction pattern is projected onto a fluorescent screen and detected by a video camera connected to a personal computer.

2.2 The UHV- STM

Design considerations

In the framework of this thesis, we have realized an ultra-high vacuum scanning tunneling microscope |12| that is compatible with the epitaxy system described in the previous section. The following requirements were considered during the design:

1. The STM must be adopted to the sample geometry of the epitaxy system, i.e., it must handle 4-inch Si wafers in a Si support ring without modifications.
1. In situ sample transfer from the epitaxy system to the STM making use of the existing sample handler.
1. Effective damping of vibrations, *atomic resolution* mandatory in spite of large sample size.
1. Accessible surface area as large as possible.

1. In situ exchange of STM tip.

None of these requirements can be treated independently, as a certain solution for one of them always imposes certain restrictions on or favors others.

Two basic set-ups are imaginable: a) STM chamber permanently connected to the epitaxy system or b) STM chamber detached for measurements. Both are consistent with points 1, 2, 4 and 5, but we assumed serious problems of coping with requirement 3 in case of a permanently connected STM. The epitaxy system is entirely equipped with mechanical pumps. Each chamber has its own turbomolecular pump, which is rigidly coupled. Due to their high rpm (30000 to 80000 rpm) they produce vibrations in the range of several hundred Hertz, which is just the frequency range most severely affecting STM imaging. While one could still think of partly decoupling the STM chamber from transmission of these vibrations (e.g. by insertion of two concentric welded bellows between two flanges, where the gap is air-pressurized to compensate for the vacuum force), what remains, is the acoustic noise in the epitaxy laboratory. All foreline pumps including large rotary vane pumps and roots blowers for high gas loads of the CVD and plasma chamber are situated inside the lab, producing a considerable acoustic noise level. Additionally, it can be assumed that a 4-inch sample is always more prone to vibration problems than a usual small sample and, hence, the option of a permanently attached STM chamber was omitted. Instead, we went for a compact detachable chamber on a trolley, which is taken to another room for measurement.

As a compromise that fulfills all the requirements mentioned above, we have realized the STM as described in the following section.

Basic description:

The STM is contained in a transportable ultra high vacuum chamber with a volume of about 25 dm^3, that is attached via a lock chamber to the sample transfer chamber of the epitaxy system. The prepared wafer is transferred from the growth- to the STM-chamber by means of the transfer system of the MBE/CVD-system, avoiding additional sample handling by space consuming transfer rods or wobble sticks. To master the noise problems due to mechanical vibrations caused by the components of the growth system, the STM-chamber is detached from the system and moved to another room for high resolution measurements. Here vibration isolation for the low frequency range is done by laminar flow isolators (Newport I 2000 series) carrying the whole chamber. Inside the vacuum vessel a spring/eddy-current assembly, that suspends both the sample and the STM, provides additional effective vibration damping. Wafer Eigenmodes are suppressed by a special design of the sample stage. The STM itself is based on the Beetle originally proposed and realized by Besocke. [25] Since a ramp, that the original Besocke design used for the tip approach, is not practicable in our case, we implemented an Inchworm motor for the tip approach.

An important feature of our design is the ability to probe a large area of the wafer, allowing to examine the surface within a diameter of more than 60 mm. This is especially important for the characterization of the homogeneity across the wafer.

STM vacuum system

The vacuum system (see Fig. 2-3) consists of two parts, the main chamber (1) with the STM and the lock chamber (2) for the connection to the MBE/CVD system, separated by a DN 150 CF UHV gate valve (3) (VAT). The main chamber is a standard DN150CF five way cross with seven additional DN40CF flanges on the sixth side. The STM with damped sample
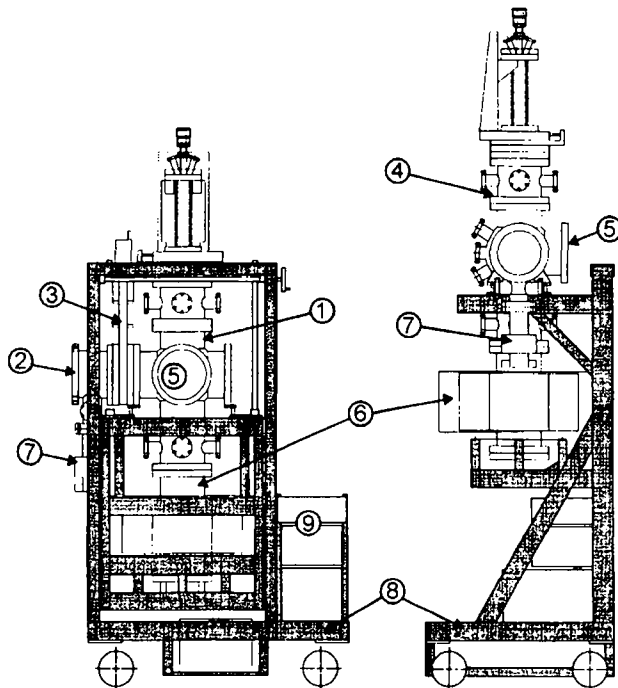
(1)	STM main chamber	(6)	ion getter pump (200 l/s)
(2)	lock chamber	(7)	turbomolecular pump (50 l/s)
(3)	DN150CF gate valve	(8)	movable trolley with chamber height
(4)	flange carrying whole STM		adjustment
	assembly	(9)	power supplies for pumps and
(5)	viewports DN150CF		pressure gauges

Fig. 2-3:   Drawing of the transportable UHV chamber containing the STM

holder is mounted on a DN150CF flange (4) fixed at the top flange of the chamber. Two of the side flanges contain viewports (5) in order to inspect the STM during sample handling and STM positioning. The lower flange carries an ion pump (MECA2000 PIDG200, 200 l/s) (6)with a titanium sublimation pump incorporated. Rough pumping is done via the lock chamber that is equipped with a turbomolecular drag pump (Pfeiffer TMU065, 60 l/s) (7). The volume of the lock chamber is kept as small as possible to achieve reasonably fast pump down times, although DN150CF flanges are obligatory for 4-inch sample transfer. The base pressure corresponds to $1 \cdot 10^{-10}$ mbar in the STM chamber and $1 \cdot 10^{-9}$ mbar in the load lock after bakeout.

The vacuum system is mounted on a compact trolley (length 90 cm, width 65 cm) (8) which also comprises the power supplies (9) for pumps and pressure measurement. Thus the whole system can be moved from one lab to another only connected to the power line by a single cable. The height of the chamber center axis with respect to the floor can be adjusted between 95 cm and 145 cm. This is necessary to adapt to the transfer flange height of the MBE system and to be able to pass through doors. The chamber can be lowered down onto a custom made stone plate that is floating on the laminar flow isolators. The isolators suppress the coupling of building vibrations above a frequency of 1 Hz.

STM set-up

For the design of the STM scan head and the sample holder the two fundamental constraints were to suppress wafer Eigenmodes (see section 2.3) and to make possible a large accessible area. At first glance, there are two possible basic configurations for a large sample STM: the wafer could be placed face down on top of the microscope or, vice versa, the microscope could be placed onto the wafer. The first setup has already been reported for a 3-inch sample STM [23], where the wafer is put on top of the three STM piezos arranged in an inverse Beetle-type geometry. However, with a setup of this type one can access only a small area in the center of the wafer surface, since the center of gravity of the wafer has to remain within the area spanned by the three piezos. Furthermore in such a setup, the wafer vibrations cannot be effectively suppressed.

The more promising configuration is thus to place the STM scan head onto the wafer from above. In this way, the wafer can be supported on its entire backside to avoid the excitation of its Eigenmodes, and the STM can be placed virtually anywhere on the surface, assuring the large accessible area. One minor disadvantage is, that additional measures have to be taken to turn the wafer, which is processed face down in the epitaxy system, around by 180° to allow the access of the epitaxial surface from above. This can, however, be easily solved by the proper design of the sample stage, that is described later. But before this, the design of the STM scan head is illustrated in the following.

The cross-sectional drawing and the 3D-view in Fig. 2-4 show the simple construction of the STM-head. Three identical piezo tubes (2) with four quadrant electrodes on the outer

a)   b)

1cm
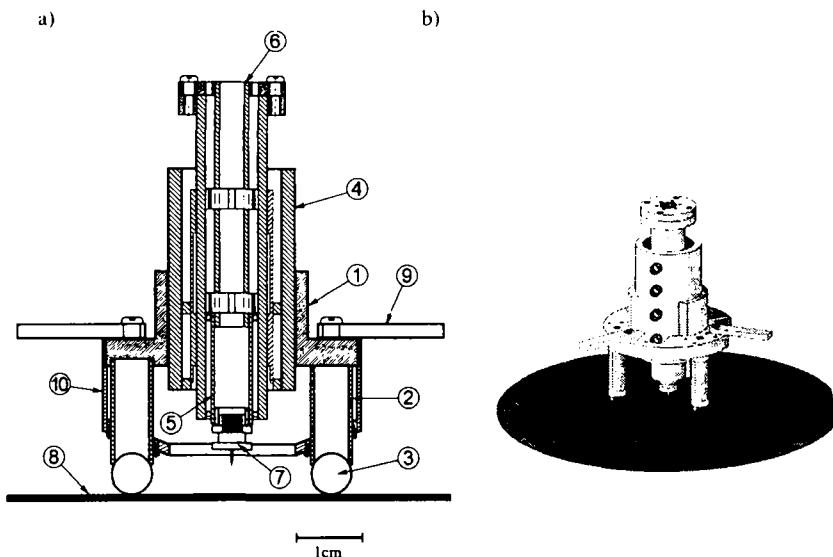
Fig. 2-4: a) Cross-section of the STM-head: (1) STM body, (2) piezo tube, (3) ruby ball, (4) Inchworm, (5) scan piezo, (6) ceramic tube with centering rings and Al flange plate, (7) magnetically fixed tip holder, (8) Si wafer (9) levers for lifting the microscope, (10) cover supporting and damping the lower part of piezo legs with small viton pieces. b) 3-dimensional view of the STM on the Si sample (without the cover)

circumference are glued to the STM body (1) with conductive UHV epoxy resin, each of them carrying a ruby ball (3) at its end. With these ruby balls the STM is lowered down directly onto the wafer surface (8) at the desired position. This coarse positioning is done by a standard UHV xyz-manipulator with a range of ±25 mm in the xy-plane and 100 mm in the z-direction (PM25-100, VAb Vakuum-Anlagenbau GmbH). In addition, the STM can travel on the surface for several millimeters in each direction and rotate by means of inertial motion, if a sawtooth-like voltage is applied to the electrodes of the three outer piezos (slip-stick-motion). A DC-offset voltage of ±200V at these piezos allows an exact positioning of the tip within ~2.5 µm. In this way, an area of about 60 mm in diameter in the center of the wafer can be accessed by the STM tip, which corresponds to ~ 30 cm^2.

Although the ruby balls leave 20 to 50 µm wide scratches on the wafer surface while moving the STM by means of inertial motion, we consider this surface damage to be non-significant for our studies. Usually the STM only walks very small distances because larger displacements are accomplished by retracting and posing the STM with the manipulator. Even if we assumed a rare case, where the STM is positioned 10 times randomly on the surface and each time travels 5 mm, the ratio of the damaged surface to the accessible area is below 5‰. So in practice, the probability to investigate involuntarily a damaged area is negligible.

In the center of the microscope a UHV-inchworm motor (4) (Burleigh UHVL Inchworm Motor) is mounted for tip approach. It is entirely fabricated of ceramics. The inchworm shaft has a travel length of 10 mm with a step resolution of 1 nm. Inside this hollow shaft the fourth piezo tube (5) responsible for the scanning motion and tip-sample distance control is inserted. It is glued to a ceramic tube (6) which is centered inside the inchworm shaft by means of two centering rings, thus avoiding bending modes of the rather long inner tube. Inside it is covered with a metal mesh serving as shielding for the tunneling current. The upper end of this ceramic tube is glued to a flange-like aluminum plate that is screwed against an aluminum ring attached to the upper end of the inchworm shaft. This assembly offers two advantages: First, in contrast to a scan piezo directly glued to an inchworm shaft, one can relatively easily separate the scan piezo from the inchworm for service without the danger of destroying the inchworm. Second, as both the inchworm and the tube, which holds the scan piezo, are made from ceramics, the compensation of thermal drift in the tip-sample distance, that is achieved with a normal beetle design, is still valid to a first order approximation. The electrical connections to the STM are made of 50 µm capton (polyimide) isolated copper wires.

At a later time, a cover (10) has been added around the lower part of the STM head, which has three holes for the piezo legs. The piezos are additionally damped inside the holes by small viton pieces squeezed into the gaps between piezos and cover. This put an end to irregularly observed erratic oscillations during scanning, which we attributed to a possible rotational Eigenmode of the STM head.

We use a 250 µm diameter polycrystalline tungsten wire for the tunneling tips. They are electrochemically etched in NaOH solution (see next chapter). The tip holder (7) comprises a small CoSm magnet that holds it in place at the end of the scan piezo. Thus the tip holder is exchangeable without breaking the ultra high vacuum. New tips are introduced via the lock chamber with a transfer rod holding a tip magazine for three tips. The exchange is accomplished by moving the microscope with the xyz-manipulator so that the tip holder is pushed into a fork of the tip magazine. Then the microscope is retracted and the tip holder is removed from the scan-piezo.

STM sample stage

The STM-sample stage can directly receive a wafer from the sample handler of the MBE/CVD system. It includes the spring suspension and eddy current damping. A photograph is represented in Fig. 2-5.

In the MBE-system the wafer is moved and processed upside down, that means, the surface of interest is on the bottom side. The wafer resides in a support ring equally made of silicon in order to avoid contact with stainless steel parts, that would result in contamination with metal impurities. This support ring, 115 mm in diameter, can be transferred to the STM by the sample handler described above. The fork only moves horizontally and can take two defined vertical positions. A scheme of the loading sequence is shown in Fig. 2-6. In the upper position the support ring is pushed into the drawer-like STM sample holder (1), then the transfer fork (5) is lowered down. The wafer (6) is still upside down. After the sample handler fork is withdrawn, the STM sample holder is turned by 180° around its axis (7) by means of a rotary UHV feedthrough on the center DN40CF flange of the chamber. This allows the access of the surface for the STM from above (Fig. 2-5.). During this turn, two spring-loaded levers (2) push against the wafer and clamp it at two points near the edge to the bottom plate of the sample holder. This plate is machined to be accurately plain so that the wafer backside closely touches it. In this way wafer vibrations are effectively suppressed, as will be shown later. Like all parts of the sample stage getting into contact with the silicon sample support ring or the wafer, the bottom plate and the clamping levers are manufactured from pure tantalum in order to prevent wafer contamination.
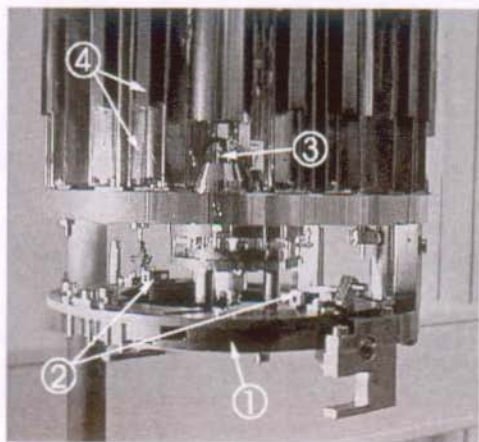

Fig. 2-5: Sample stage in measuring position. The STM is posed on the wafer. The drawer-like Ta sample holder (1) can be turned by 180° for sample introduction. The wafer is clamped at two points by the Ta levers (2). The whole stage is suspended with springs (3) and damped by eddy currents. The copper pieces and magnets (4) are visible on top of the sample stage.

a)

(1)   drawer-like sample holder (Ta)

(2)   clamping lever, spring-loaded
       (Ta)

(3)   springs for sample stage
       suspension

(4)   eddy current damper (CoSm
       magnet and Cu piece)

(5)   transfer fork

(6)   Si wafer in substrate ring

(7)   rotation axis
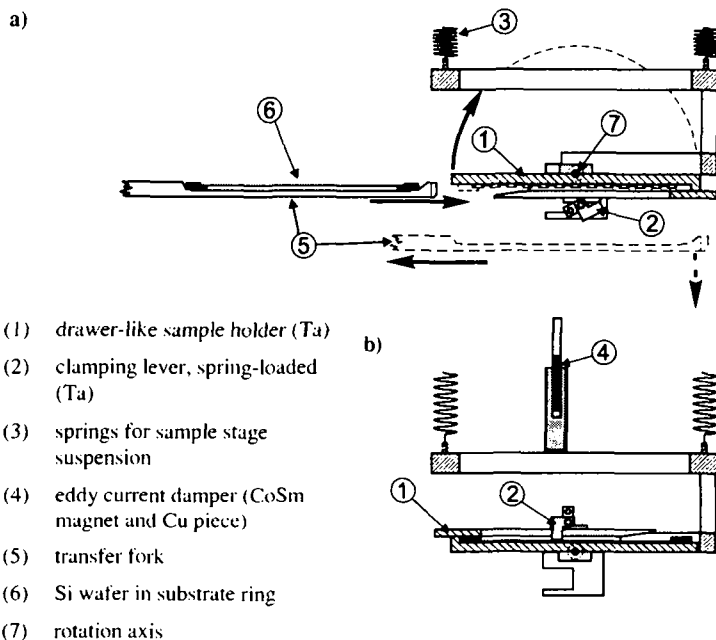
Fig. 2-6:   Cross-section of the STM sample stage and illustration of a sample loading sequence

During the transfer the sample stage is rigidly fixed in the transfer position. For STM measurement, before the STM is lowered onto the sample surface, the support is removed and the sample stage is suspended by four soft spiral springs (3). These springs have a nominal extension of 250 mm under load, thus leading to an Eigenfrequency of 1 Hz for the stage. On top of the stage 16 U-shaped copper pieces are fixed at the circumference for eddy current damping. Each of them embraces a fixed 1 Tesla CoSm permanent magnet (4). This assembly leads to a Q-factor of 12 in vertical direction and a Q of 4 for horizontal movements and torsion of the stage. Thus the suspension provides an effective isolation against mechanical and acoustical noise from the outside.

STM electronics

The control electronics is a vital part of any scanning probe microscope, since it is responsible for all parameters of imaging and STM hardware control, such as sample bias, tunneling current, tip-sample distance feedback, scan motion and tip approach, to mention the most important ones. It can be divided into two parts: STM control and data acquisition. Whereas the latter is always done by means of a computer equipped with analog/digital converters, that record the measurement signals (e.g. z-piezo position), the STM control can

either be carried out by the computer as well, or it can be performed by a separate analog control unit. A mixture of both solutions is also possible.

In our first set-up (Fig. 2-7a), we used a home-built stand-alone control unit, which had been especially designed for Beetle-type STM heads ("Besocke electronics"). It is a very basic set-up, where a computer is solely needed for data acquisition. The electronics provides the voltages for all piezos of the microscope (three legs and the inner scan piezo), including the waveforms (voltage ramps) for the inertial motion of the microscope body. This is normally used for tip approach (rotation) and microscope positioning (lateral motion) in a beetle set-up. Since in our case the tip approach is done by an inchworm motor, an additional Inchworm control unit (Burleigh ARIS 950ULN) is used. The approach is started manually on the Inchworm controller handset. A TTL stop signal is sent from the STM control unit to the Inchworm controller, once the onset of a tunneling current is detected, to stop the approach. As the approach speed is also set manually, this procedure is not very reliable and it is slow. Although the feedback loop retracts the tip immediately after current detection, a contact between tip and sample sometimes cannot be avoided.

The voltage range of the piezo voltage amplifiers is restricted to ± 40V, limiting the scan range with this electronics to 280 nm.

We use the PRODAS ([26]) image acquisition software running under MS-DOS in conjunction with the provided data acquisition board (TXA12), which goes into a PC IDE slot. A disadvantage of this board is the use of only 8-bit a/d converters. This limits the vertical resolution on samples with higher maximum corrugations, e.g. 3D islands, or a net slope such, that atomic corrugations cannot be resolved. Imaging of such samples with atomic resolution is then only possible using the derivative mode, where the signal is high-pass filtered before being sent to the computer. This suppresses the low-frequency parts of the surface topography and makes average positive slopes appear bright and negative slopes dark, while leaving atomic corrugations (with high spatial frequency) nearly unaffected. Images acquired in the derivative mode appear as illuminated from the left. Obviously a quantitative analysis of height differences is restricted or even impossible.

The Besocke electronics was meant to be a first solution, which was sufficient for preliminary experiments for STM calibration and performance evaluation. We planned from the beginning to get a more sophisticated electronics. By the exchange of the Besocke electronics with a RHK Technology SPM100 PC-based electronics the restrictions mentioned above are mastered. In particular the scan range is increased by more than a factor of five.

The RHK unit can also be used as an analog stand-alone controller, but it offers the possibility of computer control by the RHK SPM32 software package running under DOS. Most imaging parameters can be set in the software and all parameters are read out by the computer. Only the feedback loop operates analog. The interface between electronics and computer is a 16 channel 12 bit analog/digital digital/analog conversion card (Data Translation DT2812) in the PC. The software is also capable of computer controlled tip approach with the

a)

b)
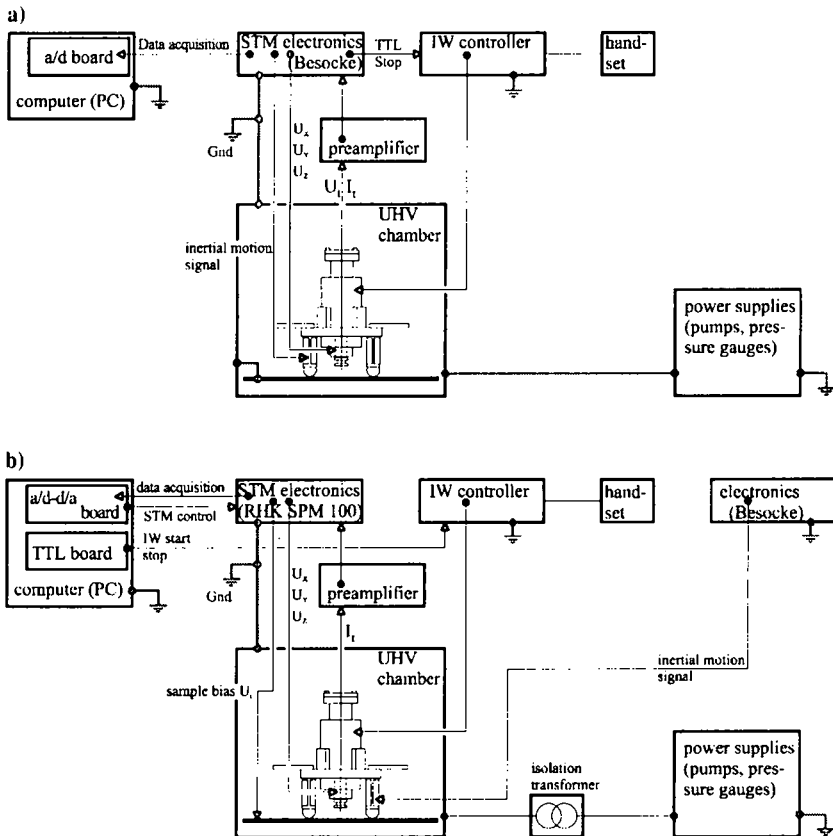
Fig. 2-7: Block diagram of the STM and its periphery; a) initial configuration with Besocke electronics, b) configuration after installation of the RHK control unit.

Inchworm motor, as the Inchworm controller is interfaced via a digital I/O TTL interface card (Data Translation DT2817). This makes the tip approach faster and reliable, avoiding effectively any tip-sample contact during approach. A block diagram of the set-up is shown in Fig. 2-7b.

We kept the Besocke electronics connected to the three piezo legs of the STM, so that it can still accomplish the inertial motion of the microscope on the sample. Only the center scan piezo is connected to the RHK unit. With the high voltage amplifier outputs of up to ±130 V this configuration gives a maximum scan range of 1.6 µm and a z-range of up to 300 nm.

While the Besocke electronics applies the tunneling bias voltage to the STM tip with the sample grounded, the RHK unit needs to apply the bias to the sample. This has been

considered right from the beginning of the sample stage design, the latter being electrically isolated from the chamber ground when suspended in the measuring configuration. Despite this, the shielding and grounding scheme had to be slightly reworked for the RHK unit due to electrically induced noise problems related to the different biasing (ground loop), which was solved by introduction of an isolation transformer into the leads to the vacuum power supplies on the trolley.

2.3 Wafer Eigenmodes

An important source of vibrations in scanning tunneling microscopy is the STM itself. The scan motion, a slow ramp usually generated stepwise by a digital-analog converter, and the z-piezo movement due to the distance regulation by the feedback circuit contain a wide spectrum of frequencies. In consequence, an amplification of any of these frequencies within the sample holder and STM has to be avoided. The most effective way is to build the STM and sample unit as compact and rigid as possible with high Eigenfrequencies of all components. However, in our case the compactness is limited by the sample size. While the STM-head and the sample holder can be designed sufficiently rigid by choice of material thickness, the geometry of the silicon wafer is given. Due to its typical thickness between 0.3 mm and 0.8 mm and its large diameter of 100 mm, it shows low frequency Eigenmodes. The theory |27| predicts the Eigenfrequencies of a circular plate of thickness s and radius r as:

$$v_{mn} = \frac{\pi s}{2r^2}\beta_{mn}^2\sqrt{\frac{E}{3\rho(1-\mu^2)}} \qquad (2.1)$$

with the elastic modulus E, density ρ and Poisson-number μ. The β_{mn} denote the coefficients for the non-harmonic Eigenmodes with m nodes in radial and n nodes in azimuthal direction. The boundary conditions are given by fixing of the wafer around the edge of the circumference. The first mode, v_{01}, with $\beta_{01}=1.015$ has one maximum in the center of the plate and the second, v_{11}, with $\beta_{11}=1.468$ has two maxima and one node across the middle of the wafer. For a 4-inch silicon wafer with a thickness of 0.5 mm eq.(2.1) yields frequencies of 630 Hz and 1315 Hz respectively.
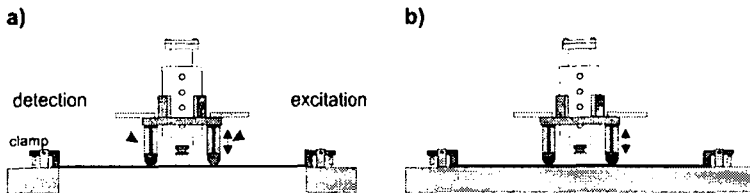

Fig. 2-8:   Experimental set-up for wafer-Eigenmode detection. One piezo is excited with a small amplitude and the response is detected at another piezo. a) Wafer is only supported at the edge; b) Wafer is clamped onto a flat plate supporting the entire backside.

In order to verify the appearance of the Eigenmodes, we positioned the STM in the center of a wafer that was supported only around its edge (Fig. 2-8a). One of the three outer piezos was excited with an ac voltage of 0.8 V_{pp} to vibrate along its symmetry axes, that means perpendicular to the wafer surface (amplitude about 2 nm). The response signal of the system wafer/STM was taken at a second outer piezo and detected with a lock-in amplifier. The obtained frequency spectrum is shown in Fig. 2-9 in the upper curve. Its most important feature is the resonance peak at 1280 Hz. We attribute this peak to the second Eigenmode v_{II} of the wafer, as the excited piezo is located slightly away from the wafer center and so the excitation of this mode is probable. A second peak is visible at 1920 Hz and a third one, although smaller, at 106 Hz. Their origin could not be determined definitely. We believe, that they occur due to the presence of the STM on the vibrating wafer, as both, STM and wafer, cannot be considered as independent.

Such resonances give rise to periodic perturbations in the images. [23] Therefore, we were looking for a simple way to suppress these modes. This is done by supporting the entire wafer by simply putting it onto a 6 mm thick, rigid tantalum plate and clamp it as mentioned above (Fig. 2-8 b). The vibration spectrum taken in this configuration is plotted in the lower curve in Fig. 2-9. The peak at 1280 Hz has completely disappeared, which demonstrates the efficient suppression of the Eigenmode. Even the peak at 106 Hz has vanished and the one at 1920 Hz has decreased in amplitude by a factor of three, indicating that they were at least partly due to the free wafer vibrations.
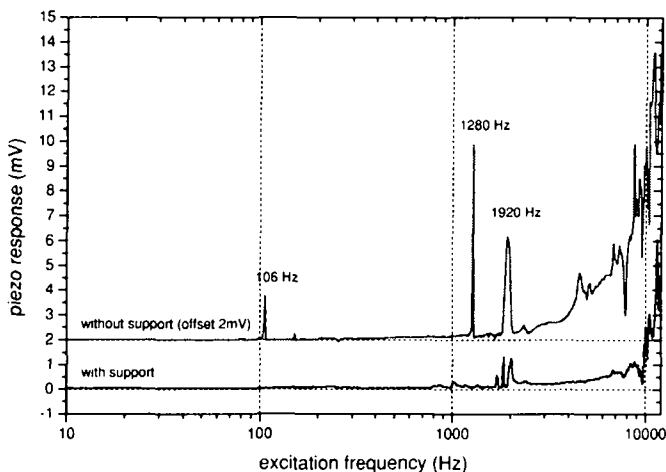

Fig. 2-9: Resonance spectra of the ensemble STM/wafer demonstrating the wafer Eigenmodes. For a wafer supported only at its circumference (upper curve) distinct resonance peaks appear, whereas for a wafer clamped onto the flat surface of the sample stage (lower curve) they disappear.

2.4 Conclusion

A UHV-STM for *in situ* studies of 4-inch wafers has been designed, built and brought into operation, that is compatible with the commercial Balzers MBE/UHV-CVD system. Contrary to other large sample STMs, where the sample is put on top of the STM, it can probe areas one or two orders of magnitude larger. For example, for the commercial large sample STM (LSSTM) of Omicron Vakuumphysik GmbH an accessible area of only 1 cm^2 is given, and the 3-inch wafer STM of Butz et al., [23] where the wafer is put on top of the three STM piezos, can access no more than 0.6 cm^2, as they are only 12 mm apart. We have achieved atomic resolution on Si(111) and Si(001) after a drastic reduction of the wafer Eigenmodes (as will be demonstrated in the following chapter). [12] This reduction can only be done by rigid support of the wafer with a plate, resulting in a heavy sample unit. This fact, and the demand for the large accessible area, necessitates to place the STM on top.

The combination of a powerful STM with an MBE/UHV-CVD system enables us to study different aspects of epitaxial growth on an atomic scale.

3 Setting up the STM

In order to be able to actually measure distances and heights on the atomic as well as on microscopic scale with a scanning tunneling microscope, it must be calibrated. The sensitivity of the piezoelectric actuators that move the tunneling tip have to be determined; i.e. the tunneling tip deflections in lateral as well as in vertical directions have to be related to the voltages applied to the piezo tubes. This can of course be theoretically calculated from the piezo tube geometry and its material parameters, but a calibration using well-known distances on a test sample yields more accurate values.

3.1 Properties of piezoelectric actuators

The physical effect exploited in piezoelectric actuators is the so-called inverse piezoelectric effect occurring in many polar crystals. This effect consists of a defined deformation of the crystal unit cell when an electric field is applied across it. If the whole crystal has a defined direction of polarization, this results in a macroscopic deformation of the crystal. The direction of deformation and its magnitude depend on both the direction of the electric field $\vec{E}$ with respect to the polarization axis $\vec{P}$, as well as on the set of piezoelectric constants $\overline{d}_{ij}$ [nm/V] of the piezoelectric material, which is in fact a symmetric tensor. Due to its high piezoelectric constant, a widely used material is PZT [lead zirconium titanate $Pb(Zr,Ti)O_3$], which can be modified by incorporation of oxides from other metals like Mg, Li, Nb etc. to adapt it to special applications.

One obtains a system of linear equations between the relative length change $\Delta\vec{L}$ and the electric field:

$$\Delta\vec{L} = \overline{d}_{ij} \cdot \vec{E} \qquad (3.1)$$

In STM applications the most commonly used case is, that the electric field $\vec{E}$ is parallel to the polarization axes $\vec{P}$. In this case, the tensor component d_{33} describes the expansion in the direction of the electric field, whereas d_{31} determines the length change perpendicular to it. For a tube scanner, which has electrodes on the inner and outer surfaces (Fig. 3-1) only the latter case is relevant. The material is radially polarized and a voltage applied between inner and outer electrodes causes expansion or contraction along the tube principal axis.

A tube scanner can be used for lateral displacements (scanning motion) and at the same time for height regulation. This is accomplished by the electrode geometry. The inner electrode

covers the entire surface, whereas the electrode for the lateral motion is sectioned into four equal quadrants. If equal voltages of opposite signs are applied to two facing outer electrodes with respect to the inside, the tube will bend into circular shape, because it expands on one side and contracts on the other. If identical voltages are applied to all four quadrants, the tube will just change its length.

The formula for the absolute longitudinal deflection Δz is derived from eq. (3.1) by replacing the electrical field with the voltage U between the two electrodes at a distance t (thickness of piezo tube wall) and introducing the electrode length l:

$$\Delta z = \mathbf{d}_{31} \frac{U}{t} \cdot l \tag{3.2}$$

The formula for the lateral deflection of a four quadrant piezo can be approximated by [28]:

$$\Delta xy = 0.9 \frac{\mathbf{d}_{31} l}{t(d_o - d_i)/2} \cdot U \tag{3.3}$$

where l is the electrode length and d_o and d_i are the outer and inner tube diameters, respectively, if the voltage U is applied with opposite sign to two opposite electrodes.

In order to minimize the cross-talk between xy- and z-motion, we have decided to set up the electrodes as shown in Fig. 3-1. The four quadrant electrodes on the upper half are sepa-


piezoelectric
constant:

$\mathbf{d}_{31}$ = 0.127 nm/V

scan piezo
dimensions:

d_o = 6.25 mm
d_i = 5.28 mm
t = 0.485 mm
l = 5.0 mm
l_2 = 13.0 mm
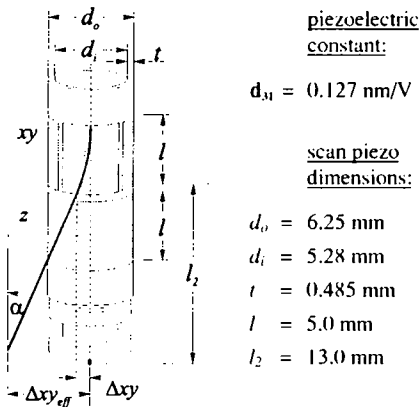
Fig. 3-1: geometry of the scan piezo electrodes and resulting tip deflection.

rated from the z-electrode on the lower half, both having a length of 5 mm. The inner electrode is electrically grounded. The piezoelectric material used is PZT-4 (EBL#1 from Staveley Sensors Inc.), which has a $\mathbf{d}_{31}$ of −0.127 nm/V.

According to equation (3.2) the theoretical z-deflection is Δz = 1.309 nm/V.

For determination of the effective lateral movement of the tip one needs to take into account the location of the tip with respect to the piezo electrodes (Fig. 3-1.). Equation (3.3) gives the piezo deflection right below the xy-electrodes of length l. The tip, however, is mounted at a distance l_2 from there. The remaining tube together with the tip holder serve as a rigid lever that forms the tangent of the bending section of the tube scanner. The fact that the tube bends into a circular shape and thus tilts the lever to an angle of $\alpha = 2\frac{\Delta xy}{l}$ (approximation for small angles) yields for the effective tip deflection Δxy_{eff}:

$$\Delta xy_{\mathit{eff}} = \Delta xy + l_2 \sin \alpha = \Delta xy \left(1 + 2\frac{l_2}{l} \right)$$ (3.4)

In the actual geometry of our set-up a deflection of $\Delta xy_{\mathit{eff}} = 6.34$ nm/V is calculated. This linear relation is only valid for small deflection angles, which are given here. Only when going to large scan ranges (e.g. $10 \mu m$), a non-linear term due to the spherical tip trajectory has to be taken into account. In large scans, this sphere is visible in the images, since the tip is held at constant height above the surface and thus the piezo is expanded more towards the edges of the image.

3.2 Calibration

To calibrate our 4-inch wafer STM we first investigated Si(111) and Si(001) surfaces, since these exhibit well known surface reconstructions. These reconstructions can be used as a calibration standard for the lateral dimensions, as they can cover reasonably wide areas of the surface. The Si(111) surface is especially suitable, because it is relatively easy to image the adatoms with atomic resolution. The (7×7) superstructure contains prominent cornerholes at a distance of 2.688 nm to each other.

The vertical calibration (z-piezo) can be accomplished using atomic steps that naturally occur on a crystal surface due to small deviations of the surface normal from a perfect crystallographic direction (miscut). Again, Si(001) as well as Si(111) surfaces can be used, as they form steps of a single atomic layer height (monolayer) or bilayer steps, respectively, under a wide range of miscut angles and preparation procedures.

In general for calibration a known voltage value that is applied to a piezo electrode is related to a known distance in the STM image.

On Si(111) the (7×7) reconstruction with its adatoms and the cornerholes could routinely be resolved (see Fig. 4-2, section 4.1). For xy-calibration the amplitude of the scan voltage ramp, which determines the range covered by the scan piezo and thus the physical image size, is measured with a digital storage oscilloscope. A distance across a certain number of Si(111) (7×7) unit cells is then measured in arbitrary units (e.g. number of image pixels) and the ratio between this and the corresponding piezo voltage is calculated, giving the calibration factor, which is also called piezo sensitivity. This is repeatedly done using different scan ranges. Care has to be taken that the microscope has reached an equilibrium state, where any drift either due to thermal expansion or piezo creep is absent. As result a calibration factor of $\Delta xy_{\mathit{eff}} = (6.12 \pm 0.12)$ nm/V has been determined, close to the theoretical value of 6.32 nm/V. With the RHK electronics, having a scan voltage sweep of 260 V_{pp}, this leads to a maximum scan range of 1.6 μm, using the linear extrapolation.

The z-calibration is performed in a similar way. Here, the z-piezo voltage that is generated by the feedback loop is recorded on a digital storage oscilloscope during line-scans across a

Table 3.1: STM calibration factors (sensitivities)

	calculated [nm/V]	calibrated [nm/V]	max. range [μm]
z-calibration	$\Delta z = 1.31$	$\Delta z = 1.38 \pm 0.05$	0.36
xy-calibration	$\Delta xy_{eff} = 6.32$	$\Delta xy_{eff} = 6.12 \pm 0.12$	1.6

bilayer step or a train of steps. The height of the corresponding voltage steps with respect to the known step height gives the z-calibration factor. One should make sure that the terraces between the steps are approximately leveled horizontally. Often the atomic features on the surface, which may be in the same order of magnitude in height as the steps themselves, make it difficult to actually determine the terrace surface. It is best to take an averaging line on each terrace, and also to average over many steps. We have done this on Si(111), where the bilayer step height is 0.313 nm, i.e. one third of the diagonal of the diamond lattice unit cell with $a_0 = 0.543$ nm. We obtained a z-calibration factor of (1.38 ± 0.05) nm/V. This experimentally determined calibration factor is slightly larger than the calculated one. The reason can be the limited accuracy of actual electrode length or a deviation of the piezoelectric constant from the specified value. The whole z-range covered by the piezo is again limited by the voltage range of the control electronics (± 130 V) yielding a maximum of 0.36 μm. In fact the imaging height it is further limited, because in our set-up the constant z-offset voltage is applied to the same electrode. That shows that our STM is particularly adapted to the investigation of rather smooth samples like they usually occur in epitaxial growth.

An overview of the calibration factors can be found in Table 3.1.

3.3 Tip preparation

The tunneling tips for measurements in ultra-high vacuum are always chemically etched from polycrystalline tungsten wire (diameter 0.25 mm). Two-molar sodium-hydroxide solution (2M NaOH) is used as electrolyte. A piece of stainless steel tube inserted into a 50ml Becherglass with the electrolyte serves as counter electrode, as shown in Fig. 3-2. The tungsten wire is immersed about 1 to 1.5 mm deep into the electrolyte in the center of the counter electrode. A DC voltage (6 – 12 V) is applied to the tungsten wire by the etching power supply. This power supply, that has been built following Ref. [29], also contains a fast switch-off circuit, that detects the end of the etching process. The highest etch rate occurs near the electrolyte surface at the air-electrolyte interface. Due to the electrolyte surface

counter electrode (-) / tungsten wire (+)

electrolyte 2m NaOH
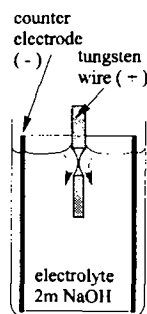
Fig. 3-2: Scheme of the set-up used for electrochemical tip preparation (drawing not to scale)

a) b)
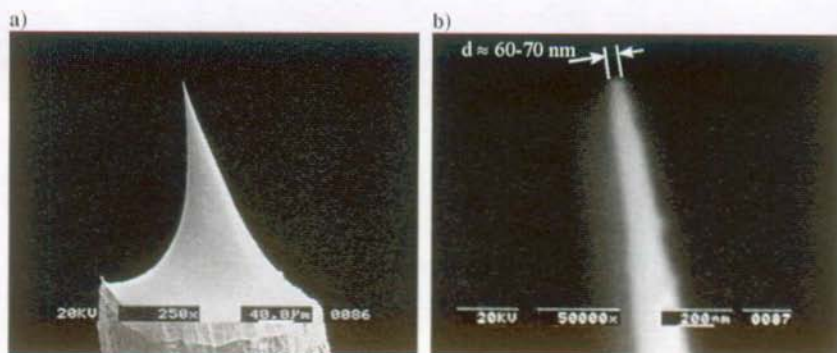
Fig. 3-3: Scanning electron microscope images of an electrochemically etched tungsten tip. a) shows the overall shape resulting from the etch, b) is a high magnification of the very apex. The radius of curvature of the tip apex is about $r \approx 30\text{-}35$ nm (diameter $d \approx 60\text{-}70$ nm).

tension, a meniscus is formed around the immersed wire. The etching usually leads to a parabolically shaped constriction of the wire near the surface region. When the wire diameter in this region has reduced to a value, where it can no longer hold the weight of the residual wire hanging below, the wire ruptures at its thinnest point. The drop-off of the lower wire part leads to a sudden increase of the resistance across the electrochemical cell, which is detected by the power supply. It immediately cuts off the DC voltage to prevent further etching, which would otherwise reduce the tip sharpness again. The specified response time of the switch-off circuitry is 15 ns. After etching, the remaining wire with the sharp tip is rinsed with deionized water. The wire is then cut to the suitable length that is necessary for placing it in the tip holder of the STM.

The etch in NaOH leaves a relatively thick (several nanometers) oxide layer on the tungsten, [30] which is removed in concentrated hydrofluoric acid (50% HF for about 1 minute). HF only reacts with the oxide and not with the metal itself, so the tip shape is unaffected or even improved by this step. [31] A thin natural oxide layer will form again after this etch, which has to be removed prior to imaging.

The final oxide removal can be easily performed *in situ* in the UHV chamber by a field emission process. A regulated DC high voltage applied between tip and grounded sample at a large (!) distance of several mm is used for this purpose. The emission current is observed via a current-voltage amplifier. Sharp tips show emission currents of several hundred μA at voltages around 500 to 800 V. This current leads to a local heating of the tip material at the apex, which removes the residual oxide. The heat together with the electric field can also rearrange the atoms at the tip apex and sharpen it. The emission current is used as an indicator for tip quality. Bad tips can be recognized before unsuccessful attempts to study a sample surface with it. However this procedure has to be carefully controlled, because the emission current depends strongly on the distance between tip and counter electrode and the applied

voltage (Fowler-Nordheim law). Excessive emission currents can melt the tip apex and cause it to become blunt rather than sharper.

A typical image of a W-tip manufactured this way can be seen in Fig. 3-3 after HF oxide removal but before field emission treatment. The scanning electron micrographs reveal the macroscopic parabolic shape of the tip (a) and at high magnification (b) the actual tip radius, which is in the range of 30–35 nm. With such tips atomic resolution could be routinely achieved on Si.

3.4 Resolution

The resolution of a scanning tunneling microscope is determined by a number of different limiting factors. Each of them has to be optimized in order to achieve the desired resolution. Such factors are the tip radius, the image pixel size, which is related to the voltage step resolution of the scan generator, the resolution of the data acquisition A/D converter and, of course, electrical or mechanical noise. The theoretical limit of resolution in absence of any instrumental deficiency is described by the Tersoff/Hamann theory for STM, which is in principal governed by the electronic structures of the tip |32| and the sample surface |33| on the atomic scale. It is strongly material dependent, especially in the case of semiconductors or semimetals. |34| So, the resolution limits of the instrumentation must be adequate not to obscure any features that could be in principal visible.

It is straightforward to obtain the z-resolution limit. This depends on the z-gain setting on the z-signal HV amplifier. At the lowest gain, the largest z-range can be covered (see Table 3.2). Since the amplifier output signal must fit into the input range of the data acquisition card, which has an A/D converter resolution of 12 bit (4096 discrete steps), the z-step resolution is lowest at the highest maximum range, namely 0.088 nm/digit for our microscope. This is of course much too coarse to image atomic corrugations, which may be in the order of 0.01 nm or less. To do so, the gain has to be raised. This means that the z-range that can be imaged decreases correspondingly. The maximum possible gain setting (for the RHK electronics) is 128 and thus the resolution can be improved by the same factor to $6.9 \cdot 10^{-4}$ nm/digit, which is largely sufficient to image atomic corrugations. However, in analog/digital conversion the least significant bit may easily be altered between its two

Table 3.2: z-piezo range and step resolution (value corresponding to the least significant bit) at different gain settings

Gain	z-range [nm]	z-resolution [nm/digit]
1	360	$8.8 \cdot 10^{-2}$
2	180	$4.4 \cdot 10^{-2}$
4	90	$2.2 \cdot 10^{-2}$
8	45	$1.1 \cdot 10^{-2}$
16	22.5	$5.5 \cdot 10^{-3}$
32	11.3	$2.7 \cdot 10^{-3}$
64	5.6	$1.4 \cdot 10^{-3}$
128	2.8	$6.9 \cdot 10^{-4}$

discrete states by small amounts of electronic noise. Thus it is not undoubtedly related to actual surface morphology. The guaranteed resolution is hence usually defined as twice the value of the single z-step resolution, corresponding to a change of the second bit.

Down to the physical limit mentioned above, the lateral resolution is mainly determined by the physical dimension of a pixel in the image. The typical size of an image is 256^2, 512^2 or 1024^2 pixels, independent of the chosen scan range. So the size of a pixel is the quotient of scan range and the number of pixels per line. In order to be able to resolve a surface feature properly, the feature must at least be twice as large as the pixel size. This argument corresponds to the sampling (Nyquist) theorem in real space.

The often worst limiting factor on the instrumentation side is noise, either electrical or mechanical. Both are reflected in the measured z-signal, the later because of true variations of the tunneling gap distance, to which the feedback loop responds. The electrical noise can either lead to mechanical noise within the STM when it couples into the piezo tubes, or it can directly couple into the feedback/amplifier part of the control electronics. Electronic noise from the outside world can be avoided by proper shielding of signal carrying wires within the whole set-up and a careful wiring of all components. The high-voltage sources for the piezos must be designed to have low noise. External mechanical noise, including acoustics, is prevented from reaching the STM by suspension and damping of the STM. In practice, both
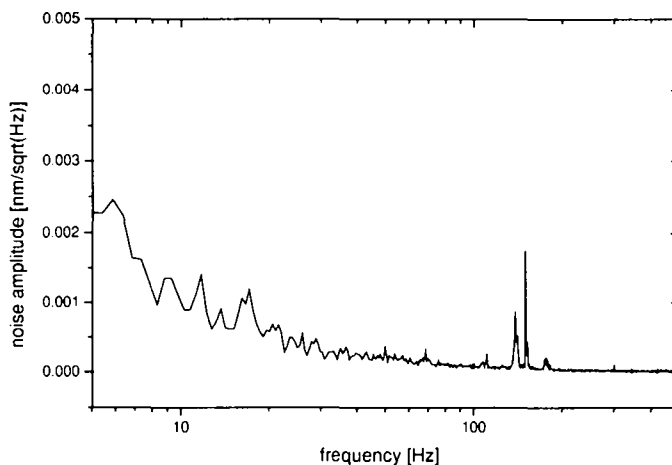
Fig. 3-4: Noise spectrum of the z-signal (topography) acquired while tunneling above a fixed position. The peak at exactly 150 Hz with an amplitude of 0.002 nm is the resolution limit. The sharp peak suggests, that it stems from electrical line noise (multiple of 50 Hz). However, the amplitude is small enough not to obscure atomic resolution on semiconductors. The high noise in the low frequency region is due to a back drift of the inchworm during acquisition of the spectrum. This drift was due to a manufacturing fault of the inchworm controller and has later been eliminated.

noise sources are often hard to distinguish.

A typical noise spectrum of the z-signal under static tunneling is represented in Fig. 3-4. It indicates, that the resolution limit of our instrument is determined by the peak amplitude of 0.002 nm at 150 Hz. Probably this peak arises from line noise, as it is an exact multiple of the mains frequency of 50 Hz. This amplitude corresponds to three digits in the highest gain setting of the data acquisition. Atomic resolution is not obstructed by this.

4 Pure Si surfaces

4.1 Si(111)

As mentioned in section 3.2, we used Si(111) (7×7) surfaces for STM calibration.
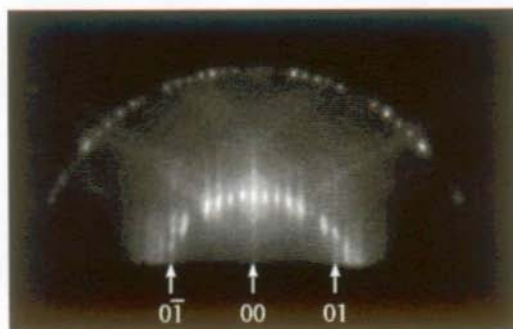
Fig. 4-1: RHEED pattern of a pure Si(111) (7×7) reconstructed surface after thermal desorption of the oxide layer (8 keV electrons, along a ⟨110⟩ direction, angle of incidence ~2.5°). Seven fractional-order superstructure-streaks are observed between the main streaks. The zero order and the 1/7th order Laue-circle are visible.
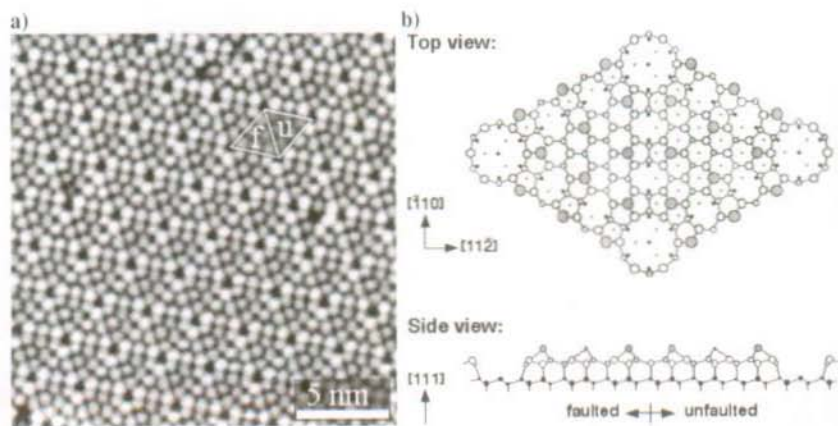
Fig. 4-2: a) Filled state image of a Si(111) (7×7) reconstructed surface (sample bias -1.5 V, 0.1 nA). The distance between two cornerholes (2.688 nm) is used as calibration standard. b) Schematic representation of the Si(111) (7×7) DAS-model (Dimer-Adatom-Stacking-fault-model) after Ref. [35]
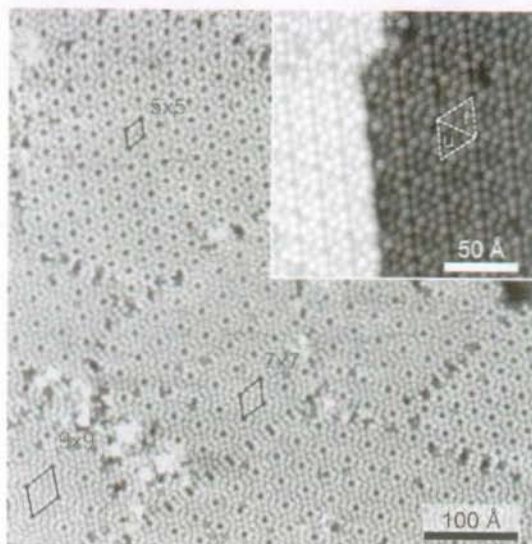
Fig. 4-3: Empty state image (+1.9 V, 0.1 nA) of a 150 nm thick Si layer on Si(111) grown at 600°C. During
growth domains of different DAS structures form, including (5×5), (7×7) and (9×9) reconstructions. The
inset shows a filled state image of a bilayer step (-0.85 V, 0.5 nA). The upper terrace is a (5×5) domain, the
lower a (7×7). Here, electronic contrast between the two halves of both DAS structure unit cells is observed.

Calibration samples consisted of Si(111) wafers with nominally no miscut. The wafers were
cleaned by an RCA clean [36] followed by a HF-dip for H-passivation before being
transferred to the MBE growth chamber. There they were heated to 650°C during 30 minutes
in order to desorb the hydrogen and hydro-carbides and subsequently to 950°C for 10 min for
desorption of oxygen via SiO formation. This treatment results in a clear (7×7) reconstruction
observed by RHEED (Fig. 4-1). After cooling down to room temperature samples were
transferred to the STM chamber. An image of this (7×7) surface is depicted in Fig. 4-2. The
twelve individual adatoms within the (7×7) unit cell are well resolved. A scheme of the dimer-
adatom-stacking-fault model [35] is also given in the same figure. One half of the
reconstructed unit cell contains a stacking fault, that manifests itself in the different apparent
heights of the adatoms in the faulted (f) and unfaulted (u) halves. This is an electronic, not a
real topographic contrast and is only seen when tunneling from filled electronic surface states
to the STM tip.

Fig. 4-3 shows a 150 nm thick Si film grown onto Si(111) (7×7) at 600°C at a growth rate
of 1 Å/s. One can see the formation of domains containing different reconstructions of DAS-
structures [(5×5), (7×7), (9×9)]. This mixture is typical for low temperature homoepitaxy on
Si(111) (7×7). [37] In the large empty state image no height difference between faulted and
unfaulted half is obtained. Individual adatoms are imaged even at the boundaries of the bilayer

steps, indicating the perfect lateral resolution of our instrument. The resolution in z-direction is much better than 0.1 Å, estimated by comparing the different apparent heights of the faulted and unfaulted halves with the known bilayer step height. This can be seen in the filled state inset of Fig. 4-3 where the faulted halves of the (7×7) and (5×5) unit cells appear a little brighter than the unfaulted ones.

4.2 Si(001)

Compared to Si(111), Si(001) surfaces are without doubt the technologically more important surfaces. Si(001) substrates are commonly used in standard Si VLSI technology, because of the natural oxide (SiO_2) occurring on this surface and the smooth Si/SiO_2 interface, which is essential as an isolation layer in today's integrated electronic circuits. In addition, Si(001) is easier to clean and has favorable wet-etching properties for device fabrication.

Since in this work all growth experiments have been carried out on Si(001), the basic properties of this surface, that are of interest with respect to the following chapters, are briefly resumed in this section.

Basics of Si(001) 2×1 and related reconstructions

On Si(001) adatom diffusion is highly anisotropic, having a direct impact on epitaxial growth, reflected in the obtained surface and step morphology. This anisotropic diffusion is caused by the surface reconstruction.

Since the bulk symmetry is broken at the crystal-vacuum interface, the formation of new surface symmetries may be energetically favorable over a bulk termination of the surface. The formation of new surface unit cells, whose surface lattice constants are larger than in the bulk, is called reconstruction. Covalently bound materials such as semiconductors like Si and Ge are typical examples. The reason for reconstruction are the non-terminated, so-called dangling bonds, that reach out into the vacuum at the surface. From an energetic point of view it is more favorable for the surface to reduce the number of dangling bonds. This can be accomplished by the rearrangement of atoms within several atomic layers [like on Si(111)] or, simpler, by a rebinding of adjacent adatoms of the topmost layer, which reduces dangling bonds by a factor of two. This type of reconstruction is observed on many pure (Si, Ge) or compound III-V and II-VI semiconductor surfaces. Because it forms supercells containing two times one adatom, or an ad-dimer, it is named (2×1) reconstruction following the Wood- notation. [38]. Fig. 4-4 shows a scheme together with STM micrographs of this dimerized surface. The Si-dimers are aligned into dimer rows along the ⟨110⟩ directions. Dimer rows on terraces that are separated by a monatomic step run in perpendicular directions, a simple result of the symmetry of the diamond-like lattice. On a clean Si(001) surface the dimers appear as rather symmetric elongated protrusions in filled state STM images at room temperature [Fig. 4-4 b)]. However,

if impurities or defects are present on the surface, like contaminants or missing dimers, the dimer rows show buckling, i.e. single dimers appear asymmetric. Neighboring dimers are tilted in the opposite direction forming a zigzag pattern along the rows [Fig. 4-4 c)]. Depending on the buckling directions of adjacent rows, this can lead to c(4×2) or p(2×2) structures for rows being out of phase or in phase, respectively.

A buckled configuration of the surface dimers is today believed to be the stable lowest energy configuration at zero temperature. [39] The dimer bond is tilted at an angle of about
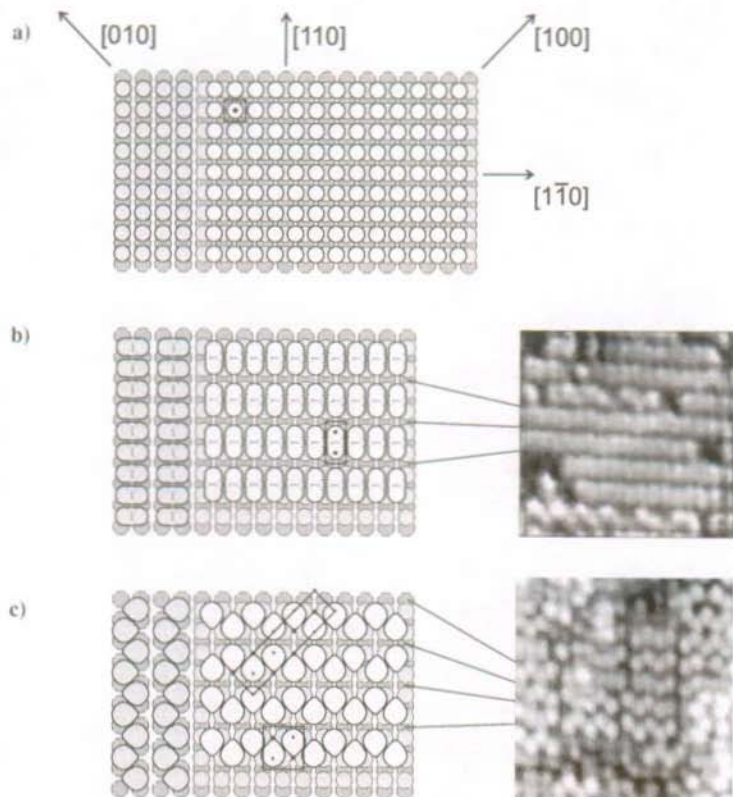
Fig. 4-4: Schematic ball representation of the reconstructions on Si(001). The distance of adjacent balls is the in-plane lattice constant of 0.384 nm ($a_0/\sqrt{2}$). a) shows the bulk symmetry which does *not* occur at the surface of pure Si(001). It is only observed on H-passivated Si(001). b) Instead, adjacent surface atoms pair into ad-dimers that are aligned in rows [(2×1) reconstruction]. These dimer rows run in perpendicular (110) directions on neighboring terraces due to the diamond lattice of the bulk crystal, as indicated by the white and gray dimer rows on the upper and lower terrace in b), respectively. c) If the rows are disturbed by impurities like missing dimers, the dimers become asymmetric and arrange into a zigzag like pattern called dimer buckling. The resulting reconstruction depends on the phase between adjacent rows of buckled dimers. In phase they build a p(2×2), out of phase a c(4×2) as indicated by the small lower and the larger upper surface unit cell in c).

16° which causes one dimer atom to protrude roughly 0.6 Å above the other. At room temperature, however, the dimers are thermally activated to switch at high frequency (hv ~ 25 meV) [40] between their two equivalent configurations. So usually the STM measures a time average, which appears symmetric. At surface defects the dimers are pinned to a certain buckling direction and thus the oscillation is inhibited. The buckling can then be seen in STM.

The rebinding of the adatoms into dimers obviously distorts the usual tetrahedral bond geometry of the bulk material by changing bond lengths and angles of the involved atoms. The resulting strain induced by the dimers extends into the bulk as far as four atomic layers. [41] The bulk atoms lying under the dimer rows experience compressive strain, and on those lying between the rows tensile stress is exerted.

For the preparation of the Si(001)-wafers a standard procedure was used. It consists of a Caros clean (50% H_2SO_4 and 50% H_2O_2) to oxidize the surface, a rinse in DI H_2O followed by a dip in concentrated HF to remove the oxide and passivate the surface with hydrogen. The cleaned wafers are loaded into the vacuum chamber, where hydrogen is desorbed by heating the sample to 650°C for 10 minutes and to 950°C for 30 min, subsequently. This procedure results in the clear streaky (2×1) RHEED pattern of clean Si(001). Fig. 4-5 represents a Si(001) surface directly after substrate preparation. Single dimers are clearly resolved within the dimer rows (corrugation ~0.1 Å) when tunneling through occupied sample states. The inset of Fig. 4-5 is taken at a positive sample bias, hence tunneling to unoccupied states. In this empty state image, where additional depressions appear in the center of the dimer rows, the symmetry of the unoccupied antibonding states of the dimers is visible, [42] as it is frequently observed with very sharp tips. Each protrusion corresponds to the empty state of a single dimer atom. These images also demonstrate the high resolution, although the surface exhibits a rather large number of defects seen as missing dimers or as starting points for dimer buckling. This is probably due to insufficient sample cleaning or contamination from the residual gas.

Consequences for global morphology

The global morphology of a clean Si(001) wafer is usually governed by a train of atomically flat terraces that are separated by monatomic steps. This stepped surface arises from the misalignment of the surface normal from the ideal crystallographic (001) surface (miscut), a consequence of the wafer manufacturing and polishing process. For a standard (001) wafer used for device production the miscut angle is typically specified to lie within ±0.2° off the ideal direction, but there are also wafers only specified to ±1°. Fig. 4-6 a) gives an example of such a surface. From the average spacing of the steps (40 nm) the miscut angle can be determined to be 0.2° for this sample. As already mentioned, the dimer rows along ⟨110⟩ run in perpendicular directions on adjacent monatomic terraces. Thus, two types of monatomic steps can be distinguished: those where the rows on the upper terrace are parallel to the step edge and those ending with the dimer rows perpendicular to the step edge. They are named S_A and S_B steps respectively, following the notation of Chadi. [43] Pure alternating S_A
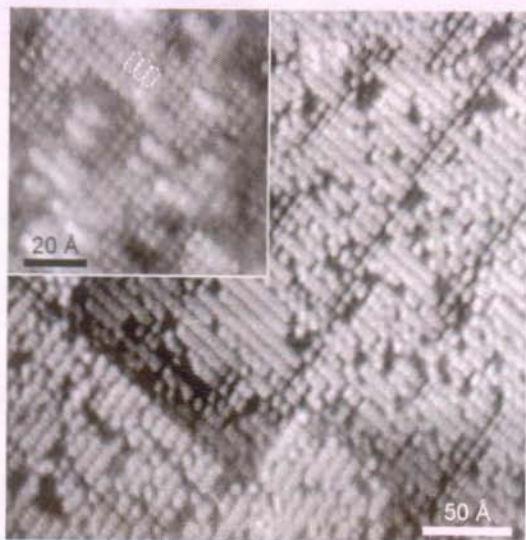
Fig. 4-5: STM images of a Si(001) wafer surface. The (larger) filled state image (-1.88V, 0.2nA) reveals the dimer rows with partially buckled and symmetric dimers. A monatomic S_B step can be seen in the lower left part of the image. On the higher terrace the rows run perpendicular to the rows on the lower one. The inset shows the unoccupied states at 0.85V, 0.2nA, where the single atoms within a dimer can be resolved.

and S_B steps can only be obtained when the surface normal is tilted exactly towards $\langle 110 \rangle$. Thus normally each step is a mixture between both types, having segments of S_A and S_B character, as seen in Fig. 4-6 a), where the surface is approximately tilted towards [100].
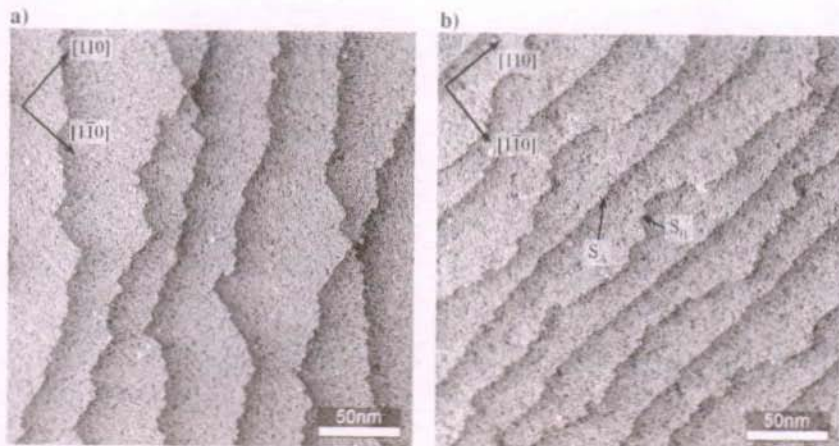
Fig. 4-6: a) Stepped Si(001) surface as obtained directly after in situ cleaning and b) after growth of a 150 nm thick Si layer at 750°C. In a) the average tilt angle is 0.2° towards [100].

S_A steps are generally smoother than S_B steps, i.e. they contain less kinks and corners, which is a result from the anisotropy of the surface. On a terrace the adatom diffusion along the dimer rows is favored over diffusion across the rows. [44] The barrier (Schwoebel barrier) for an adatom moving down a S_B step is lower than for a S_A step. In addition, an adatom on a lower terrace reaching an S_A step of the higher terrace can diffuse perpendicular to the dimer rows along the S_A step more easily than without the presence of the step and is preferentially incorporated at the end of the S_A step, which has S_B character. [45] The smoothing of the S_A parts of the step train can be recognized in Fig. 4-6 b), where the same wafer as in a) is shown after growth of 150 nm of Si at a substrate temperature of 750°C. The fact that no islands are present on the terraces indicates a pure step-flow growth, which means that the impinging atoms are all incorporated at the steps, because their diffusion length is longer than the average terrace width. What is also observable in Fig. 4-6 b) is, that the tilt angle and direction have, at least at the location where this 250 × 250 nm image has been taken, changed to 0.26° towards [1 $\bar{1}$ 0]. This may be induced by a not perfectly homogeneous flux distribution across the wafer, leading to different step directions on different locations after the growth of such thick films.

5 Carbon on Si(001)

The incorporation of C into Si with the aim to achieve high quality $Si_{1-x}C_x$ films with high content of substitutional carbon on Si(001) substrates has been the subject of many studies during the past few years. [46, 47] Although both, Si and C, are group IV elements forming the same lattice structure, the equilibrium solubility of C in Si is very small, i.e. only in the order of 10^{-4} atomic % [48] due to the very large lattice mismatch between the two bulk materials ($\sim$35%). Hence, in order to get a high C concentration in the range of a few percent, one has to use growth methods that operate far from thermal equilibrium. MBE is the method that has been most widely applied for this purpose. Coevaporation of Si and C [49-52] as well as deposition of 1-2 ML pure C with subsequent Si overgrowth [46, 53] have been successfully used to fabricate C-rich $Si_{1-x}C_x$ quantum wells. Along with such experimental investigations, several theoretical studies about the distribution and atomic positions of substitutional C in bulk Si and $Si_{1-x}C_x$ films have been reported. [41, 46]

However, so far very little is known about C incorporation onto or into the Si(001) *surface* in the submonolayer regime, as the above mentioned reports all deal with C readily incorporated in a $Si_{1-x}C_x$ layer. The first theoretical approach taking into account the influence of the Si(001) surface properties on C incorporation, starting from a complete ML of C on Si(001), has been given in Ref. [54]. Theoretical or experimental studies of lower C coverages deposited under epitaxy conditions have not been reported by now. The fact, that C *sub*monolayer coverages on Si(001) lead to interesting consequences for subsequent Ge island nucleation on this surface, [11] makes detailed studies of the structure and properties of the C/Si(001) system particularly interesting. The knowledge of this system's properties is a prerequisite for the understanding of Ge nucleation on this surface, that will be described in the following chapters.

In this chapter a combined experimental and theoretical study of the initial stages of C deposition on Si(001) substrates is reported. Carbon is discovered to cause an unusual c(4×4) reconstruction. A structural model is proposed backed by detailed density functional theory (DFT) calculations that can account for all the observed experimental results. This model involves the pairing of surface Si dimers mediated by the presence of C dimers bound to subsurface C atoms, and gives rise to electronic charge distributions that agree with the scanning tunneling microscopy (STM) images.

5.1 Calibration of the carbon source

The knowledge and control of the carbon flux is crucial for all the following experiments. So a careful calibration of the C source is necessary in order to be able to reproducibly and accurately produce the sub-monolayer coverages of C. As already mentioned in the previous chapter, the carbon source (SUKO 63) consists of a meander-shaped filament machined from a highly oriented pyrolithic graphite (HOPG) plate. The filament is directly heated by DC current passing through it and the carbon simply sublimates from the filament, thus producing the deposition flux. Due to the high temperature needed for significant carbon sublimation, which is about 2000 – 2200°C, and due to the low heat capacity of the filament, a stable source control by temperature feedback is difficult. Instead the source is simply operated in a constant current mode. The constant current yields a constant filament temperature and, hence, a constant C sublimation rate. The typical value used for all samples of this work is a current of 100 A at a supply voltage of about 14 V, which is close to the maximum power allowed for this source according to the manufacturers specifications. This yields a deposition rate of about $2.3 \cdot 10^{-4}$ ML/s. The thickness of the deposited C-layers is then controlled only via the deposition time.

Fig. 5-1 demonstrates the good reproducibility of C deposition on a sandwich sample containing 8 layers of 0.047 ML of pure C, separated by Si spacer layers of 17 nm thickness. The deposition time per carbon layer was 240 s, yielding a flux of $1.95 \cdot 10^{-4}$ ML/s. The layer thickness achieved for all layers is reproducible within 2%.

However, the latter flux value is 15% lower than that determined 10 months earlier in equivalent samples containing 0.11 ML C, as shown in the inset of Fig. 5-1. That means, the flux is subject to a certain degradation over longer time periods. At first sight one would rather expect the flux to increase instead of decrease with operation time, simply because the filament becomes slightly thinner due to material sublimation loss. This would cause the resistance to go up and thus, at constant current, the power to increase, resulting in higher filament temperature and higher flux. In fact a slight increase of the needed voltage over the time from initially 13.9 V to 14.3 V for 100 A filament current could be observed. However, not only the filament itself may be subject to the degradation, but also the contacts between the different materials involved in the current path of the source (like stainless steel > tantalum rods > graphite blocks > filament), that are partially only clamped together, may worsen, absorbing more power without contributing to the carbon flux. Possibly, also the shape of the flux distribution may change due to small changes of the filament shape, thus being the reason for reduced deposition rate at the sample position. Anyhow, the flux decrease at constant current shows, that the carbon source has to be recalibrated from time to time.
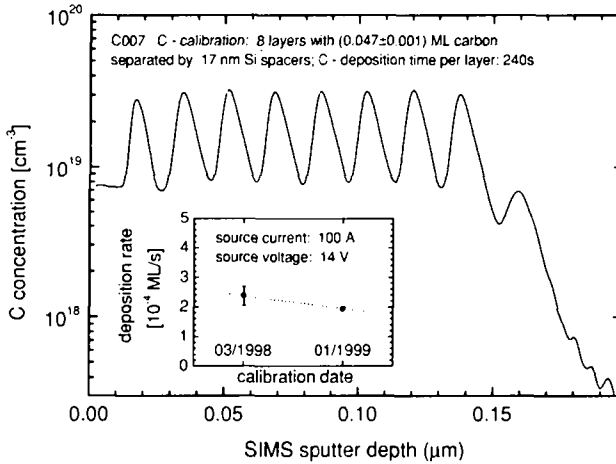
Fig. 5-1: Example of a SIMS calibration of C-content in an eight period sandwich structure. Within the structure the reproducibility of the C-content in each layer is 2%, which is better than the accuracy of the SIMS measurement itself (~ 5%). However, the inset demonstrates a slight degradation of the flux over a long time period. From two SIMS calibrations within 10 month, a decrease of deposition rate by about 15% is determined.

Nevertheless, as samples of the same series are usually grown within a short time of several days or weeks, the good flux reproducibility is still given. For all samples presented in this work, the error in the absolute C coverage value is estimated to be less than 10%.

The dependence between C deposition rate and source current has also been measured. Flux increases slightly slower than exponentially with current. Going from 90 A to 100 A gives a flux increase by a factor of five with an almost linear behavior. But as the deposition rate is already low at 100 A, and using even lower flux would lead to unreasonably long deposition times, the current dependence has not been evaluated in detail.

Another effect that has to be taken into account especially at short C deposition times is the occurrence of a flux transient after opening the source shutter. This effect is due to the different thermal equilibria with closed and open shutter. Closed shutters reflect part of the radiated heat and, hence, lead to higher source temperature. This higher temperature equilibrates to a new steady value within a certain time after shutter action. For the carbon source, the initial flux decays from about twice the steady state value exponentially towards the new equilibrium. The time constant of this decay has been determined to be $\tau \cong 20$ s by evaluating SIMS measurements of several C layers with different deposition times. The consequence of this flux transient effect on C-layer thickness can be neglected when deposition times are longer than about 200 s.

5.2 Identification of the C-induced c(4×4) reconstruction

Experiments were carried out in the MBE system described in chapter 2. Si(001) wafers were treated with the standard procedure mentioned above. Prior to C deposition, a 200 nm thick Si buffer is grown at a substrate temperature of 550°C to 750°C. Some large scale scans have shown on earlier samples, that Si buffer layers grown at 550°C tend to form long-period undulations on the surface with a large lateral periodicity of about 500 nm and undulation height of ~1-3 nm. Period and direction of the undulation depend on the (arbitrary) miscut of the substrate. This is probably due to a step bunching instability during buffer growth (although this has only been reported and predicted for heteroepitaxial strained layer growth). An increase of the buffer growth temperature to 750°C, however, solved this problem and lead to smooth Si epi-layers, as this is desired for the study of subsequent C and Ge deposition. After the buffer growth, the sample is cooled down to 550°C within 3 minutes. The sub-monolayer coverage of carbon is then deposited at a deposition rate of $3.3 \cdot 10^{11}$ atoms/s (or $2.3 \cdot 10^{-4}$ ML/s) at a substrate temperature of 550°C, calibrated by secondary ion mass spectroscopy. This flux corresponds to a power of 100 A at 14 V = 1.4 kW on the C sublimation source. A coverage of 0.11 ML takes about 480 seconds. The accuracy of the C coverage is estimated to be about 10%. After C deposition the samples are cooled to room temperature and transferred to the STM-chamber without breaking ultra-high vacuum.

Fig. 5-2 shows STM-images of a Si(001) surface covered with 0.11 ML C. The striking features for both filled states (sample bias –2 V, current 0.2 nA) and empty states (+2 V,
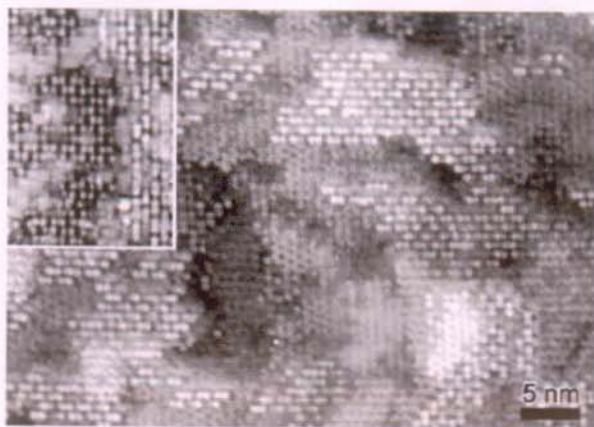
Fig. 5-2: Filled state STM image (–2 V, 0.2 nA) after deposition of 0.11 ML C on Si(001) at a substrate temperature of 550°C and a deposition rate of $2.3 \cdot 10^{-4}$ ML/s. Areas covered with elongated pairs of bright spots lying in ⟨110⟩ directions exhibit a c(4×4) structure. The inset shows empty state data (+2 V, 0.2 nA), which exhibits essentially the same paired spot pattern.
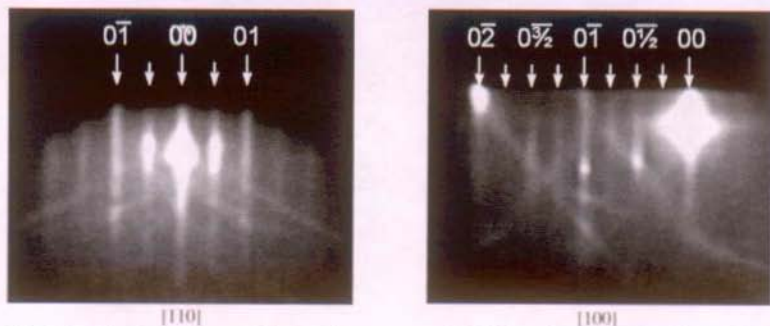
Fig. 5-3: RHEED pattern of a partially c(4×4) reconstructed Si(001) surface after deposition of 0.11 ML carbon. The azimuth of the electron beam is indicated. In ⟨110⟩ the four fractional order streaks between the integer reflexes are observable.

0.2 nA; see inset) are the elongated pairs of bright spots that are arranged into patches of a c(4×4) superstructure. In between these areas, the surface exhibits a Si buckled dimer reconstruction. Both reconstructions can coexist in the same atomic layer. Reflection high-energy electron diffraction measurements (RHEED) confirm the c(4×4) symmetry, as seen in Fig. 5-3. Three fractional order streaks are visible between the main RHEED reflexes in ⟨100⟩ azimuths. Along ⟨110⟩ the electron beam experiences a periodicity of two a_0 because the paired spots are repeated at this distance in adjacent rows, thus only showing half order streaks like on (2×1).

An enhancement of surface roughness is observed for the C covered surface compared to the initial pure Si(001) (2×1) surface, demonstrated in Fig. 5-4. Already at a carbon coverage of 5% of a monolayer a pronounced roughening of step edges is found coming along with larger voids on the terraces [a)]. At a carbon coverage of 0.11 ML elongated islands of single
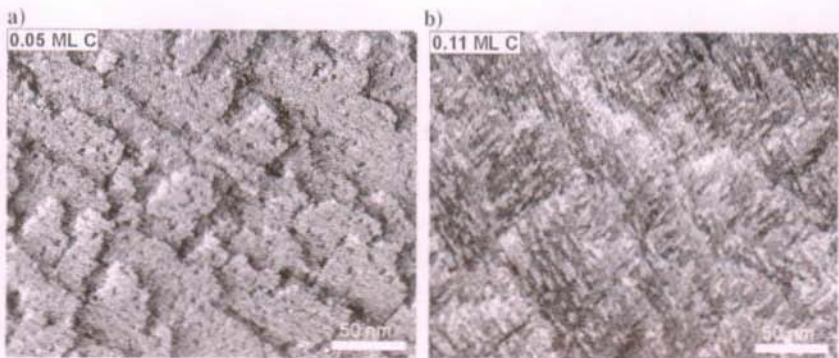
Fig. 5-4: global morphology of Si(001) after deposition of 0.05 and 0.11 ML carbon. Image sizes are 280×220 nm². The tunneling condition are a) 2.6 V, 0.2 nA and b) -2.0 V, 0.17 nA.
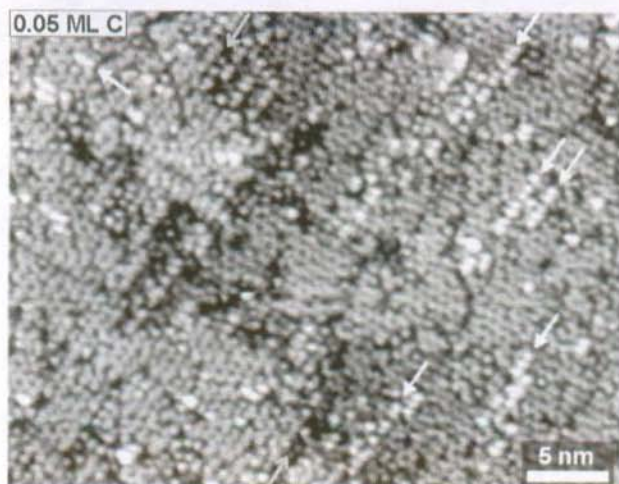
Fig. 5-5:   0.05 ML carbon on Si(001), filled state image (-2.0 V, 0.2 nA): Si dimers appear entirely buckled. A
small number of paired bright spots characteristic for the c(4×4) reconstruction can be found emerging at
steps or forming on top of a terrace (indicated by white arrows). Beginning and end of a step is indicated by
gray arrows. Rows of missing Si dimer defects perpendicular to the dimer rows are present on the terraces,
possibly reducing the tensile strain that arises from carbon incorporation.

monolayer height appear on the terraces [b)]. Most of these islands show a mixture of dimers
and c(4×4) reconstruction.

The observation of a c(4×4) reconstruction on Si(001) has been reported by several authors
after thermal treatment following an oxygen [14] or hydrogen [15, 55], exposure or even pure
thermal treatment [16]. It was usually assigned to a metastable pure Si structure. Only recently
Miki et al. [17] suggested that it might have been caused by carbon impurities.

The experiment shows that the number of the paired spots changes drastically with the
amount of deposited carbon. At 0.05 ML C only a few such pairs are observed, mainly at step
edges (see Fig. 5-5). Occasionally short chains of the spot pairs are found on the terraces. The
remaining Si surface consists entirely of buckled dimers in contrast to symmetric dimers on
bare Si(001) (2×1), when tunneling from the filled states, i.e. at negative sample bias. This is
known to be caused by the presence of impurities [56]. Carbon obviously acts also as impurity
inducing buckling. In addition, the Si surface shows a large number of defects in form of
missing dimers. The missing dimer defects often arrange into chains perpendicular to the
dimer rows. This may serve for a reduction of the tensile strain that is induced by
incorporation of carbon into the surface.

At 0.11 ML, however, already more than 10% of the surface is covered with the c(4×4)
pattern (see e.g. Fig. 5-2). This demonstrates, that the formation of the c(4×4) reconstruction is
definitely caused by the C deposition. Moreover, a certain number of C atoms has to come
together within a c(4×4) unit cell to produce the superstructure, arranged either on surface or
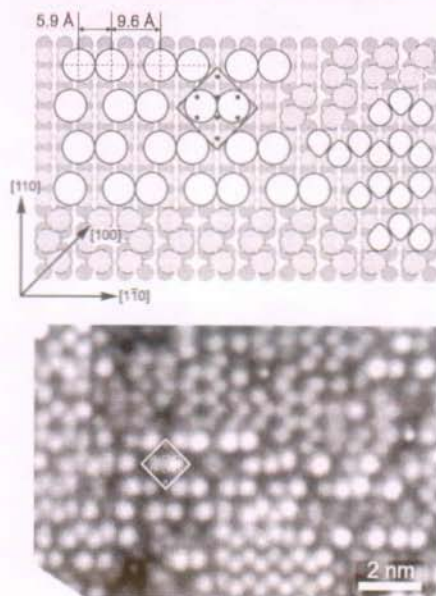
Fig. 5-6: schematic representation and high resolution STM picture of the symmetry and positions of the spot pairs within the c(4×4) pattern. The rhombi with the eight black dots indicate the unit cell with its ideal unreconstructed atom positions.

subsurface sites, which is much more likely to occur at higher coverage. Our findings are very similar to those reported recently by Butz and Lüth. [57]

The curious feature in the STM images that is difficult to explain, at least in terms of the typical structures on the Si(001) surface, is the presence of two bright spots per c(4×4) surface unit cell at an apparent height of about one ML above the previous layer. The two spots appear in pairs with an intrapair distance equal to 5.9 Å and an inter-pair distance of 9.6 Å. The distance between successive pair centers is 15.5 Å, which is the normal length of four times the basic repeat distance on the unreconstructed (001) surface $(4 \cdot a_{0(Si)}/\sqrt{2}; a_{0(Si)} = 5.43 Å)$ within 1% accuracy. A scheme and a high resolution STM image is given in Fig. 5-6. The intrapair distance is far too long to correspond to any kind of interatomic bond. Furthermore, the surface unit cell covers eight atomic sites in the unreconstructed geometry. These observations argue that the bright spots cannot be associated with single atoms. We propose that the paired spot structure corresponds to two Si dimers, which would normally be at a second neighbor distance, i.e., 7.7 Å apart, and have come closer together at a distance of 5.9 Å due to strain induced by incorporation of substitutional C atoms in the Si lattice.
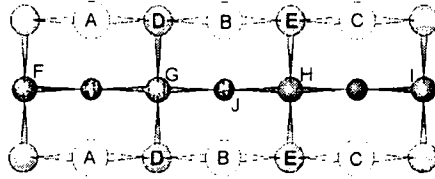
Fig. 5-7: Schematic top view of the atomic arrangement along the diagonal of a c(4×4) unit cell in the unreconstructed case. The atoms of the topmost four atomic layers are represented by circles, decreasing in size and brightness from top to bottom. The labeled atoms are those considered in the different models according to Table 5.1.

5.3 Model structures for the c(4×4) reconstruction

The remarkable displacement of the Si dimers by 1.8 Å towards each other is a very significant distortion and cannot be easily rationalized, especially in the case of a covalently bound semiconductor. To account for this distortion a number of structural models have been considered that could potentially produce the desired effect. The presence of the dimer reconstruction on the pure Si(001) (2×1) surface produces a pattern of strain in the substrate, with certain sites (those directly under the surface dimers) under compressive stress, and other sites (those between dimer rows) under tensile stress. This pattern of opposite stresses can lead to interesting ordering effects in semiconductor alloys. [58] However, the very large strain induced by substitutional C atoms is such that a very strong repulsion results between C atoms at first neighbor sites below the top two surface layers. This repulsion can substantially reduce the ordering produced by the surface reconstruction. [54] All these considerations have been taken into account when constructing models that could potentially reproduce the experimental features. The important features of the models that have been considered are illustrated in Fig. 5-7. A c(4×4) unit cell covers the area of eight lattice sites. So it could contain a maximum of four surface dimers. Due to the symmetry observed in the STM images it is assumed that there is at least one dimer missing from the surface layer, i.e. the atom positions in the top and bottom cor-

Table 5.1: Occupation of surface and subsurface sites identified in Fig. 5-7 by silicon or carbon atoms. A dash (-) indicates the site is unoccupied.

					Site					
Structure	A	B	C	D	E	F	G	H	I	J
(a)	Si	–	Si	Si	Si	C	Si	Si	C	C
(b)	Si	–	Si	Si	Si	C	C	C	C	Si
(c)	Si	–	Si	Si	Si	C	C	C	C	C
(d)	Si	–	Si	Si	Si	Si	C	C	Si	C
(e)	C	–	C	Si	Si	Si	Si	Si	Si	Si
(f)	Si	–	C	Si	Si	C	C	Si	Si	Si
(g)	Si	C	Si	Si	Si	Si	Si	Si	Si	Si
(h)	Si	C	Si	C	C	Si	Si	Si	Si	Si

ners of the rhomb-shaped unit cell are unoccupied. Hence, there are at most three surface dimers. These remaining dimers are made up from atoms at the top sites labeled A, B and C in Fig. 5-7, that make up the diagonal of the unit cell. Sites D and E lie in the second layer. The sites labeled F, G, H and I in the third layer, and site J in the fourth layer, are all under compressive stress due to the surface reconstruction.

Eight different models were considered with different amounts of carbon atoms incorporated in the Si lattice (Table 5.1). The models fall into two groups: in the first group |models (a)–(f)|, the sites labeled B are unoccupied. The remaining two dimers at sites A and C are either silicon or carbon dimers. In the second group |models (g)–(h)|, the sites labeled B are occupied by carbon atoms, i.e., there are three dimers in the unit cell, two Si dimers and one carbon dimer. The sites not being labeled are always occupied by Si atoms. The placement of C atoms in the different sites was guided by two considerations: (i) carbon atoms were placed in sites that are compressively stressed due to the surface reconstruction, and (ii) they were situated in positions that are likely to lead to a pairing of the two Si dimers at sites A and C, which could then explain the observed STM images.

In models (a)–(d), there are only two surface dimers which are composed of two Si atoms each, with various amounts of C atoms at sites F–J, placed so as to induce subsurface distortions that could potentially bring the surface Si dimers closer together. In model (e) both surface dimers are composed of C atoms. In model (f) one surface dimer is composed of C atoms and the other of Si atoms; the latter model also has two C atoms in the third layer. Model (g) has three surface dimers, the outer two of them composed of Si atoms at the sites A and C, and the middle one composed of carbon atoms at site B. The shorter bond of this latter dimer will induce strain that could bring the Si dimers closer together. Finally, model (h) has the same atomic arrangement at the surface as model (g), and in addition has carbon atoms at the subsurface sites D and E. This introduces altogether five carbon-carbon bonds in a complex of six C atoms, which will induce a strain that will pull atoms around this complex closer to its center.

5.4 Evaluation of the models

The models described above have been evaluated by investigating the total energies and the thermodynamic stability. In addition, calculations of the electronic charge density of the structures in the bulk and on the surface have been performed, based on pseudo-potential density functional calculations. The computer calculations have been done by Prof. Dr. Efthimios Kaxiras from Harvard University at the computer center of the physics department at University of Crete, Heraclion. |59| The DFT calculations were carried out in the local density approximation. Norm-conserving pseudopotentials have been used to describe the interactions between the valence electrons and the ion core. The system is modeled by a slab

geometry containing eight atomic layers in ((X)1) direction. The bottom atoms of the slab are terminated with hydrogen atoms, the lattice constant being fixed to that of bulk Si. The topmost atomic layers contain the proper arrangement of C and Si atoms characteristic for each model. Slabs are separated by a vacuum region of 12 Å, leading to periodic boundary conditions in the calculation. In an iterative calculation process, the total energy is optimized until it converges towards its minimum value. This is done using the Car-Parrinello scheme. [60] The iteration comprises the following steps. First, the atomic positions within the initial structure are allowed to relax to the lowest energy positions. This is done by deriving in a first fully self-consistent calculation the charge density and electronic wavefunctions by solving the Kohn-Sham equation, from which the forces acting upon the ions (Hellmann-Feynman forces) can be derived. These forces are then reduced by calculating the relaxed and thus slightly different positions applying a conjugate gradient algorithm. [61] The total energy of this new configuration and its charge density distribution is then calculated again, i.e. the Kohn-Sham equation is solved again, the ionic forces are derived again, the structure is relaxed further and so on. In this iterative way, the total energy is optimized. By taking small steps in the ionic relaxation according to the calculated Hellmann-Feynman forces, and evolving accordingly the electronic degrees of freedom through the Car-Parrinello lagrangian, only very few steps of electronic optimization are needed, leading to a fast convergence of the total system to its lowest energy ionic and electronic state for a given configuration. Finally, after this procedure the total energy of the particular structure, its charge density distribution and the relaxed atomic positions have been determined. (the computational parameters are the same as in Refs. [54] and [41]).

Gray-level plots of the surface charge density distributions of all models are depicted in Fig. 5-8. They were created using an energy window of 2.5 eV below the Fermi level, thus being comparable to STM images with about -2 V sample bias. Calculations have been restricted to occupied states, as the experiment shows that the c(4×4) structure considered here is rather insensitive to the bias sign. Filled state and empty state images show the same overall features. Furthermore, for empty states the calculation tends to converge very slowly. The charge density contours have been convoluted with a Gaussian to account for limited STM-tip resolution in the experiment.

In all cases the two surface dimers appear more or less asymmetric, which is a result of the asymmetric relaxation of the surface atoms. In cases (e)–(h), where there are one or two surface dimers composed of carbon atoms, these are *not* visible. Even in case (e), where there are just two C dimers on the surface, what is visible are their back bonds to their nearest neighbor Si atoms. This interesting effect, i.e. the invisibility of C–C dimers to STM when Si–Si dimers are also present on the surface, is due to the lower geometric position of the atoms and the lower energy of the bonding states of the C–C dimers. The short bond length of C–C bonds causes the carbon surface dimers to lie essentially at the same height as the second-layer Si atoms to which they are bonded. (see also Ref. [41])
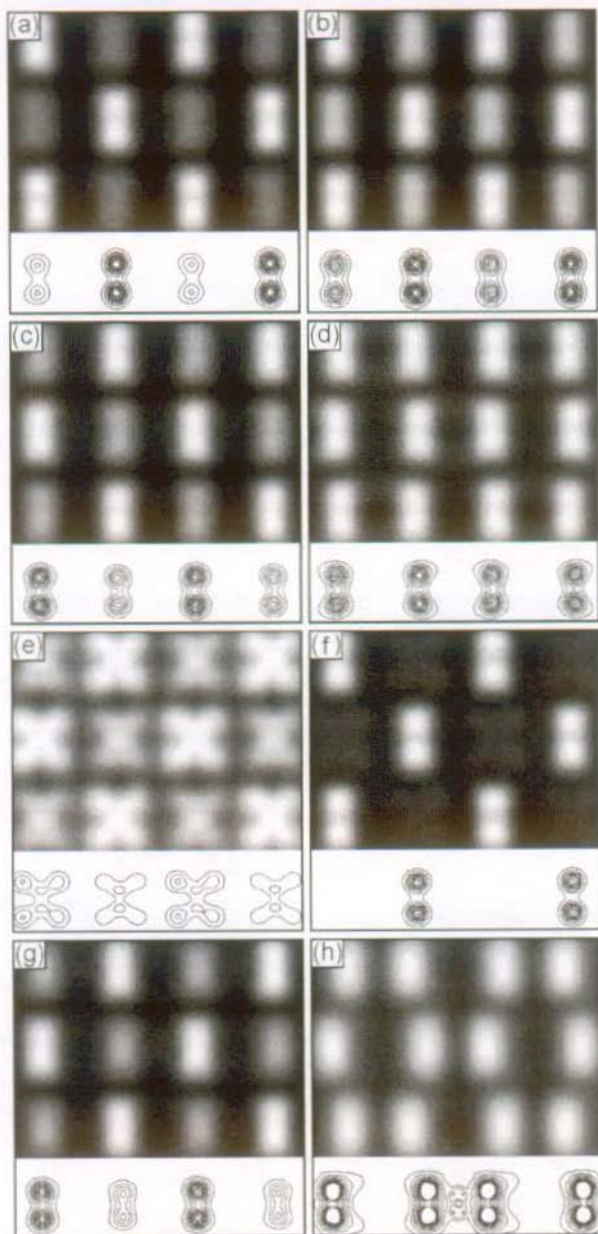
Fig. 5-8: Calculated surface charge density distributions of the models (a)–(h), corresponding to simulated STM images for occupied states. The contour plots reveal the detailed charge density around the atoms. Gray level representation of the contour plots are convoluted with a Gaussian to account for limited STM tip resolution. Bright white indicates high charge density. Only structure (h) is consistent with the observed STM images.
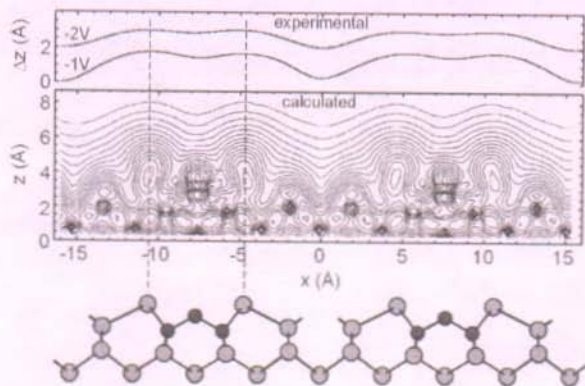
Fig. 5-9: Cross-sectional contour plot of calculated charge density in a vertical plane through the center of rows of dimer pairs for model (h). Charge density values go from 0.191 e/Å³ for Si-Si bonds to $2.7 \cdot 10^{-6}$ e/Å³ for the topmost line scan in the vacuum region. Experimental line scans are given above these for comparison. A schematic ball and stick model of the topmost 4 atomic layers is also shown. Si: light gray; C: dark gray.

Of all the models examined only in model (h) the surface Si dimers are displaced sufficiently towards each other to form effectively a pair of dimers as suggested by the paired bright spots in the STM images. In this structure, the surface Si dimers have been brought closer together by approximately 1.8 Å, in excellent agreement with the apparent distance of the bright spots in the experimental STM images. This displacement of the Si dimers is a consequence of the strain induced by the carbon atoms at sites B, D and E. Therefore it is proposed that the STM images could be interpreted as corresponding to this unusual structure, involving two Si dimers in the surface c(4×4) unit cell, brought considerably closer together due to the presence of a complex of six C atoms between the Si dimers, arranged in a surface carbon–carbon dimer and its first four subsurface neighbors.

Fig. 5-9 displays a contour plot of the charge density in a vertical plane through the center of the rows of paired Si dimers for model (h). A scheme of the atomic arrangement in this plane comprising the topmost four atomic layers is also depicted, which demonstrates the displacement of the Si dimers and the C complex with respect to bulk positions. With increasing distance from the surface dimers (i.e., decreasing charge density) the corrugation of the contours decreases and the only features that remain are the maxima directly above the two Si-surface dimers. The experimental line scans reproduce the calculated contours quite well, namely the maxima positions coincide exactly, supporting the validity of model (h). As the actual distance of the STM tip above the surface is not known and the convolution of the tip with the contours is not included in the calculations, the corrugations of the line scans can not be quantitatively compared. The decreasing corrugation with growing bias is due to increasing tip-sample distance.

A question to be taken into account is the entire amount of C atoms necessary for the

observed c(4×4) area. This covers about 10%–12% of the surface for 0.11 ML C, as far as can be deduced from a limited number of atomic scale STM images assuming homogenous deposition. If all C were contained in the c(4×4) regions, a number of eight C atoms would be available per c(4×4) unit cell. But it is very likely that a significant part of the deposited C atoms do not find enough neighbors to form a complex of six. These could then be incorporated in the areas between the c(4×4) regions, thus explaining the consistent buckling of the Si-dimers. Therefore, a model having six C atoms per c(4×4) unit cell is compatible with experiment.

As another measure of the validity of our model, the total energies of the different structures have been calculated and compared. Since these contain different amounts of C atoms, it is important to compare their energies as a function of the chemical potential of
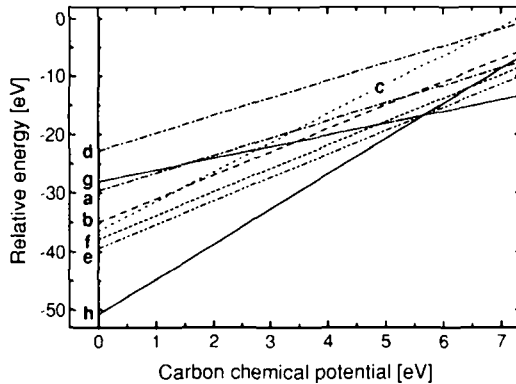
Fig. 5-10: Energy of the considered structures relative to a dimerized Si surface with one vacancy dimer per c(4×4) unit cell as a function of the carbon chemical potential. The lowest energy structure is by far model (h) in the range of chemical potentials relevant to experiment.

carbon. This comparison is shown in Fig. 5-10. The carbon chemical potential ranges from 0 to 7.4 eV. These limits correspond to the two extreme situations: in the first, the atomic reservoir for carbon atoms is a gas of free carbon atoms; in the second, the atomic reservoir is bulk diamond or graphite. The cohesive energy per atom of these two most stable forms of carbon is approximately the same, 7.4 eV. It is more realistic to use this experimental cohesive energy value here, since typically LDA underestimates atomic energies, leading to a theoretical cohesive energy value that would be 50% larger. For the energetic comparisons the atomic reservoir for Si atoms is taken to be bulk Si, with which the surface is always in equilibrium due to the presence of steps and other surface defects. For the systems, where carbon is deposited as monomers or larger clusters of carbon atoms (usually small, of size two or three), we believe the relevant range of carbon chemical potential is in the lower half of the

range shown in Fig. 5-10. In this range, the lowest energy structure is by far model (h), which also gives the images that correspond most closely to the STM images. At higher carbon chemical potential other structures become energetically competitive to structure (h), and eventually structure (g) becomes lower in energy.

Finally, in an attempt to determine the thermodynamic stability of the proposed structure, finite temperature simulations have been done using the semigrand canonical Monte Carlo method (SGMC) with the use of empirical potentials to describe the atomic interactions, which has already been applied with success to $Si_{1-x}C_x$ and $Si_{1-x-y}Ge_xC_y$ alloys. The empirical potentials used are derived from those proposed by Tersoff for SiC and SiGe. [34] A detailed description of this simulation method can be found in Ref. [62]. At a temperature of 600°C the structure is found to be very stable against interchanges of C and Si atoms. At somewhat higher temperatures (simulations were also performed at 900 and 1200°C), there is more of a tendency for interchange between the two types of atoms, although the rate of such atomic interchanges is rather small (approximately once in 10^5 MC moves). Considering a temperature uncertainty in the simulations of −100K and of −50K for experiment, all these temperatures are equal or higher than typical growth temperatures of around 550°C. This leads to the suggestion that, if the structure proposed here can be formed under usual growth conditions, then it will be stable.

Taking into account the experimental observations on the large scale morphology of the surface together with the proposed model structure (h), one can roughly understand the formation mechanism of the c(4×4) structure. In section 5.2 of this chapter one could see, that during deposition of carbon the c(4×4) areas arise at step edges or as islands on top of the Si(001) terraces. It would of course be very speculative to make any statements about the detailed kinetics of C on the surface, but nonetheless the observations lead to suggest the following: once a number of six (or less) C adatoms have approached, four of them penetrate into the topmost Si surface layer and expel the concerned Si atoms into adatom positions. These build up then the two Si ad-dimers of a c(4×4) unit cell, leaving a C ad-dimer in between. Thus a new atomic layer with c(4×4) reconstruction, identified as islands or as growth proceeding from the step edges, is generated. Step edges seem to act as preferential nucleation sites just like in any epitaxy. Probably the generation of c(4×4) islands on terraces is enhanced by initial defects on the (2×1) substrate. Once an embryo c(4×4) cell has formed on a terrace, it also enhances the nucleation of further cells. The generally anisotropic diffusion on the Si(2×1) and along its steps is qualitatively also valid for carbon adatoms, which is reflected in the elongated shape of the c(4×4) islands seen in Fig. 5-4 b).

It should be mentioned, that the substrate temperature plays an important role in the formation of the c(4×4) reconstruction. The deposition of C at 650°C for instance does not show any c(4×4) related streaks in the RHEED pattern. So it is likely, that at this temperature the carbon already diffuses into deeper layers. At temperatures around 600°C it has also been reported, that carbon is predominantly incorporated at interstitial sites. [52] Our models,

however, do not take interstitial carbon into consideration, which we believe is justified at the chosen growth temperature.

Resuming, the c(4×4) reconstruction with a complex of six C atoms is the stable surface structure as confirmed by the STM observations and our calculations. However, upon overgrowth of the surface with silicon or germanium this C_6 complex will dissolve almost certainly. In the bulk material, carbon tends to take energetically more favorable third-nearest neighbor positions, as predicted theoretically [41] and derived experimentally. [46]

5.5 Dependency on tip-sample bias voltage

Although the c(4×4) structure appears, as stated above, very similar for all sample bias voltages, there are small differences that are worth being considered. One might expect to see a splitting of each individual protrusion into two single maxima for empty state imaging, as this is seen for the Si dimers on Si(001) (2×1), reflecting the symmetry of the antibonding states of dangling bonds. But this is not the case. The only aspect in which filled and empty state images differ, is the apparent intra-pair distance between the two dimers in a surface unit cell. Generally a larger value is obtained for empty states than for filled states. This indicates that the maximum of the filled states is located more towards the carbon cluster, whereas the unoccupied states point further in the direction of the missing surface dimer. This seems to be reasonable, since at the missing dimer position the additional dangling bonds of the four second-layer atoms may contribute to the overall density of empty states. The same holds for the filled state density near the strong C–C bonds of the C_6 cluster. The C–C surface dimer bond may even have the form of a sp^2 hybridized double-bond, thus having no unoccupied states in form of dangling bonds.
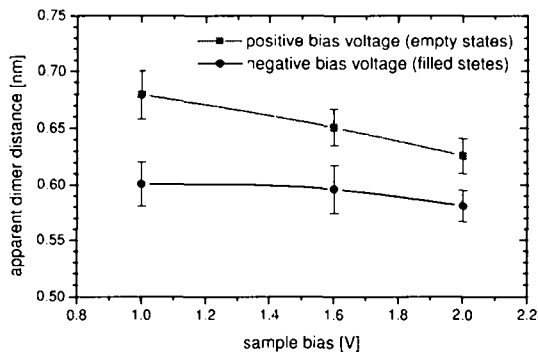
Fig. 5-11: Apparent intra-dimer distance as a function of sample bias voltage, derived from STM topographs. For empty states the distance is larger for all biases. Distance increases with decreasing absolute voltage for both polarities.
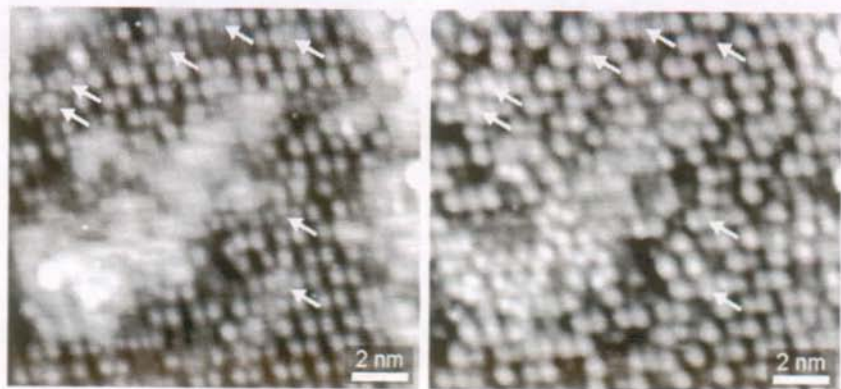
Fig. 5-12: Empty (left panel) and filled state pictures (right panel) of c(4×4) pattern (0.11 ML C) acquired simultaneously. Arrows mark the rhombus-like features discussed in the text.

We have evaluated the apparent intra-pair distances for tunneling voltages between 1V and 2V (−1V and −2V) for empty (filled) states, respectively, in Fig. 5-11. An increase of apparent distance with decreasing absolute voltage is observed, both for positive and negative bias. At the same time the depression between the dimers is more pronounced. It shows, that the peak position of the density of states depends on the corresponding energy of the states. The detailed reason for this is, however, not clear.

Another detail of our observations shall not be omitted: occasionally rhombus-like arrangements of spots are found in empty state images, as depicted in Fig. 5-12. These rhombi are also a c(4×4) structure and have previously been reported by other authors as the main feature in their empty state data. [15, 57] However, the structure is definitely different from that discussed in this chapter and is in our opinion not the essential and characteristic C-induced c(4×4) structure. Having a close look at the empty state pictures, one realizes, that the additional two small spots are positioned in the gap between two dimer pairs, thus forming a rhombus. In the corresponding filled state image a single wide bright blob, that protrudes slightly above the dimers, takes this place right in the middle between two dimer pairs. Hence, we believe that this must be due to an additional adsorbed adatom or ad-dimer. Indeed, the rhombus-like c(4×4) pattern is in qualitative agreement with the observation reported by Uhrberg et al. [15]. They had obtained this pattern by exposure of clean Si(001) (2×1) to hydrogen cracked at a hot tungsten filament. The structure was considered as a metastable pure Si reconstruction and explained by a mixed ad-dimer model. The presence of a certain amount of hydrogen in the residual gas in our experiment cannot be ruled out. The hydrogen may be cracked at the very hot carbon source filament, thus occasionally leading to this arrangement that is different from the carbon induced c(4×4). However, the Mixed ad-dimer model is not compatible with our model. So the atomic details of this secondary structure remain unclear.

6 Germanium quantum dots

6.1 Germanium on bare Si(001) (2×1)

The heteroepitaxial growth of Ge on the Si(001) surface has already been studied in detail by various techniques, such as x-ray diffraction, [63], [64] low energy electron diffraction (LEED), [65] reflection high-energy electron diffraction, transmission electron micros-copy,[66, 67] photoluminescence, [68, 69] scanning force microscopy [70] and of course by in situ scanning tunneling microscopy. [65, 71, 72] In this section the basic observations shall be briefly resumed.

The growth of Ge on Si is generally classified as being of the Stranski-Krastanov type. Due to its lower surface energy Ge tends to completely wet the Si substrate. So the first 2 – 3 monolayers grow in a layer by layer mode forming the two-dimensional (2D) wetting-layer, but then growth switches into three-dimensional (3D) island formation. The basic factor that governs this transition is the elastic energy that builds up in a coherent layer of Ge on Si due to the compressive strain in the Ge layer (4.2% lattice mismatch). At a Ge coverage of usually 3–4 ML, depending on actual growth conditions, the spontaneous formation of relatively small pyramidal islands with distinct {105} faceted sides, so called 'hut-clusters', is observed, having typical sizes of several ten nm. [73, 74] These are believed to be a metastable intermediate state [73] before a transition to larger 'dome' clusters that show a more complicated mixture of various facets [72], and finally to macroscopic clusters of undefined irregular shape. [73] The large clusters tend to further relieve the strain by the formation of misfit dislocations inside the cluster, which then penetrate into the underlying substrate. Hut clusters are usually still coherent with the substrate and relief the strain gradually towards their apex. [64] Even after formation of 3D islands a Ge wetting layer of 2–3 ML thickness remains between the islands.

Growth kinetics also plays an important role in the 3D transition. So the substrate tem-perature can be used to tune the morphology of the resulting islands. At lower growth tem-perature the size of the 3D islands is reduced and their density increased, which is a result of the limited diffusion rate of the adatoms. However, in this case of kinetic limitation the struc-ture is always more prone to formation of crystal imperfections and the homogeneity suffers in terms of size distribution.

2D wetting layer

The 2D wetting layer of Ge on Si(001) exhibits interesting features that are related to the misfit stress in these films. Already the first monolayer of Ge shows a quasi-periodic pattern of missing dimer defects, that is, every n^{th} dimer in the dimer rows is absent, thus leading to rows of missing dimers running perpendicular to the dimer rows. This structure can be described as a $(2 \times n)$ reconstruction, where n is on average equal to 12. [65] These missing dimer defects allow the rows of n dimers to relax already a part of the strain towards their ends. The second atomic Ge layer is affected by the $(2 \times n)$ pattern. There is a competition between the need to lower the surface energy by forming a closed layer and the partial strain relief by dimer defect superstructures. Second layer dimer rows preferentially grow on top of the underlying dimer
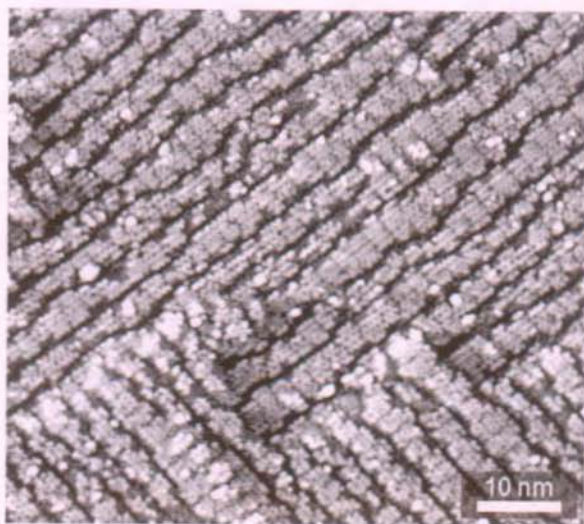
Fig. 6-1: High resolution STM picture of the residual 2D wetting layer of Ge on Si(001) (2×1) after formation of 3D clusters. The surface structure is dominated by trenches on average along ⟨110⟩ and missing dimer rows perpendicular to the trenches. The thickness of the Ge layer is 2-3 ML.

rows in the direction perpendicular to the latter. The positions of the missing dimers in the first layer are thus not all filled up. Instead, trenches of the width of at least one dimer row follow them. The periodicity of the trenches is determined to be $10 - 12$ a_0 on average. In addition, the second layer again contains missing dimer defects like the first layer at an angle of 90° to the trenches, but with a smaller periodicity of $m = 6 - 8$. So, effectively the second layer is made up of patches containing $n \times m$ lattice sites, separated by missing dimer structures. Obviously the strain relief by the missing dimers overrules the potential gain in surface energy by formation of a closed layer. Fractions of the third monolayer nucleate entirely on top of the patches. Hence, three atomic layers can be distinguished on each terrace, as seen in Fig. 6-1,

which shows the residual 2D wetting layer between 3D clusters after deposition of 5.8 ML Ge at 550°C. This argues, that the wetting layer retains a thickness between 2 and 3 monolayers.

a)

50 nm

b)

20 nm
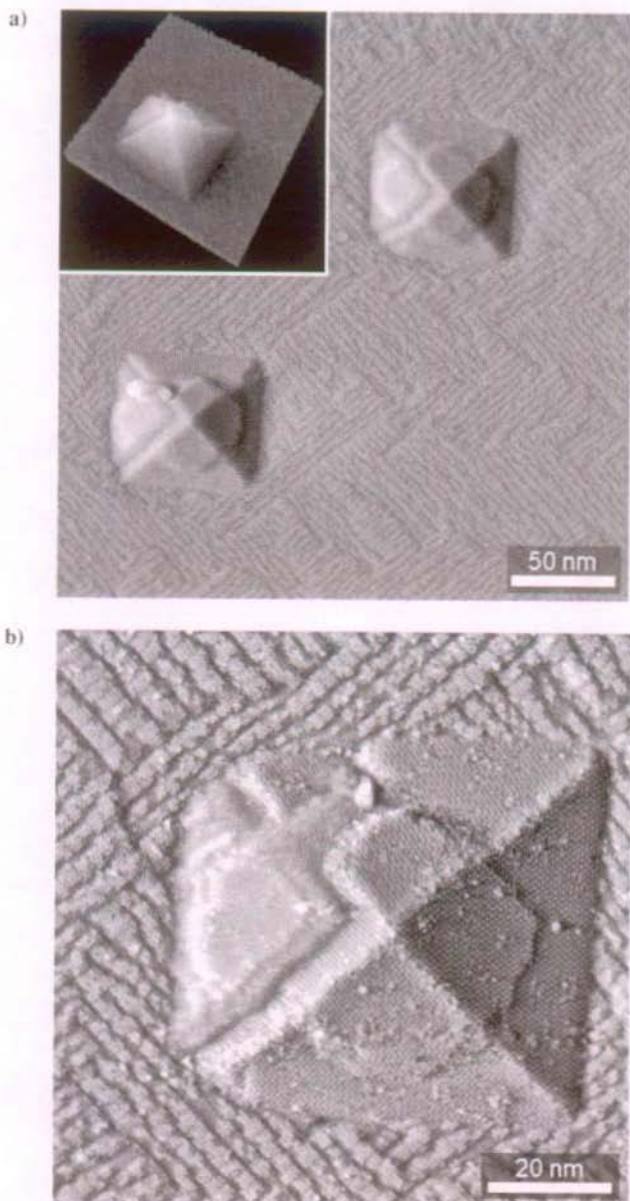
Fig. 6-2: a) Ge hut cluster grown on bare Si(001) (2×1) at 550°C. The low density (<2·10⁹ cm⁻²) and the large island size of 60 nm are due to the relatively high growth temperature. All observed islands have nearly identical size. Picture b) shows details of the characteristic reconstruction on the {105} facets. The blurred ghost image on the left side of the islands is due to a double-tip artifact. Note, that the growth of the island seems to proceed from the apex downwards.

3D islands

An example of the pure Ge hut clusters after deposition of nominally 5.8 ML Ge is given in Fig. 6-2 a). They have been grown at a substrate temperature of 550°C and a Ge growth rate of about 0.16 ML/s. Due to the quite high growth temperature the hut clusters are relatively large with a base length of about 60 nm. At the same time their density is low. It is rare to have two of them at once within the maximum scan range of 280 nm of the home-built electronics. So
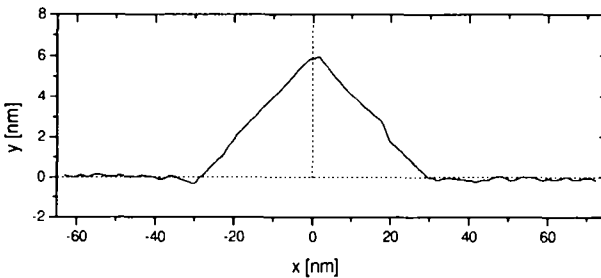
Fig. 6-3: Line scan across the center of a pyramidal hut cluster. The island is 60 nm wide and 6 nm high. The slope corresponds well to the {105} facet angle of 11.3°.

we estimate their density to be less than $2 \cdot 10^9$ cm⁻².

The walls of the pyramidal huts show the typical zigzag reconstruction of {105} facets, where each bright spot corresponds to a pair of two surface dimers. This is demonstrated in Fig. 6-2 b), where the contrast of a high resolution image has been significantly increased to reveal the atomic size details despite the large z-range covered by the whole hut. The {105} facets consist of monatomic steps parallel to ⟨100⟩, separated by a distance of 1.25 a_0. A line scan through the center of a hut cluster is depicted in Fig. 6-3, revealing the nearly perfect pyramidal shape of the cluster. The average slope is determined to be 11.8°±0.5°, which is very close or even identical to the angle of 11.3° that ideal {105} facets form with the (001) surface.

If a sufficient part of the surface is made up from facets, they can be in situ detected by RHEED, when the electron beam is incident in ⟨100⟩. The tilt angle of the facets tilts the 2D lattice rods of the reciprocal space by the same angle and can hence be directly observed on the RHEED screen as tilted streaks or V-shaped spots with an opening angle of twice the facet angle. In Fig. 6-4 a) an example of a RHEED pattern from {105} faceted dots is given, meas-
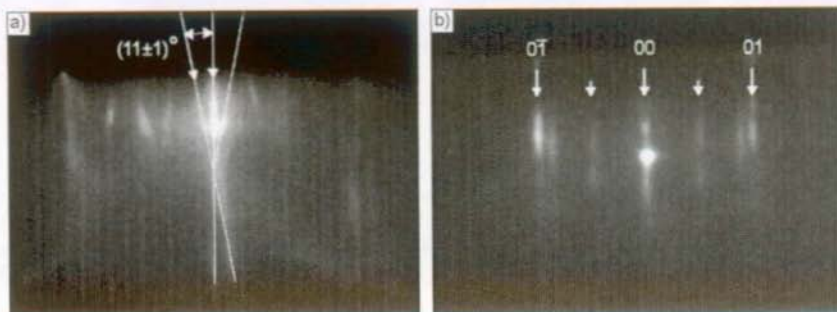
Fig. 6-4: RHEED pattern of Ge dot structure on Si(001). a) Electron beam incident in [100] yields streaks tilted at the facet angle of $(11\pm1)°$. b) In [110] the dimerized wetting layer dominates the pattern. Additional streaks inside the SBZ near the integer reflexes are probably due to the (2×8) missing dimer pattern of the wetting layer.

ured at a sample where 6 ML Ge have been deposited at a substrate temperature of 550°C and a rate of 0.14 ML/s. The tilted streaks are clearly identified. But the accuracy of the facet angle measurements is limited due to the short streaks and the streak width. The angle is determined as $(11\pm1)°$. In the (110) directions the huts are invisible to RHEED and the structure of the wetting layer determines the pattern, as seen in Fig. 6-4 b). Here basically the dimer structure gives rise to the integer and half order streaks. The additional streak near the (01) reflexes inside the surface Brillouin zone (SBZ), which has a distance of 1/8 SBZ from the latter, is very likely due to the missing dimer (2×8) superstructure

The hut clusters shown here are in fact slightly different from those reported by Mo et al. [73]. Besides the low cluster density, our clusters are rather quadratic in shape whereas in the literature usually clusters with a rectangular base and elongated apex are found, aligned to equal amounts in the two equivalent (100) directions. This anisotropy in cluster shape is caused by elastic interactions between adjacent huts. [75] Due to the large distance between the individual dots in our case, caused by high growth temperature, elastic interactions between the dots are negligible. Hence, they take the isotropic square shape, which is the optimal ground shape, where the energy per island volume is minimized. [76] Presumably these islands have already formed in a ripening process from smaller hut clusters, which would also explain the narrow size distribution.

Furthermore on our clusters depicted in Fig. 6-2 one can observe additional atomic layers (two or three) arising at the island apex and growing downwards, but stopping at about half way down. Similar effects have been observed for 3D islands of InP on GaInP/GaAs. [77] This is an interesting observation, which has to our knowledge not been reported so far. It can possibly be understood in the framework of shape transitions in strained island growth, which is generally unstable against this second order transition. [67, 76] When 3D islands coarsen, they go through a number of different shapes. For Ge the shapes range from {105}, {104}, {117} up to {113} faceted islands and mixtures of these, e.g. in the dome type clusters. Our

results are potentially an answer to the question, how the smaller pyramid-islands with {105} facets convert into the larger dome islands. The clusters here are presumably a frozen-in (due to growth interruption) transitional state from a {105} faceted dot to another steeper faceted dot, e.g. a {104} cluster [see [78]]. As already mentioned, the hut clusters are completely strained at the bottom, but relaxed at their apex. We think, that the observed feature is due to nucleation at the most strain-relaxed apex area, rather than growth from the island base upwards, in contrast to the discussion in [75]. The facets grow then downwards, but the new monolayers do not reach the bottom due to the increasing strain. The consequence is an increase of the facet angle and finally formation of new low-index facets. In order to make this process possible, the atoms deposited in the apex region are not sufficient. Adatoms that impinge into the region between the islands must be allowed to diffuse up the terraces, which may also be driven by the strain gradient. Note in this context the slight depletion of the wetting layer in the vicinity of the cluster.

Concluding, we assume, that the presented hut clusters here are in fact in a state of transition from the {105} hut cluster regime to another facet type regime. Nevertheless, they reveal the typical properties of Ge on Si(001), like the wetting layer and the {105} facets.

6.2 Ge deposition on C pre-covered Si(001)

As we have described in the previous section, the deposition of Ge on bare Si(001) surfaces leads to a strain induced spontaneous formation of hut clusters as soon as the Ge film exceeds a critical thickness of 3 – 4 ML. But since we are interested in structures with potential optoelectronic applications, it is desirable to reduce the dot size to a limit, where direct transitions become favorable due to a zero-dimensional confinement of carriers. Dot diameters can in principal be reduced by lowering the growth temperature. However, at low temperatures, where the smallest dots can be fabricated, [10] the material quality suffers and no significant dot-related luminescence is detected, due to non-radiating transitions at defects. Recently it has been shown that Ge islands with diameters as small as 10 nm can be produced on Si(001) surfaces pre-coated with a sub-monolayer of carbon at a growth temperature of 550°C. [11] These islands show rather intense photoluminescence (PL) [79, 80] and may have some potential in Si-based optoelectronics.

In this chapter we focus our attention on the formation of these C-induced Ge dots on Si(001) studied in situ by ultra-high-vacuum scanning tunneling microscopy (UHV-STM). [81] The results are supported by transmission electron microscopy (TEM) of C-induced Ge dots capped with Si and photoluminescence spectroscopy. [82]

Review of growth parameters

The samples were prepared in the MBE system using the standard procedure described in chapter 4 and 5, including a pure Si buffer layer and the sub-monolayer of C. Carbon deposition always took place at 550°C to ensure the formation of the c(4×4) reconstructed areas. STM samples with Ge coverage between 2.5 ML and 4 ML were all deposited at a substrate temperature of 550°C and a Ge growth rate of 0.16 ML/s. For TEM investigations 1–3 C-induced Ge dot layers separated by 150 nm wide Si barriers were grown. Dot layers grown directly on top of the Si buffer and on top of the layered structure show no difference in the STM analysis. For TEM samples the deposition temperature as well as the C precoverage were varied from 350°C to 750°C and 0.03 ML to 0.32 ML, respectively.

STM results

Fig. 6-5 compares the STM images obtained from (a) 2.5, (b) 4 and (c) 5.8 ML of Ge on a Si(001) surface pre-covered by 0.11 ML C. For Ge coverage up to 4 ML [Fig. 6-5(a) and (b)], basically a very rough three dimensional (3D) growth front is observed. It consists of bumps (islands) and voids with random shape, which are formed from stacks of single atom high Ge terraces, as can be seen in the inset of Fig. 6-5(b). No formation of distinct crystal facets is detected in this stage. Neither does the typical structure of a 2D Ge wetting layer appear. The growth front comprises already up to 7 atomic layers for 2.5 ML deposited Ge and up to 12 layers in the case of a 4 ML Ge deposit. In the following, we will call these irregularly shaped 3D islands GeC dots throughout this thesis, although this name is not undoubtedly related to the exact composition within the dots.

It is remarkable, that 3D Ge growth is already observed after the deposition of 2.5 ML of Ge on Si(001) surfaces covered with fractions of a ML of C. In contrast, Ge on bare Si(001)-(2×1) surfaces forms 3D islands (faceted hut clusters) only after the Ge thickness exceeds the critical thickness of 3–4 ML. [74] In this case, the driving force for the island formation is strain relief of the Ge layer by elastic relaxation of individual islands, in order to reduce elastic energy, which overrules the gain in surface energy. [83]

Since in the picture of a ternary $Si_{1-x-y}Ge_{1-x}C_y$ alloy the submonolayer C coverage should compensate a part of the overall amount of strain in the Ge layer (one C atom compensates the strain of 8-10 Ge atoms in a $Si_{1-x-y}Ge_{1-x}C_y$ alloy), this mechanism of strain relief appears not to be the dominating force for the early onset of 3D island formation here. However, the sub-monolayer C coverage, that is not uniformly distributed on the surface, (see chapter about C on Si(001) or Ref. [59]) may lead to an undulating surface strain field even before Ge deposition. The carbon containing areas having the c(4×4) pattern exert a compressive stress to the Si substrate underneath, and the areas in between are hence potentially strained tensilely. It is likely that the Ge island formation is driven by this strain field, that is, Ge nucleation is strongly favored to occur on the tensilely pre-strained pure Si regions, where the Ge lattice will be less compressively strained. The strong repulsive interaction between C and
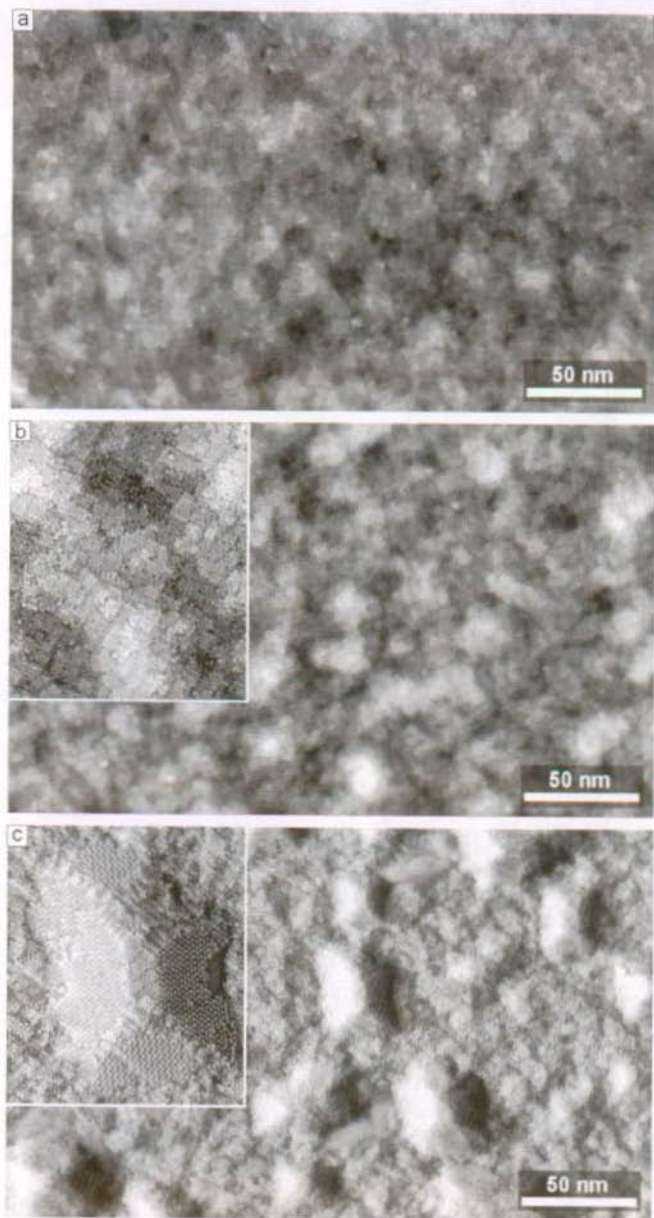
Fig. 6-5: Comparison of surface morphologies of different Ge-coverages on Si(001) precovered with 0.11 ML C. For (a) 2.5 ML and (b) 4 ML Ge coverage irregularly shaped islands with stepped terraces are obtained on C-precovered Si. Their height increases with the Ge coverage. At 5.8 ML Ge {105}-faceting of the Ge-island occurs at the expense of island density, as depicted in (c). The size and height (about 3 nm) of faceted island exceeds that of the stepped ones. [Picture (c) has been taken in derivative imaging mode]. Insets in (b) and (c), each (45×40) nm² in size, show atomic resolution details of the island morphology.

Ge [62] may also play a role, preventing the formation of Ge-C bonds. Hence, the Ge is to a certain degree prevented from completely wetting the substrate with completion of the first monolayer (this will be discussed in the following chapter). Furthermore, the surface roughness introduced by the C deposition [82] and, hence, reduced diffusion length for Ge-adatoms may contribute to the island formation in the low coverage range of 2–3 Ge ML.

It is not clear, to which extent the strain in this rough 3D layer is relieved. But the fact, that at 4 ML Ge no faceting occurs at the substrate temperature of 550°C, is a sign for a slight relaxation within the irregular Ge layer stacks, not urging the layer to take lower energy facets at this net thickness. This relaxation is likely to exceed the degree of relaxation that is possible in a 2D Ge layer with a trench structure. 2D Ge layers of 4 ML thickness without faceted island formation can only be obtained at lower growth temperatures.

Increasing the Ge coverage beyond a critical thickness leads to the spontaneous formation of faceted islands also on the C-covered Si surfaces [Fig. 6-5(c)]. Simultaneously the surface between the islands smoothens and the irregular islands obtained at lower Ge coverage die out. The dominating facets are {105} side facets and a flat (001) top facet. Quadratic as well as rectangular shapes are found, comparably to the typical hut clusters. Some clusters appear to be coalesced from islands created at neighboring nucleation centers. On the top (001) facet buckled Ge dimers with missing dimer rows are observed. Since these rows of missing dimers are an effective way for stress relaxation for the compressively strained Ge on Si, [65] as we discussed in section 6.1, this indicates that the islands are still partially strained at their flat apex.

The similarities with the well-known strain-driven Ge hut clusters observed on bare Si surfaces let us conclude that these islands are formed by a similar mechanism. The rough surface of the initial irregular 3D layer has per se a higher surface energy than a smooth 2D layer. For relaxation by faceted island formation, the reduction of elastic energy must exceed the cost in surface energy. This limit is obviously reached for 5.8 ML Ge, which is, however, at higher coverage than usual for Ge/Si without carbon. This could be interpreted as a surface phase transition, just like that between hut clusters and steeper faceted islands in the clean Ge/Si system. Once the energy barrier for this transition is overcome, the total energy, both surface and elastic strain energy, are minimized, leading to a decay of the irregular islands, i.e. smoothing of the layer and to the formation of the faceted more relaxed islands.

The density of the faceted islands on the C precovered surface is about $2 - 3 \cdot 10^{10}\,\mathrm{cm}^{-2}$ and thus is at least an order of magnitude higher than for the hut clusters found on bare Si(001) at the same growth conditions [$n \leq 2 \cdot 10^{9}\,\mathrm{cm}^{-2}$, see Fig. 6-2]. The increased surface roughness due to the irregular 3D islands and hence the large number of monatomic steps in all directions impedes the Ge surface diffusion during the transition to the faceted island shape. In addition, some of the irregular shaped islands may act as nucleation centers for the larger faceted dots. These two factors then lead to a higher nucleation density for faceted islands, which in turn
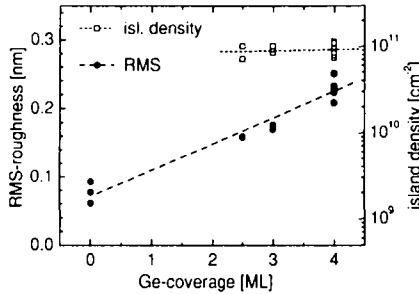
Fig. 6-6: Root-mean-square roughness (RMS) and island density as a function of Ge coverage as deduced from
STM images. The roughness increases monotonously while the island density remains constant.

results in a higher island density and smaller island size compared to islands grown on bare Si
surfaces at the same temperature.

The density of the faceted islands on C precovered surfaces is about a factor of 4 lower
compared to the irregular islands at lower Ge coverage. The density of the latter GeC islands
of 2.5 – 4 ML nominal Ge thickness is determined to be about 10^{11} cm^{-2}. As illustrated in Fig.
6-6 the island density appears not to depend on the actual Ge coverage, when counting all
islands higher than the mean height in the STM images plus the root-mean-square (RMS)
roughness. Fig. 6-6 also shows the dependence of RMS roughness obtained from the STM
scans as a function of the Ge coverage. The RMS-roughness increases monotonously with the
amount of Ge deposited from (0.08±0.02) nm, detected after the deposition of 0.1 ML C with-
out Ge, to (0.22 ± 0.03) nm after additional deposition of 4 ML Ge. Roughening of a surface
indicates that surface protrusions, i.e. islands, grow in height when their density is fixed.

Fig. 6-7 depicts the island height distribution of samples with Ge coverages of 3 ML (dark
gray) and 4 ML (light gray). Island heights are given in the number of ML with respect to the
level of the lowest voids in the images that are defined as zero. Only islands are counted that
lie above a certain threshold value (5 ML, in this case, see the horizontal line in the inset of
Fig. 6-7) by a gray-value discrimination and particle count algorithm. Counting below this
threshold is meaningless, since around the mean value of heights between bumps and voids in
the images one obtains only large areas formed by interconnected island bases from adjacent
bumps. The average height of the islands shifts from 5.7 ML to 7.6 ML for the samples with 3
and 4 ML deposited material, respectively. At the same time the height distribution becomes
broader with increasing thickness, again showing, that the growth front contains an increasing
number of atomic layers, in agreement with the increasing RMS value.
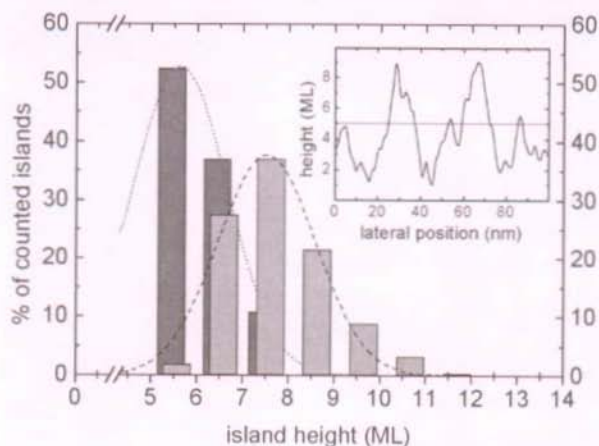
Fig. 6-7: Island height distribution for nominal Ge coverages of 3 ML (dark gray) and 4 ML (light gray). Mean island heights shift to higher values with increasing Ge coverage. Dashed and dotted curves are Gauss fits of the height distributions. The inset shows a typical line scan with the threshold for island count at 5 ML.

A quantitative analysis of an island diameter distribution on this randomly rugged surface does not seem to be useful, since the definition of the island bases and, hence, of the island diameters always remains somewhat arbitrary. Nevertheless, one can state that the size distribution is quite broad with the irregularly shaped bumps having diameters ranging from less than 10 nm up to 25 nm.

TEM investigations

The growth of the islands in the regime of 2.5 – 4 ML Ge can be clearly seen in TEM cross sections of capped C-induced dot layers. Fig. 6-8 a) shows a C-induced island layer (dark) of 2.5 ML Ge embedded in Si (light). The islands are quite shallow, with an approximate width of 10 – 20 nm and a height of 14 atomic layers. In the case of 4 ML Ge [Fig. 6-8 b)], the islands are more pronounced, in particular, the height has grown to about 18 atomic layers. Like the STM images of the surface dots, the TEM data of the corresponding islands embedded in Si show no well-defined facets. An overall change of island shape due to capping with Si, that has been demonstrated for initially {105}-faceted dots, [84] cannot be detected for the initially non-faceted islands. Still, the islands are undoubtedly affected by the overgrowth with Si; the slightly larger island height observed by TEM compared to the STM data might be attributed to the segregation of Ge during capping. One should keep in mind, that capping is always necessary when studying optical properties of dot layers, in order to prevent non-radiative recombination at surface states of the nanostructures.

In the TEM images the islands seem to be connected by a narrow dark line. However, this dark line is not very homogeneous and hence is not necessarily a hint for a Ge wetting layer. It can either be just the projection of the irregular depressions in the dot layer across the TEM foil, or it can be the Si–C alloy or both. A detailed study of the Ge nucleation in the sub-monolayer regime on the C precovered Si(001) surface, that will be presented in the next chapter, shows, that at low Ge coverage there is indeed no continuous Ge layer. The TEM shows no extended defects like dislocations in the grown layer although the crystal contains carbon in the area of the dot layer. It is worth mentioning that we have observed intense pho-
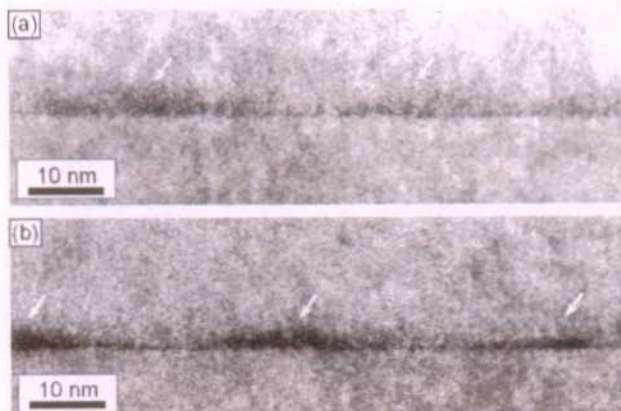

Fig. 6-8: TEM cross-sectional images of overgrown samples with a) 2.5 and b) 4 ML Ge coverage. Islands are indicated by arrows. They become higher and more pronounced with increasing Ge coverage.

toluminescence for the capped C-induced dot layers [82], as will be shown below, in agreement with Ref. [11].

For further information on the growth mechanisms of this new type of C-induced Ge dots the effect of the deposition temperature on the dot formation was investigated by TEM. Fig. 6-9 depicts four cross-sectional TEM images taken from samples with 0.11 ML C and 2.5 ML Ge grown at a) 350°C, b) 550°C, c) 650°C and d) 750°C. We kept the Ge thickness at this value, because 2.5 ML is well below the critical thickness of island formation without carbon. In Fig. 6-9 pronounced Ge dots are found at a temperature of 550°C. Samples of 450°C (not shown) have very similar dot structure. At 350°C only a defective 2-dimensional quantum well layer is observed (dark line in Fig. 6-9 a) and no dots are formed. Most likely this is due to the limited surface mobility of the C and Ge atoms at this low temperature. At 650°C on the other hand, a rather smooth well is observed. In this case the pre-deposited C smears out into the surrounding material and dots do not form. This can be understood, because at 650°C no carbon c(4×4) pattern is formed and thus the prerequisite for the island formation at the low coverage of 2.5 ML is not met. At 750°C dark spots appear (Fig. 6-9 d) that are most probably SiC precipitates. The 2.5 ML Ge have segregated into the surrounding Si and are not seen in the TEM cross section.

The next important question is how the GeC dot formation is affected by different amounts of pre-deposited carbon. So we prepared

Fig. 6-9: TEM cross section of dot structures (0.11 ML C, 2.5 ML Ge) grown at different temperatures: a) 350°C, b) 550°C, c) 650°C and d) 750°C. Pronounced dot formation is only found for temperatures around 550°C (b) down to 450°C.

samples containing 0.03, 0.11, 0.2 and 0.32 ML carbon by C deposition for 120s, 480s, 960s and 1500s respectively, again followed by 2.5 ML Ge. The substrate temperature was held at 550°C. The typical effect of a carbon flux decay within the first 100 seconds after opening the shutter due to the change of thermal equilibrium of the source was taken into account when estimating the lowest coverage. Cross sectional TEM images of the corresponding layers are depicted in Fig. 6-10. At the lowest C coverage of 0.03 ML no distinct GeC dots are observed. This is consistent with our STM results, where at 0.05 ML C no well developed C rich areas are detected. The small amount of carbon is spread nearly homogeneously on the substrate, thus not driving the 2.5 ML Ge into the 3D growth regime. This changes at 0.11 ML C coverage as discussed above. The most pronounced dot formation is obtained at a predeposition of 0.2 ML C. In this case STM reveals, that around 30% of the surface is covered with the carbon-rich c(4×4) reconstruction. So three-dimensional Ge growth is even enforced compared to the 0.11 ML C coverage. The dark line interconnecting the dots appears particularly thin in this case.

At even higher carbon coverage of 0.32 ML the TEM still shows a contrast that may be attributed to Ge islands, but the overall image appears somewhat distorted. Dark spots are
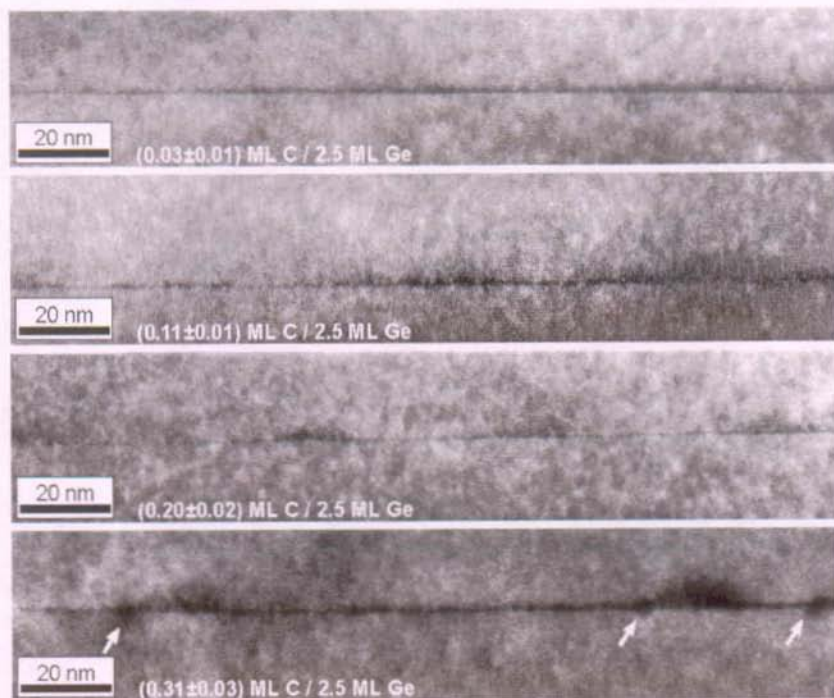
Fig. 6-10: TEM cross-sections of GeC dot layers containing different amounts of predeposited C and 2.5 ML Ge each, grown at 550°C. The C content is indicated in each image. The dark spots (see arrows) penetrating into the substrate are probably SiC, formed due to the high C coverage.

visible that penetrate into the substrate, indicated by the arrows. They show a Moiré pattern in high resolution TEM micrographs. Butz et al. recognized the formation of 3D islands about 4 nm in diameter and 1.5 nm height upon deposition of 0.5 ML C at 600°C. [57] These islands were interpreted as SiC precipitates forming on the surface far before the whole surface is covered with c(4×4). The value of 0.5 ML is certainly an upper limit, where the SiC islands have been recognized. It is possible that they start growing already at slightly lower coverage, that have not been investigated by STM. So it is very likely, that they are the cause for the observed features in the TEM image for 0.32 ML C.

Concluding this section, TEM shows that the optimum regime for coherent 3D GeC dot formation on Si((001) is a growth temperature between 450°C and 550°C and a C predeposition of 0.1 to 0.2 ML. For this regime, GeC dots are readily obtained for Ge coverages of 2.5 ML and above.

6.3 Photoluminescence from C-induced Ge dots

In the previous section we have described the morphology of pure and C-induced Ge dots, both studied by STM and TEM. In this paragraph we will show, that optical properties of these structures, which were studied by photoluminescence (PL) measurements, are strongly correlated with the morphology. As mentioned above, it is always necessary to cap the nanostructures (dots) on the surface by Si, since otherwise the PL emission of the dot layer is prevented by non-radiative recombination paths via surface states.

Before showing PL measurements of C-induced dots the PL spectra of pure Ge dots on Si((001) without carbon predeposition will be discussed first.

Fig. 6-11 represents a spectrum of a sandwich structure containing 10 periods of 7 ML (1 nm) Ge separated by 15 nm Si grown at 750°C. This sample exhibits large coherent Ge dots around 200 nm in diameter in each layer, which have a relatively narrow size distribution due to vertical alignment. The PL spectrum of this structure is comparable to that of a single dot layer or a vertically non-aligned multiple dot layer, with the only difference, that the intensity of the PL signals related to the Ge-structure is larger with respect to the bulk Si signals. The Si related peaks are situated at the high energy side of the spectrum. The very low no-phonon peak (NP) at 1.15 eV belongs to the direct bound exciton transition in Si, which has a low transition probability in the indirect band gap material. Excitons are usually bound to shallow impurity levels that typically lie about 5 meV below the band gap. Clearly, in the indirect bulk Si the symmetry-allowed phonon assisted transitions show much stronger intensity. The transverse optical (TO) phonon replica of this bound exciton transition is the strongest in Si and is found at a distance of 58 meV (the Si-Si TO phonon energy) below the Si NP line, namely at 1.092 eV. Due to the high excitation density used it is buried behind the wide intense peak around 1.083 eV. This peak does not depend on the particular structure of the
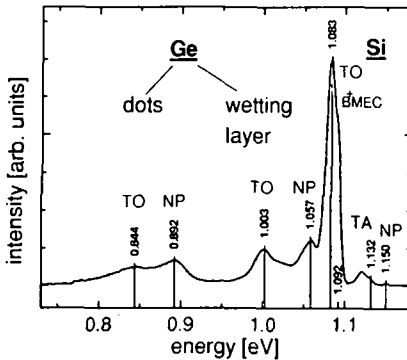
Fig. 6-11: PL spectrum at 4K of a multilayer of 10 periods 7 ML(1 nm) Ge / 85 nm Si spacer grown at 750°C. The layers contain Stranski-Krastanov Ge dots of around 200 nm diameter. Both dot-related and wetting layer PL lines are obtained. Bulk Si lines are broadened due to the formation of bound multiexciton complexes (BMEC) caused by high excitation density of 100 mW at an excitation wavelength of 488 nm.

sample, but stems from an effect related to high excitation densities. It is assigned to the formation of bound multiexciton complexes (BMEC) at increased exciton densities, whose decay gives rise to this broad luminescence at the low energy side of the corresponding excitonic recombination. [85] For the Si NP line this peak cannot be detected in the spectrum of Fig. 6-11 due to the very low peak intensity there. But it is clear, that the BMEC recombination is equally mimicked by the phonon assisted transitions, and hence also overlays the Si TO phonon line at a distance of 9 meV. It can also be seen at the same distance from the Si TA phonon line at 1.132 eV. At lower laser excitation density these BMEC lines decay and allow the observation of the distinct Si TA and Si TO peaks.

At lower energies one observes two further pairs of peaks. These are related to the actual structure of the Ge layers. The peaks at 1.057 eV and 1.003 eV are assigned to the NP and TO assisted lines of the Ge wetting layer (WL), respectively, that is always remaining in the regions between Ge dots in the pure Ge/Si system. Their energetic distance of 54 meV is by 5 meV larger than the Si-Ge TO phonon energy of 49 meV in unstrained bulk SiGe [86]. But the 2-3 ML thin Ge wetting layer is buried in Si and thus contains severe compressive strain, which increases the energy of the lattice vibrations. Furthermore, due to Ge segregation during overgrowth, whose decay length attains about 1 nm at 750°C, [87, 88] the WL is rather a SiGe alloy with a gradual change in composition at the top Ge-Si interface and a sharper Si-Ge interface at the bottom. Thus it is difficult to obtain exact values for the transition energy from theory. However, the band gap of the Ge QW strongly increases with decreasing well width due to the confinement effect. The NP value of 1.057 eV for this quantum well and the detection of the Si-Ge TO phonon replica are thus reasonable. In addition, the WL TO line shows a shoulder at the high energy side that surely stems from the weaker Ge-Ge TO assisted transition.

The second pair of peaks at energies of 0.892 eV and 0.844 eV are then interpreted as the NP and TO lines of the Ge quantum dots, respectively. Due to their large size of about 200 nm the lateral confinement effect is not pronounced, so that they can be considered as quantum wells of larger thickness than the wetting layer (but varying towards the edges). In addition, the strain in the dots is not homogeneous and segregation is also present, making a theoretical

prediction of the energy levels even more difficult. Anyway, it is clear, that the transition energies lie substantially lower with respect to the WL due to increased thickness and higher average Ge content. The peak distance of 48 meV corresponds closely to the Si-Ge phonon energy. The broad line width is explained in terms of the dot size distribution.

When the pure Ge dots are grown under different growth conditions leading to smaller dot size, the dot related peaks shift to higher energy due to enhanced confinement effects, whereas the wetting layer PL remains at essentially the same energetic position, because the wetting layer is always present in this system.

With these characteristics of the PL of pure Ge dots in mind, the photoluminescence spectra of the carbon-induced Ge islands shall be discussed next. Spectra of sample series deposited under different growth conditions and containing different amounts of Ge are shown and compared to the structural information obtained from TEM.

Fig. 6-12: Measured 4 K photoluminescence spectrum (top) of a GeC dot layer (0.11 ML C, 2.5 ML Ge grown at 450°C) and a simulated Gauss peak fit (bottom). The broad doublet peaks are associated with the NP and TO emission from the GeC dots. Excitation power was 11 mW unfocussed at 488 nm.

Fig. 6-12 shows a spectrum of a typical carbon induced Ge dot layer consisting of 2.5 ML Ge on 0.11 ML C grown at 450°C. It has been taken "as grown", i.e. without the need for annealing the structure. Excitation density is chosen so that no BMEC recombination is detected. The spectrum is dominated by a broad peak with a linewidth of 25 meV at around 1.078 eV. At a distance of 46 meV on the low energy side a flatter but even broader second peak at 1.032 eV is found. These two peaks are assigned to the NP transition related to the C-induced Ge dots and its TO phonon replica. Note, that this dot related PL has high intensity compared to the bulk Si TO line, which is usually a prominent feature in the PL of SiGe heterostructures, but which is hidden by the dot NP peak here. The linewidth of the peaks is attributed to the broad size distribution of the GeC quantum structures, especially for low growth temperatures.

The TEM results have shown that effective GeC dot formation is only obtained at growth temperatures between 450°C and 550°C for 2.5 ML Ge coverage and a C-predeposition of minimally 0.1 ML. The PL spectra verify this experimental result. In Fig. 6-13 the influence of the growth temperature on the 4K PL spectra is demonstrated. The samples contain 0.11 ML C and 2.5 ML Ge. For the growth temperature of 650°C and 750°C only the TO-phonon line of

Si at 1.09 eV is visible. Besides this line, typical defect related broad band luminescence around 850 meV is observed for the sample grown at 350°C. The photoluminescence features related to the deposition of the C-induced Ge quantum structures are only observed at growth temperatures of 450°C and 550°C. At 550°C the NP-TO doublet with one peak at 1.086 eV and the second peak at 1.035 eV are resolved. At 450°C the spectrum is broadened compared to the latter PL spectrum. The explanation behind this can be the improved dot size homogeneity at 550°C. In addition, a slight shift of peak positions to higher energy with increasing growth temperature is recognized (~ 8 meV for the NP line).

The dependence of the photoluminescence spectra on the amount of Ge is illustrated in Fig. 6-14. Here, the amount of C is kept constant at 0.11 ML whereas the Ge coverage is varied from 2.5 to 4 ML (substrate temperature 550°C). From TEM and STM data it is known, that Ge islands do exist in these samples that increase in size with growing Ge coverage. The no phonon PL peak shifts from 1088 meV at 2.5 ML to 1060 meV at 3 ML and to a broad peak centered around 940 meV at 4 ML. The broadening of the PL spectra with increasing amounts of Ge deposited indicate that the size distribution of the islands contributing to the emission broadens.

Although the two prominent broad PL peaks have been a priori related to the GeC dots above, mainly because they arise from the samples where their existence has been definitely verified, this assignment could be ambiguous, since the PL peaks from a 2D wetting layer in a pure Ge system are lying at similar energetic positions (see e.g. Fig. 6-11). Therefore, this assignment is discussed in more detail. The term wetting layer is referred to the portion of the structure having two-dimensional quantum well character.

A strong indication for PL of islands is the large energy shift of 140 meV upon the Ge thickness change of only 1.5 ML from 2.5 to 4 ML (Fig. 6-14). For a 2-dimensional quantum well this would only lead to a smaller energy shift of 66 meV/ML according to ref. [79] for a pure Ge wetting layer. The red shift of sub-band states in case of zero-dimensional confinement with growing quantum dot size is much stronger than in case of one-dimensional confinement (QW).

If a "wetting layer" were present simultaneously with GeC dots, it would definitely contain C in the range of several percent. Both species, Ge and C, are then probably inter-diffused with the surrounding Si. A prediction of the peak positions in this alloyed system can therefore not be made. For a two-dimensional system like the wetting layer, a well resolved spectrum with rather narrow lines is expected. Moreover, typically the TO-phonon line has an intensity comparable to or larger than the NP line for quantum wells in the Si-Ge-C material system. [89] In the obtained PL spectra the rather well resolved separation of the TO-phonon and NP line would suggest a 2-dimensional confinement, whereas the weak intensity of the TO-phonon line suggests luminescence of low dimensional structures in Si. [90]
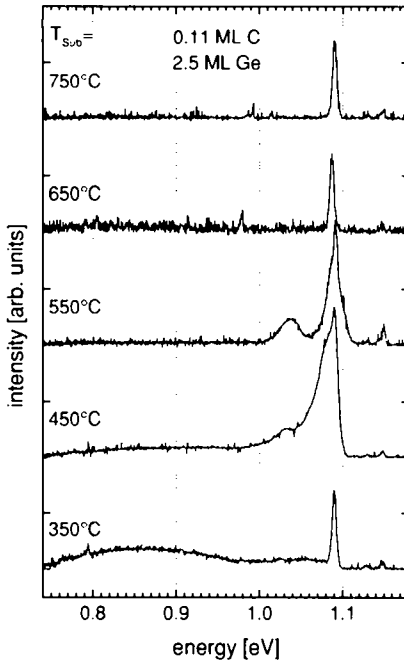
Fig. 6-13: 4 K PL from GeC dots grown at different growth temperatures. All samples have 0.11 ML C and 2.5 ML Ge. Dot-related PL is only found for T_{Sub}=450°C and 550°C.
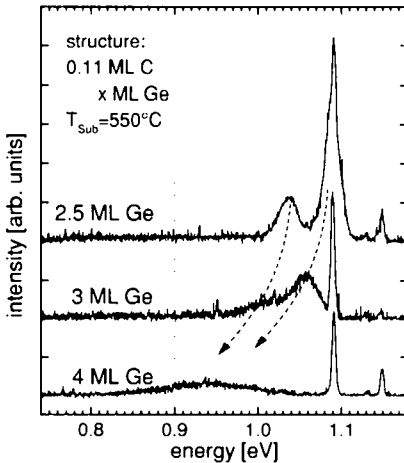

Fig. 6-14: PL spectra (4 K) at different Ge coverage. A pronounced red shift and intensity decrease is observed for increasing coverage.

At this point we like to stress that the amount of C used here to induce Ge island formation is really small (0.1 ML). For higher C coverages, e.g. 0.2 ML, the formation of the C-induced Ge dots has been reported for even thinner Ge films, i.e. 1.6 ML. [11] It leads to intense by PL lines assigned to dots at a Ge coverage of 2.16 ML.

Most likely the observed PL originates from the islands that consist of stacks of 5 - 7 ML of Ge. The system can also be considered as a very rough 2D-layer with large thickness fluctuations. Due to the high density of $1 \cdot 10^{11}$ cm^{-2} of the islands or dots, i.e. areas of wide "well width", it is expected that the excited carriers are collected very efficiently in these areas with the lowest states in energy.

The energy at 1.08 eV is rather high for luminescence from Ge islands. However one has to consider that the strain of Ge towards Si is partly compensated by the C, which leads to an increase of the band gap of these islands compared to islands formed in the Si-Ge system. In addition, the TEM images reveal a very narrow wetting layer of only 1 - 2 ML between the dots. This SiGeC wetting layer is expected to give PL at even higher energies.

There are even more indications for the dot-like character of the PL spectra. For instance, the dot PL changes and blue shifts gradually to a definite SiGeC quantum well luminescence upon annealing samples up to 950°C, as depicted in Fig. 6-15. This is due to
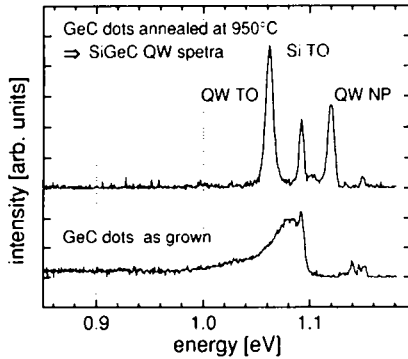
Fig. 6-15: PL spectra (4 K) of the same sample (GeC dots 0.11 ML C, 2.5 ML Ge grown at 450°C) before and after annealing to 950°C. The dot-related PL of the lower spectrum changes to a SiGeC quantum well spectrum with distinct narrow NP and TO peaks. Excitation power is 0.6mW.

interdiffusion of the different species causing the dots to smear out into a QW shape. Details on these investigations are given in the references [91] and [92].

Furthermore, the excitation dependence of the PL spectra indicates 3D confinement showing saturation effects of the dots. The relation between the excitation power P and the integrated intensity of the PL signals I_{PL} is plotted in Fig. 6-16 for the same sample as in the figure above, both before and after annealing at 950°C. In general, this relation can be described by a power law $I_{PL} \propto P^m$. [93] The slope m of the double-logarithmic plot (Fig. 6-16) permits insights into the dominant recombination mechanisms in the samples. The rate of electron-hole pair generation, excited by the absorption of the incoming photons and resulting in the carrier density n, is proportional to the excitation power P. The emitted PL intensity is always the result of the competition between the radiative and non-radiative recombination rates R_{rad} and $R_{non-rad}$, respectively. That means, the PL intensity I_{PL} is proportional to the ratio $R_{rad} / (R_{rad} + R_{non-rad})$ or, equivalently, to the ratio of the lifetimes $\tau_{non-rad} / (\tau_{rad} + \tau_{non-rad})$. [94] The radiative recombination rate is governed by its time constant τ_{rad} and is proportional to n^2. For the non-radiating recombination there are basically two possible pathways: the recombination via scattering processes generating phonons or the recombination via an Auger process. In the Auger process, an electron-hole pair recombines by donating its energy and momentum to a free electron (hole) in the conduction (valence) band that is excited to higher states, from which it decays via phonon processes. As for this process an additional free carrier must be present, the Auger recombination rate increases with n^3. Its time constant is short (~1 ns) compared to the radiative lifetimes in SiGe (~1 ms). The rate of non-radiative recombination via impurity levels is on the other hand directly proportional to the carrier density n. If, for instance, Auger recombination is the predominant recombination path, the PL intensity will increase sublinearly as $I_{PL} \propto P^{2/3}$. [95] So for dominant Auger recombination the slope m equals 2/3, $m = 0.66$. In contrast to this, for predominant impurity recombination the intensity scales like $I_{PL} \propto P^2$ and the slope is $m = 2$. [94, 95]

Looking at Fig. 6-16 it is evident, that in the case of the as grown GeC dots Auger recombination is indeed the most probable path, as the slope is equal to 0.66 over the whole range of excitation power. A similar behavior has been reported for SiGe dots around 100 nm in diameter. [95] For the annealed sample, the SiGeC quantum well contribution to the PL inten-
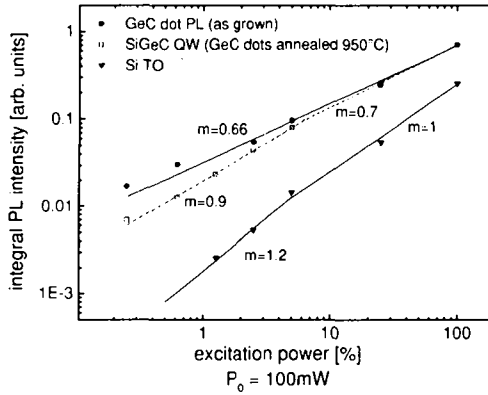
Fig. 6-16: Excitation power dependence of the integrated PL intensity for the GeC dot sample containing 0.11 ML C / 2.5 ML Ge grown at 450°C. Plots are given for the dot-related PL from the as grown sample containing GeC dots, and for the SiGeC QW PL and the Si TO intensity after annealing to 950°C. The corresponding spectra are displayed in Fig. 6-15.

sity shows a slope ranging from $m = 0.9$ at low excitation power to $m = 0.7$ at higher excitation power. This corresponds to a transition from a more excitonic recombination to the Auger dominated value. The integrated intensity of the bulk Si TO peak, in contrast, has a slope of $m = 1$ at high power, indicating the dominance of excitonic recombination. At lower excitation power the slightly superlinear slope may indicate the influence of impurity related recombination.

The observation of dominant Auger-recombination in the GeC quantum dot sample already at low excitation power supports, that the sample really exhibits a three-dimensional carrier confinement and that the observed luminescence stems from quantum dots. Most carriers excited anywhere in the sample migrate within their lifetime rapidly to the confinement potentials of the quantum dots. The 3D-confinement leads to locally high carrier densities in the dots even at low excitation power, thus strongly enhancing the probability for the Auger process here. For the quantum well structure of the annealed sample the carrier localization and thus the Auger recombination is not so important at low excitation power, leading to the steeper slope $m = 0.9$.

For a deeper understanding of the PL mechanisms it might be important to know, whether the Ge islands grow on top of the C patches or in between them. In the first case, the enhancement of PL intensity in comparison to 2-dimensional SiGe quantum well structures can be explained by a spatially indirect type II recombination within the C induced Ge islands. In the picture of Ref. [80] the GeC dots are described as having a gradual composition profile from SiCGe at the bottom to pure Ge towards the apex. This would also lead to a gradual transition of the band alignment within each dot from a type I confinement of electrons in the conduction band in the C-rich lower SiCGe region towards a confinement of heavy holes in the

valence band at the Ge rich dot apex. Hence the optical transition involves a type II recombination of the electron hole pairs confined in different regions of the dots. This is possible, since Bohr radii of bound excitons in SiGe can be as large as 11 nm, [85] and, thus, are typically larger than the height of ≤ 3 nm of these small islands. A schematic drawing of the dot composition and the bands assumed in this model is given in Fig. 6-17 a).

In the second case enhanced confinement effects may be the origin for the intense PL. The idealized picture of a Ge-free $Si_{1-x}C_x$ area in between C-free 3D SiGe islands would potentially lead to a strong confinement of electrons in the SiC, whereas holes would be exclusively trapped in the islands. This is illustrated in Fig. 6-17 b). Then, following the same argumentation as in the first case, the spatially indirect recombination of the carriers from the island position to the SiC regions is possible when their distance is smaller than the exciton binding radius. Understandably, this is strongly favored, when the islands are small and dense.

For the latter model it is also important, that the Ge or SiGe thickness shown schematically above the SiC remains thin. If this thickness grows, the well defined confinement smears out thus decreasing the direct recombination probability. As seen in Fig. 6-14 a rapid decay of PL efficiency with Ge coverage is observed, possibly because of the latter reason.

At this stage one cannot decide whether the islands form on top of the C rich areas or in areas in between them. On the one hand Ge-C bonds are even less favorable than Si-C bonds which may lead to an accumulation of Ge in areas with no or low C concentrations. On the other hand SiC alloys have a smaller and SiGe alloys a larger lattice constant than Si, therefore the accumulation of Ge on top of the C rich areas would lead to a strain compensation, which
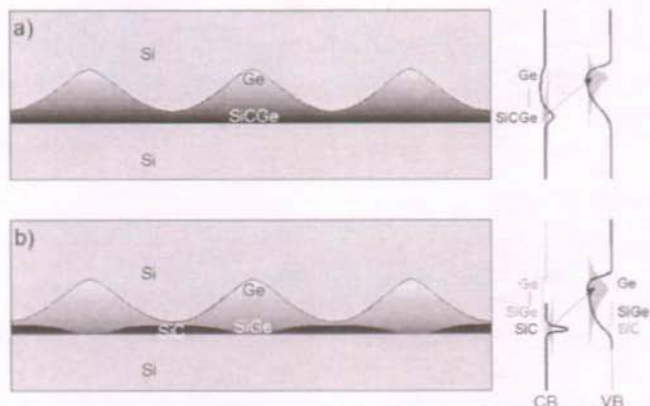

Fig. 6-17: Idealized schematic representations of possible GeC dot composition and resulting schematic band alignments. In a) GeC dots are assumed to grow on the carbon covered areas leading to dots of gradual composition change from SiCGe to Ge at the apex. PL could be explained by a spatially indirect recombination of electrons confined at the bottom and holes confined near the dot apex. In b) Ge is assumed to grow preferentially between the C rich areas. This leads to a confinement of e^- in the SiC regions and of holes in the SiGe...Ge islands. The effective confining potentials are sketched in black, but they are located at different positions in the layer plane. Nevertheless, spatially indirect recombination is possible, if the lateral distances involved are smaller than the exciton Bohr radius.

might be favorable. But the findings from the following chapter, where the Ge nucleation on C precovered surfaces in the submonolayer regime is investigated, strongly support the second model [Fig. 6-17 b)], since the Ge atoms avoid the c(4x4) domains and form 3D islands in the regions between the domains, not wetting the complete substrate.

The fact of dominating Auger recombination in these quantum structures raises some questions. On one hand it shows, that the samples are of good crystallographic quality, i.e. it is not impurities or defects that limit the PL output. However, a quality problem could potentially be circumvented by proper growth techniques and optimization. On the other hand one has to state, that, if the severe Auger recombination is an intrinsic property of this kind of carbon containing nanostructures on Si, it will be difficult to get around it and further increase the luminescence efficiency. Possibly even higher dot densities at smaller dot sizes could reduce the Auger process and further enhance radiative transitions, as every single dot would be less populated at a given excitation density.

7 Sub-monolayer Ge nucleation on C/Si(001)

In chapter 6 we have seen, that germanium forms irregularly shaped 3D islands on a C precovered Si(001) surface. The investigations were governed by the wish to reveal the detailed structure of these GeC dots, that exhibit strong dot-related photoluminescence. However, from these relatively thick Ge layers, where at a coverage of 2.5 ML islands are readily developed, no definitive conclusions can be drawn about the actual nucleation process. One could only state, that island formation starts at lower coverage than on bare Si(001) and that the island shape differs from the anticipated hut cluster shape. At which coverage the nucleation of the GeC islands exactly starts remained rather speculative at that stage.

To get deeper insight into this process, the initial stages of GeC dot nucleation will be evaluated in this chapter.

7.1 Sample preparation

The growth parameters closely resemble those described in detail in chapter 6. Only the differences imposed by the low Ge coverage are given below. The substrates used were p-type Boron-doped Si(001) wafers with nominally no miscut and a resistivity of (30–50) Ωcm, corresponding to a doping level of $4.6 \cdot 10^{14}$cm^{-3} down to $2.8 \cdot 10^{14}$cm^{-3} (Wacker W54).

For the STM study of sub-monolayer Ge deposition we tested the impact of growth temperature on nucleation by choice of substrate temperatures of $T_{sub} = 350°C$ and $550°C$. The C precoverage of 0.11 ML using the standard source current of 100 A was produced at $T_{sub} = 550°C$ to make sure the formation of the c(4×4) reconstructed patches. We deposited Ge with a coverage between of 0.1 ML and 1 ML. In order to be able to accurately control the low coverages, the Ge growth rate was reduced by a factor of 15 to an intended 0.011 ML/s by linear reduction of the flux regulation parameters for the mass spectrometer. Subsequently the rate has been calibrated by SIMS, yielding the actual rate of (0.013 ± 0.001) ML/s. The obtained Ge-coverage for different deposition times according to the SIMS measurement are given in Fig. 7-1. The deposition rate is reproducible within an error of less than 10%.
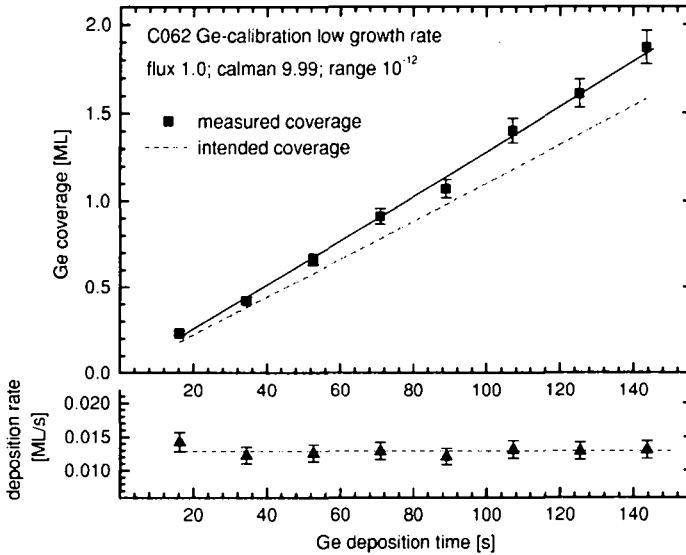
Fig. 7-1: Ge coverage and deposition rate as a function of deposition time. Values are extracted from SIMS calibration of a calibration sample containing 8 layers with different amounts of Ge separated by 120 nm wide Si spacers, all grown at a substrate temperature of 550°C. Ge source flux control parameters are given in the plot.

7.2 Ge deposition at T_{sub} = 350°C

When growing Ge at substrate temperatures above 500°C on bare Si(001), intermixing of Ge adatoms with the Si substrate within the first monolayer is observed. [96] So the identification of single Ge atoms with STM is obstructed, as it has to date not been possible to distinguish (even with spectroscopic STM techniques) between alloyed Si and Ge atoms at the surface. A distinction between the species is only possible, when Ge forms a different surface reconstruction than the initial Si substrate. [97] On Si(001), however, Si and Ge have the same (2×1) symmetry.

To avoid intermixing, the deposition temperature is chosen well below 550°C, so that deposited Ge stays preferentially at the surface or is incorporated at defects such as step edges. Suitable temperatures, where the growth is mainly kinetically limited by the anisotropic diffusion on the Si(001) surface, are below 350°C. Here, Ge forms elongated islands due to the diffusion anisotropy on the Si(001) terraces. Their aspect ratio decreases with increasing temperature. [71]

0.1 ML Ge coverage

Fig. 7-2 shows a 50 nm × 50 nm STM image of 0.1 ML Ge deposited onto 0.11 ML C / Si(001) at 350°C. Several small Ge islands of single layer height have nucleated on terraces (indicated by arrows). These islands are always surrounded by a certain number of buckled dimer rows in the terrace layer, which are assumed to be silicon. Although smaller islands of about 8 × 6 atoms dominate, larger islands are also found. The aspect ratio, however, is small compared to the more elongated islands reported on bare Si(001), although narrow islands are also present. The diffusion anisotropy on the surface seems to be reduced due to the presence of the c(4×4) regions. Ge ad-layer islands are not found directly on top of a c(4×4) area. Fig. 7-3 depicts a larger area of the same sample. The RMS roughness of this surface corresponds to (0.10 ± 0.01) nm and an island density of $(8 \pm 1) \cdot 10^{11}$ cm^{-2} is deduced at this coverage. If all Ge adatoms were contained in the islands, these would have an average size of 8 × 11 atoms or about (3.0×4.5) nm. But the islands are smaller in fact. This implies, that a substantial amount of Ge (~50%) is incorporated at step edges. The incorporation at S_B steps in places where the lower terrace is (2×1) reconstructed is favorable. It has been shown that the energy barrier for adatoms to cross S_B steps downwards, the Ehrlich-Schwoebel barrier, [98, 99] is small. [71] Presumably it is also energetically favorable for Ge atoms impinging onto a c(4×4) domain
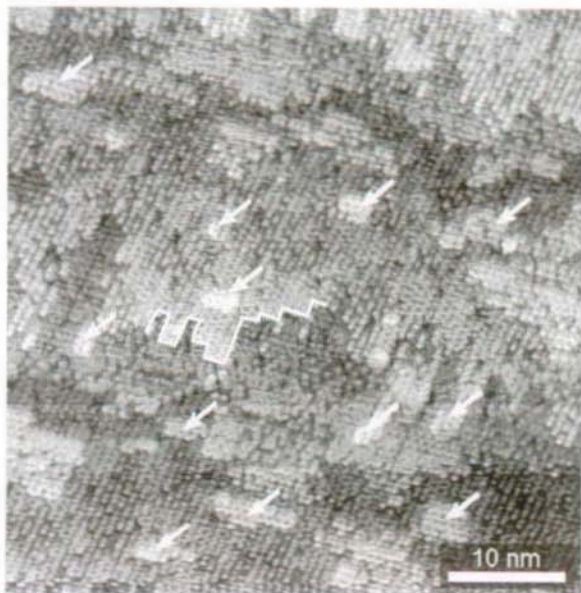
Fig. 7-2: STM image (-2 V, 0.17 nA) of 0.1 ML Ge deposited onto 0.11 ML C / Si(001) at a substrate temperature of 350°C and a flux of 0.01 ML/s. Arrows mark small single-layer Ge islands on the terraces surrounded by buckled dimer reconstruction. Islands are never found on top of carbon rich c(4×4) areas. A substantial amount of Ge is incorporated at step edges. A S_B step, where Ge might have gathered, is outlined.
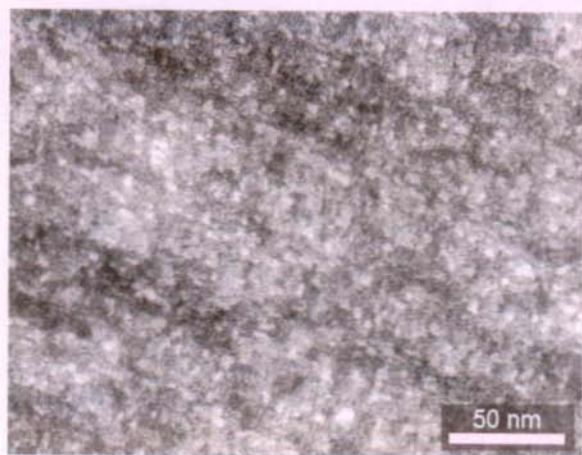
Fig. 7-3: 200 nm × 150 nm STM image (-2.4 V, 0.5 nA) of the same surface as in Fig. 7-2. The island density corresponds to ~(8 ± 1)·10^{11} cm^{-2}.

near an S$_B$ step to leave the domain by migrating step downwards. The outlined step edge in Fig. 7-2, where the terrace area behind exhibits c(4×4) symmetry, is therefore assumed to consist of Ge. A second layer island then prefers to nucleate on top of this Ge area, because the lattice mismatch is small here.

The observation, that the germanium atoms do not nucleate on the carbon rich c(4×4) reconstruction, is in perfect agreement with the finding of a repulsive interaction of Ge and C in this SiGeC material system.[62] It can be understood in terms of bond lengths and lattice constants. In the c(4×4) areas the Si surface is compressively strained due to the high carbon content. Consequently, the average lattice constant here is smaller than that of Si, which discourages the larger Ge atoms from nucleating in these areas. Furthermore, as there is also C present directly at the surface, the formation of Ge–C bonds would be very costly in energy, involving severe amounts of strain due to the difference in bond length of ~37%. Instead, the Ge tends to wet the Si(2×1) regions first, since they are unstrained or even tensilely strained in between the carbon-containing areas. The resulting lattice mismatch of less than 4% favors Ge nucleation on the Si(2×1) areas. In addition, at this low growth temperature the adatom diffusion is sufficiently slow to form islands on the terraces despite the small terrace width of about 10-15 nm.

0.5 ML Ge coverage

Increasing the Ge coverage to 0.5 ML, the island density raises only slightly to a value of (9.5 ± 1.0)·10^{11} cm^{-2}. The RMS roughness has increased to (0.15 ± 0.01) nm simultaneously. Consequently the islands grow in size and height. But their lateral extensions are somewhat restricted by the ubiquitous c(4×4) areas. Still, the Ge atoms seem to avoid the formation of

Ge-C bonds and therefore start nucleating on top of the existing islands, resulting in 3D island growth. The restructuring of the Si surface due to the C predeposition obviously forces Ge to grow in a Volmer-Weber mode rather than a Stranski-Krastanov mode at the given temperature. This 3D growth mode is demonstrated in Fig. 7-5, where many of the Ge islands clearly consist of two or even three layers. The line scan underlines this experimental finding. The area between the islands is mainly c(4×4) reconstructed. Islands have most frequently a rectangular shape with a low aspect ratio. The edges are aligned along ⟨110⟩.

An interesting observation is that most of the 3D islands are located at step edges. They virtually form the border between adjacent terraces in those places, where the c(4×4) reconstruction does not reach the step edge. In Fig. 7-5 the terraces descend from the top of the image to the bottom. The line scan starts on a lower terrace across the island and ends one ML above on the upper terrace, as indicated by the white line in Fig. 7-5. The highest islands are predominantly found at the steps having S_B character, where we already assumed the agglomeration of the Ge not seen as islands at a coverage of 0.1 ML. Islands in the center of a terrace remain somewhat smaller and flatter. A possible explanation is the following: due to the enhanced surface diffusion along dimer rows on the upper terrace Ge adatoms migrate towards the step edge, descend and are incorporated there, which corresponds to the initial stages of a step flow mode. But the lateral extension of this first monolayer of an island is restricted when it approaches the c(4×4) regions on the lower terrace, because of the reluctance to form Ge-C bonds. From then on, the presence of c(4×4) areas on the lower terrace acts as a barrier that prevents new Ge adatoms from descending the Ge step and from growing further in step flow mode. Instead, the Ge atoms start to pile up by preferential
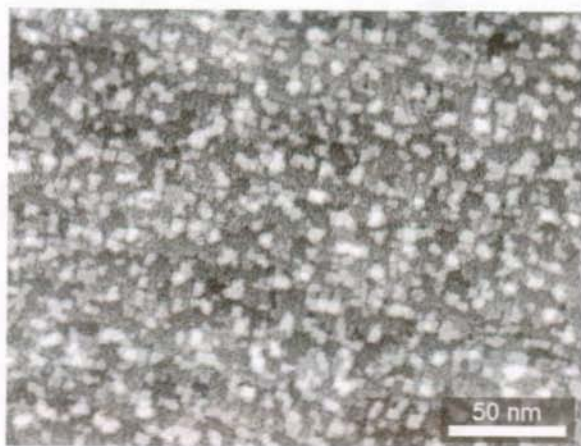

Fig. 7-4: STM image (-2.3 V, 0.2 nA) (200 nm × 150 nm) of 0.5 ML Ge deposited on 0.11 ML C / Si(001) at a substrate temperature of 350°C and a Ge flux of 0.01 ML/s. Island density corresponds to $(9.5 \pm 1.0) \cdot 10^{11}$ cm^{-2}. The island sizes are small (3 – 4 nm), but 3-dimensional.
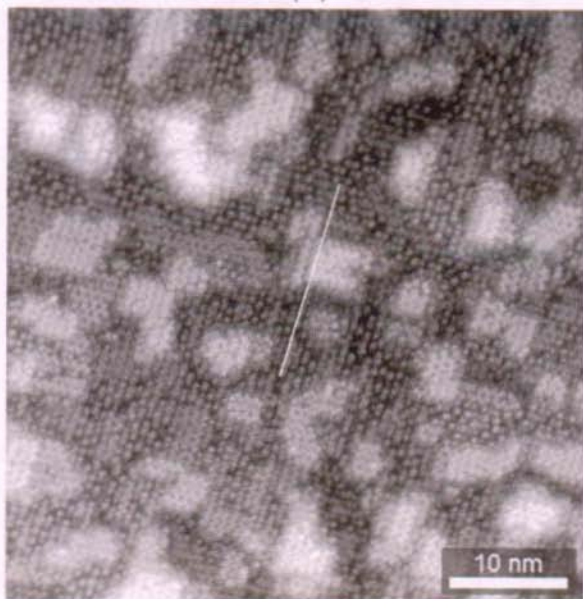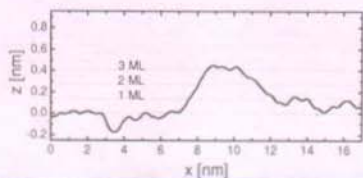
Fig. 7-5: STM image (-2.3 V, 0.2 nA) of 0.5 ML Ge on 0.1 ML C /Si(001), same sample as in Fig. 7-4, image size 50 × 50 nm. Islands started to pile up to 3-4 ML height. They are laterally restricted by the Ge-repelling c(4×4) patches. The line scan follows the white line from the lower left to the upper right. High islands are predominantly found at steps.

nucleation on top of these existing Ge areas, where they can most easily accommodate to the lattice constant. So the 3D growth is driven by strain relaxation, because the carbon enriched Si surface areas have a smaller average lattice constant. Note, that some of the larger flatter islands exhibit the missing dimer rows known from the relief of strain in thin Ge ad-layers on Si(001).

1 ML Ge coverage

The evolution of the 3D islands outlined above continues towards higher Ge coverage. At 1 ML Ge deposited at 350°C the Ge still does not cover the whole surface but instead keeps growing as 3D piles. Therefore, the RMS roughness increases to (0.23 ± 0.01) nm. The island density slightly decreases to $(8 \pm 1) \cdot 10^{11}$ cm^{-2}. The island diameters increase to 4 - 5 nm, the height increases and the size distribution slightly broadens. In areas between the islands the

unperturbed c(4×4) reconstruction is still completely visible. Fig. 7-6 and Fig. 7-7 show the surface morphology for 1 ML Ge coverage. A line scan of a 6 ML high island is also depicted.

It is remarkable, that the shape of the basis of the higher islands becomes more irregular with respect to 0.5 ML, where the rectangular shape dominates. More rounded shapes are now also found and the longer axes of many islands deviates from the ⟨110⟩ direction. The reason may be the coalescence of neighboring islands. It is difficult to determine the side facets of these relatively small islands. No distinct facet reconstruction can be seen because side walls are irregular. Nevertheless, a certain affinity to side facet formation either in ⟨100⟩ or ⟨110⟩ directions is visible in the images. Most likely the facets are made up from close trains of S_A and rebonded S_B steps along ⟨110⟩ and (104) facets along ⟨100⟩, having inclination angles of $-11°$ to $-15°$ with respect to the (001) surface.

The small (001) top facets of the high islands are perfectly (1×2) reconstructed, indicating
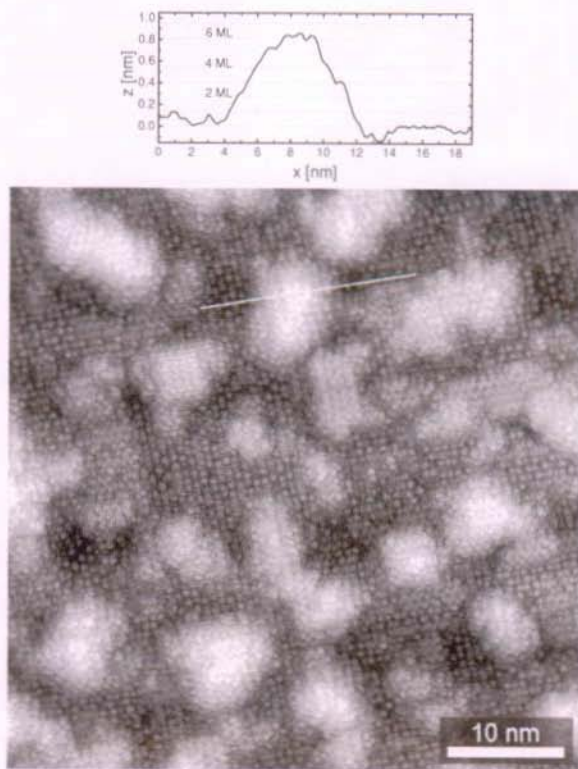
Fig. 7-6: 50 nm × 50 nm STM image (-2.4 V, 0.2 nA) of 1 ML Ge on 0.11 ML C/ Si(001). Deposition was performed at a substrate temperature of 350°C and a Ge flux of 0.01 ML/s. Between the islands the c(4×4) areas are left untouched by the Ge. The island shapes are more irregular with respect to lower coverage. The line scan taken at the position of the white line shows an island of 6 ML height.
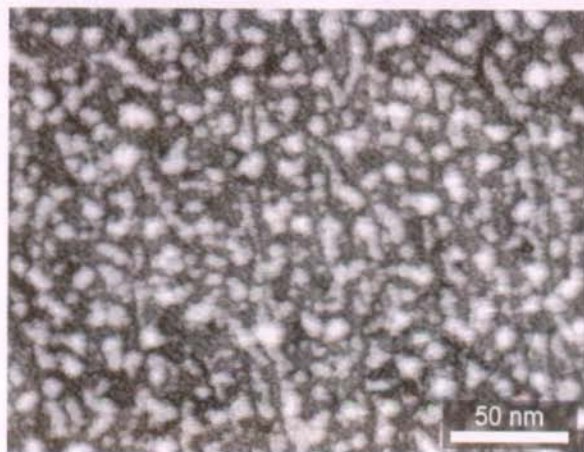
Fig. 7-7: STM image (-1.5 V, 0.2 nA; size 200 nm × 150 nm) of the same surface as in Fig. 7-6. The island density is $(8 \pm 1) \cdot 10^{11}$ cm^{-2}. Islands are higher and slightly larger than for the corresponding structure at 0.5 ML Ge coverage

that they are to a large extent relaxed towards the apex, due to their small lateral extension. The height to base length ratio of the high clusters is ~1/10, similar to relaxed hut clusters. The flatter islands on the other hand still show the missing dimer rows to relieve the strain, when they are larger than n dimers [(2×n) structure].

We point out, that up to this coverage *no Ge wetting layer* is formed. Instead, the area between 3D islands is made up exclusively from the C-rich $Si_{1-x}C_x$ alloy. We assume that virtually no Ge incorporates into the c(4×4) regions, since this would almost certainly alter the appearance of these regions in the STM images. The reason is, as explained above, the repulsive interaction between Ge and C, which is a result of the large local strains that would be associated with such a mixture. [62]

The size of about 5 nm of these well developed 3D islands at 1 ML Ge and the absence of a Ge wetting layer is appealing, as small size favors zero-dimensional properties such as symmetry-allowed direct optical transitions. Carrier localization will be much enhanced due to the small distances of less than 10 nm between dots, which is in the range of the exciton radius in SiGe. [85] Thus it seems to be worth exploring these small and dense GeC-dots with PL in the future. Due to the small size the crystallographic perfection is presumably maintained despite the low growth temperature. However, the capping of these dots with Si remains a factor of uncertainty, since it is a priori not clear, if these small dots would survive as Ge clusters or if segregation would rather lead to a thin SiGeC quantum well instead.

7.3 Ge deposition at $T_{sub} = 550°C$

We have demonstrated, that using a substrate temperature of 350°C, the Ge is completely repelled by the C rich areas on 0.11 ML C / Si(001) surfaces and grows three-dimensionally in a Volmer-Weber mode. For thicker Ge films such as of 2.5 ML and more, grown at 550°C, islands with a density of $1 \cdot 10^{11}$ cm^{-2} have been detected whereby the c(4×4) reconstructed areas have disappeared (chapter 6.2). Consequently, Ge is assumed to be intermixed with the $Si_{1-x}C_x$ areas at this temperature and coverage. The evolution of Ge growth below one monolayer is further investigated to uncover the process of intermixing and island formation at 550°C.

0.5 ML Ge coverage

Fig. 7-8 represents a 50 nm × 50 nm STM image of 0.5 ML Ge on 0.11 ML C / Si(001). At first glance, the Ge growth is now dominated by steps flow. The image is stepped downwards from the right to the left. It has been shown for the C-precovered surface, that the c(4×4) areas are formed preferentially at the step edges, so that these are usually terminated by the c(4×4) pattern. After the deposition of 0.5 ML Ge, the areas around steps are mostly terminated by (2×1) reconstructions. This behavior is more pronounced for S_A type steps, as demonstrated by the long narrow (2×1) reconstructed stripe running from the top middle to the lower right of the image. This area is expected to consist of Ge indicated by the characteristic missing dimer superstructure. It adjoins on the right hand side to a c(4×4) reconstructed area, which is believed to be located at a terrace edge before Ge deposition.

In contrast to the S_A steps, the S_B steps are still often formed by c(4×4) rows. All in all one still finds a lot of c(4×4) areas, either at step edges or surrounded by Ge or Si. That means, even at this substrate temperature of 550°C Ge is repelled by the C rich areas. A certain amount of intermixing between Ge and C, however, cannot be ruled out, since some of the (2×1) reconstructed areas contain – in addition to the strain relieving perpendicular missing dimer rows – rows with a periodic train of missing dimer defects (indicated by arrows in Fig. 7-8). In these rows only every third or fourth dimer is visible, a structure not usually observed in Ge or SiGe adlayers. Furthermore, small c(4×4) patches are found in direct vicinity or even on top of the areas believed to consist of Ge.

The growth does, however, not proceed in pure step flow mode. On top of the islands a second layer has nucleated. The islands reach relatively large sizes (compare upper middle of Fig. 7-8), but small ones are also present. These islands are also seen on a larger scale (compare Fig. 7-9). Islands with extensions of about 20 nm are dominant, having rather isotropic shape, i.e. without preferential directions of elongation. On all of them the Ge missing
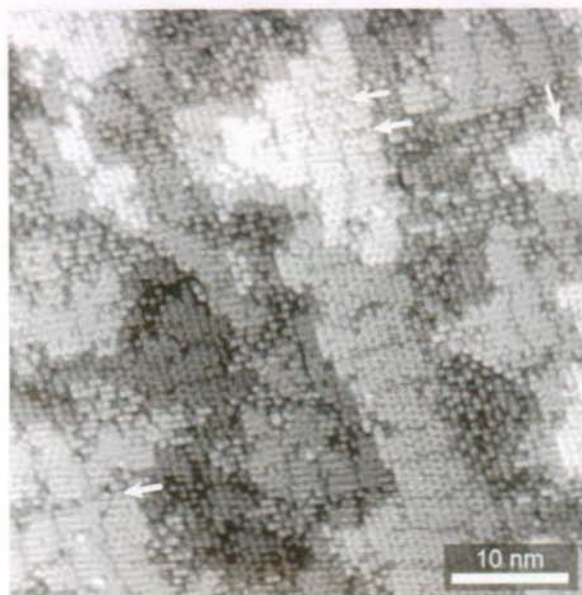
Fig. 7-8:   STM image (-2.4 V, 0.18 nA; size 50 nm × 50 nm), of a surface covered with 0.5 ML Ge deposited at 550°C on top of 0.11 ML C / Si(001) at a rate of 0.1 ML/s. The growth is rather 2- than 3-dimensional, but two ML high islands are also formed. Still Ge is basically repelled by the C-rich regions, but some intermixing cannot be ruled out, indicated by the arrows that mark unusual structure within the Ge adlayer.

dimer rows are developed. Large islands exist predominantly in the vicinity of steps. The RMS roughness is determined to be (0.10 ± 0.02) nm.

It should be mentioned that the nucleation of a third layer on top of the large islands is rarely observed, indicating, that the diffusion length of Ge adatoms on these large islands is higher than the island diameter and the activation barrier for diffusing down the island edges is overcome at this growth temperature. This observation may be caused by different diffusion lengths on terraces and on islands. If they were identical one should find pure step flow growth, especially for the small terrace width of the substrate. Therefore, intuitively, one can conclude, that the diffusion on the terraces is hindered by the presence of the C-rich c(4×4).

Counting the islands on this surface by a gray scale discrimination and thresholding procedure, an island density of $(3 \pm 1) \cdot 10^{11}\,cm^{-2}$ is derived. This value is only a factor of three lower compared to the island density at 350°C. This difference in island density upon the large temperature difference of 200 K is remarkably small. From Si [100] or Ge nucleation on bare Si(001) surfaces one expects a drop of the island density by several orders of magnitude, because diffusion is a thermally activated process. [101] Even though the procedure for island counting, which involves leveling of the stepped surface, is not very accurate for large flat
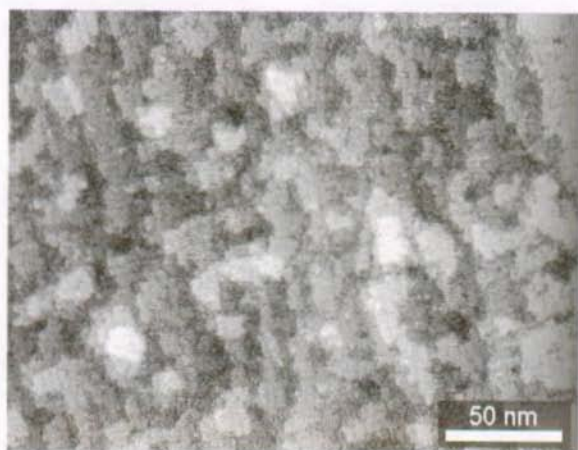
Fig. 7-9: Larger scale STM image (-2.0 V,, 0.2 nA; 200 nm × 150 nm in size) of the 0.5 ML Ge / 0.11 ML C / Si(001) surface of Fig. 7-8. The island density is determined to be $(3 \pm 1) \cdot 10^{11} cm^{-2}$.

islands, because it leads to an average inclination of the terraces and eventually also protruding parts of step edges are counted, the order of magnitude of the island density remains without doubt correct. Hence, it is the presence of the C-rich c(4×4) reconstructed areas that modifies the fundamental process in Ge growth.

As already pointed out in the introduction of this chapter a certain amount of intermixing between Ge and the Si within the first monolayer is expected at 550°C. It was predicted to be below 25% [96]. Thus the (2×1) dimer reconstructed areas in the substrate layer and the first monolayer are most probably a $Si_{1-x}Ge_x$ alloy. This is Si-rich in the substrate layer and Ge-rich in the first ad-layer. The second layer consists almost exclusively of Ge.

1 ML Ge coverage

Fig. 7-10 shows an STM image of the surface after one monolayer Ge deposition at 550°C. Note, the surface exhibits substantial amounts of c(4×4) reconstructed areas. Even at 550°C the Ge does not wet the whole surface but is still essentially repelled by the C rich areas. The island growth is more pronounced for monolayer coverage than for 0.5 ML. The RMS roughness has increased considerably to (0.17 ± 0.02) nm. Some islands have a height up to 6 ML. The largest islands have sizes of 10 to 15 nm. The majority of islands, however, is flat, rarely exceeding a height of three monolayers. The island density remains constant at a value of $(3 \pm 1) \cdot 10^{11} cm^{-2}$. The large islands are expected to grow on top of the large two layer high islands found at 0.5 ML, whereas the smaller islands do not pile up further. This is understandable since the growth of the smaller islands, which is probably laterally restricted by the strain in surrounding areas, would lead to steeper sides, which is unfavorable in terms of sur-
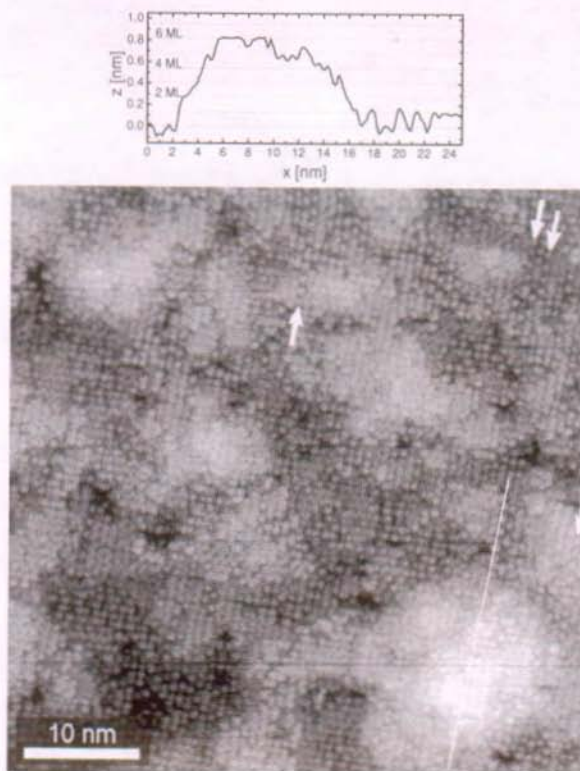
Fig. 7-10 STM image (-1.5 V, 0.2 V; 50 nm × 50 nm) of 1 ML Ge on 0.11 ML C / Si(001). Some large and high islands (see line scan) and many smaller and flatter islands not higher than three atomic layer are present The c(4×4) areas are partly disordered, indicating some Ge incorporation.

face energy. Furthermore, the supply of the small islands with adatoms is kinetically restricted as they have a smaller capture area.

Intermixing of Si and Ge depends primarily on the substrate temperature, but as for any thermodynamic mixing (diffusion) process the particle density is involved, too. Therefore at higher Ge coverage intermixing is expected to become more important. Consequently the c(4×4) areas become more disordered compared to 0.5 ML Ge. In some places the same unusual rows with periodically missing dimers are found as for 0.5 ML Ge (see arrows). This could be interpreted as a sign for a partial intermixing of Ge and Si in C rich areas.

In conclusion, there is no wetting layer of Ge even after 1 ML at 550°C. So even at this substrate temperature the growth mode is of a Volmer-Weber type. It is definitely not Stranski-Krastanov growth as observed on bare Si(001).
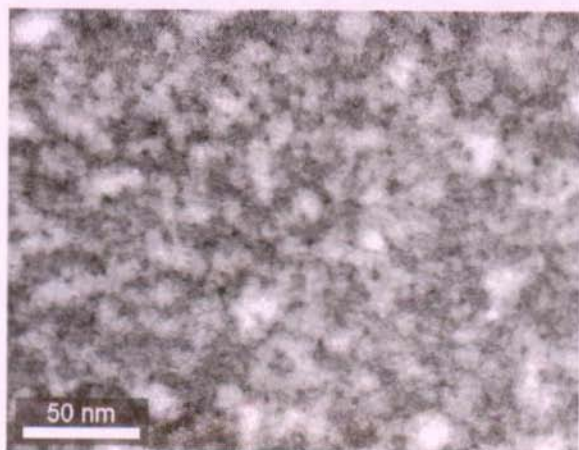
Fig. 7-11: 200 nm × 150 nm STM image (-2.2 V, 0.2 nA) of 1 ML Ge deposited at 550°C. The island density still is about $(3 \pm 1) \cdot 10^{11}$ cm^{-2}, with a broad size distribution.

For a realistic description it should be mentioned, that the step density of the substrates is relatively high. The terrace lengths of about 15 to 20 nm corresponds to an arbitrary miscut of 0.4° to 0.5°, which in addition can vary in direction from wafer to wafer, although they originate from the same series. Hence, the terrace width is comparable to the lateral size of the 3D islands. Undoubtedly the steps do affect the island nucleation and, therefore, alter the island size and density. Nevertheless, the general finding of the non-wetting of the c(4×4) areas resulting in Volmer-Weber growth will also be true on larger terraces.

7.4 Quantification of island morphologies

Island heights and profiles

In order to compare the morphologies of the samples grown at 350°C and 550°C in a quantitative way, island heights and island sizes have been evaluated in detail. To get reasonable statistics, the STM images larger than 40000 nm² and exhibiting more than 100 islands are used. As these have many steps (>50), single terraces cannot be treated individu-
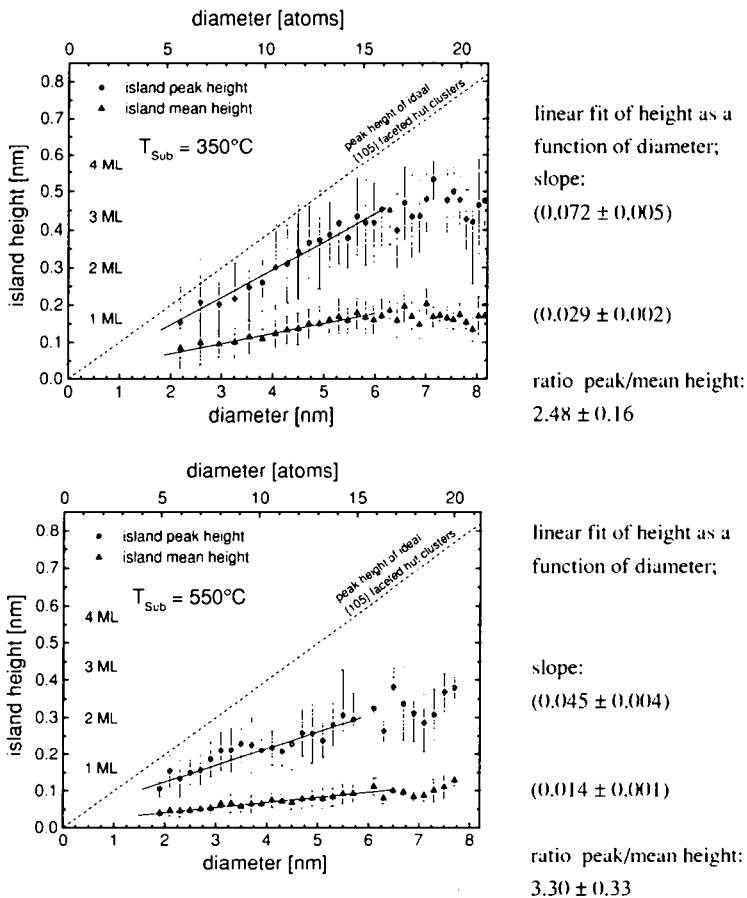
Fig. 7-12: Island peak heights and mean heights as a function of island diameter for 1 ML Ge deposited at 350°C and 550°C. Data is derived from STM images.

ally. Instead the whole image is leveled, leading to an average inclination of every terrace that corresponds to the miscut angle of the wafer. The resulting topography is evaluated by means of a particle count algorithm, that determines height and size of islands that exceed a certain threshold height. The threshold value is set for each image as the sum of the mean height plus the respective RMS roughness value of the particular image. Only islands are counted, that protrude above this threshold. As the islands are distributed on terrace edges as well as in the center of terraces, the threshold intersects islands, that are in different positions on an inclined terrace, at different levels between 0 and 1 ML. This leads to a quasi-continuous height distribution, although in reality the island height is of course an integer number of monolayers. In addition, an average is taken over all islands of the same size, where the smallest unit of measure is that of an image pixel. The standard deviation of this average is given as error bars. In Fig. 7-12 a) and b) the island heights are plotted versus the island diameter for the samples consisting of 1 ML Ge on 0.11 ML C / Si(001), grown at 350°C and 550°C, respectively, at a rate of 0.013 ML/s. Circles represent the island peak height and triangles the mean island height, i.e. the total island volume divided by the area of the island basis. On average, the island height increases monotonously with the island size for both substrate temperatures. This behavior confirms, that the growth proceeds in a 3-dimensional manner in the whole temperature range investigated. At 350°C the islands are always higher than at 550°C for a given size. That means, their aspect ratio is higher, namely (0.072 ± 0.005) at 350°C compared to (0.045 ± 0.004) at 550°C. This is another indication for the fact, that the 3D growth is more pronounced for the lower substrate temperature. However, in both cases the islands remain flatter than ideal hut clusters with a square base. These have an aspect ratio of 0.10, indicated by the dashed diagonal line in Fig. 7-12. Furthermore, the islands grown at 350°C are more compact than at 550°C. This can be seen by comparing the ratio between island mean and peak height for both temperatures. Theoretically this ratio would be unity for a box-like island profile with vertical side walls, and three for an ideal pyramid. For the islands grown at 350°C this ratio is 2.48 ± 0.16 which corresponds to a truncated pyramid with a flat top facet, that has about 0.12 – 0.24 times the diameter of the island base. This is in agreement with the observed islands as shown in Fig. 7-6. At the substrate temperature of 550°C the ratio yields 3.30 ± 0.33. This is somewhat larger than for an ideal pyramid and can be explained by the low aspect ratio. The islands are usually only two to three monolayers high and in this height range the discrete steps forming the "sides" of the islands as well as the small inclination of the terraces must be taken into account. So the ratio corresponds to low island profiles with widely spaced steps on the sides.

The islands found here are not as high as hut-clusters of identical lateral size. Flatness increases with increasing substrate temperature. However, this analysis corroborates the 3D character of island growth in the monolayer range.

Island size distributions

The evaluation of scaled island size distributions in nucleation experiments can provide additional information about the growth process. A scaled island size distribution is obtained by plotting the scaling function $f(s/S_{Av}) = S_{Av}^2 N_s/\theta$ versus the ratio s/S_{Av}. [102] Here s is the size of the individual island, S_{Av} the average island size of the counted islands, N_s the number of islands with size s and θ the coverage due to deposition. The scaling function is normalized so that integration over s/S_{Av} yields unity. Experimentally, the size distribution is deduced from STM images by counting islands and measuring their size. Islands of similar size are combined into classes to give a histogram. One can show, that the scaled distribution function can simply be written as $f(s/S_{Av}) = N_s / N_{total}$, where N_{total} is the total number of islands of the evaluated STM image.

In case the saturation island density is reached, i.e. the density is no longer limited by the supply of adatoms, the scaled island size distributions of different coverage have to collapse into one curve, if the samples are grown under identical growth conditions. However, this is only the case in the aggregation regime up to a coverage where island coalescence becomes important (coalescence regime). [102]
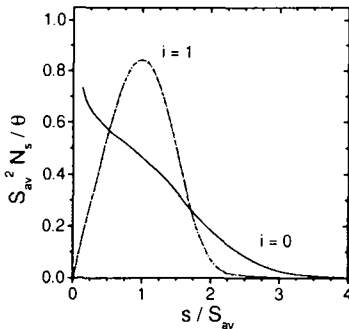

Fig. 7-13 Theoretical scaled island size distributions for different critical island sizes, taken from Ref. [103].

According to theoretical calculations the actual shape of scaled size distributions depends on several parameters, like the diffusion over impinging flux (D/F) ratio and the critical cluster size i. For $i = 0$ (a stable monomer) simulations on a square lattice yield a monotonic decrease of the distribution function, whereas for $i \geq 1$ (stable dimers or larger clusters) the distribution function peaks around $(s/S_{Av}) = 1$ and becomes higher and sharper with increasing i [103] (see Fig. 7-13). Size distributions become slightly sharper at higher D/F ratio, i.e. at higher substrate temperature. [104] So in principle it is possible to draw conclusions about these parameters by comparing suitable experimental distributions with the theoretical plots.

However, such a comparison is only straightforward in case of unperturbed nucleation on smooth terraces of sufficient size, where kinetics is governed solely by surface diffusion. If these requirements are not met, a quantitative interpretation may be impossible. In the system of Ge deposition onto C / Si((X)1) considered here, there are several reasons that obstruct such an interpretation. First of all, the mean terrace width is only 10-15 nm, so that step edges have an impact on nucleation. Furthermore, the C predeposition makes the surface inhomogeneous on nanometer scale, altering the diffusion behavior of the adatoms and the island nucleation. Nevertheless, the scaled island size distributions are evaluated for 0.5 ML and 1 ML Ge

a)
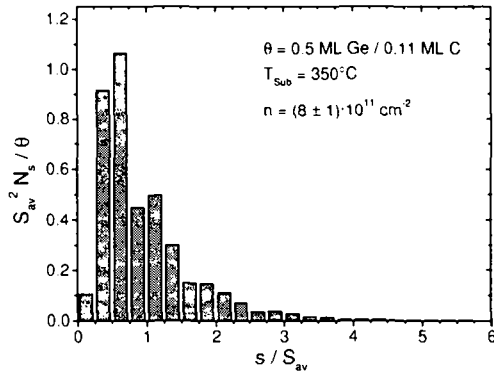
b)
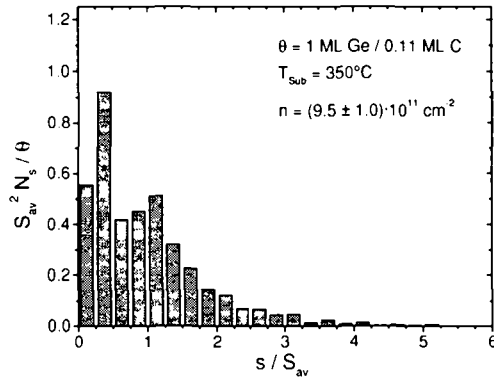
Fig. 7-14: Scaled island size distributions for a) 0.5 ML Ge and b) 1 ML Ge deposited at a substrate temperature of 350°C and a flux of 0.013 ML/s. Both distributions coincide nearly perfectly.

deposited at 350°C and 550°C. One would expect, that the distributions qualitatively reflect the influence of the C-predeposition and the 3D growth.

The scaled size distributions for the 350°C deposition are plotted in Fig. 7-14. It is striking, that histograms a) and b) with the different coverages of 0.5 and 1 ML Ge, respectively, reveal almost identical distributions, as predicted by scaling theory. [102, 105] The fact, that scaling is applicable even for monolayer coverage, shows that the system is still in the island aggregation regime for 1 ML, which is only possible at this coverage due to 3D growth.

Although at this substrate temperature of 350°C for homoepitaxial growth on Si(001) a small critical island size is expected [106] and Ge behaves very similar to Si in the sub-monolayer range, [71] the shape of the histogram cannot be assigned to a certain i. The overall shape for $s/S_{Av} \geq 1$ may resemble roughly to an i = 0 shape, since the distribution decays slowly

a)
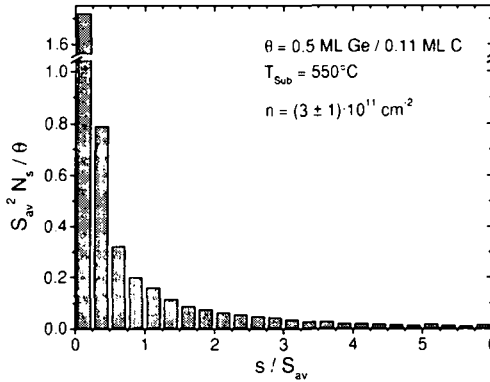
b)
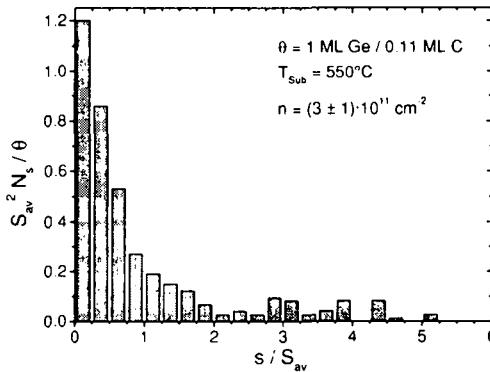
Fig. 7-15: Scaled island size distributions for a) 0.5 ML and b) 1 ML Ge deposited onto 0.11 ML C / Si(001) at a substrate temperature of 550°C. Both histograms reveal a high number of small islands and a nearly exponential decay towards large islands.

and extends to large islands with $s/S_{Av} \geq 4$, but looking at the corresponding STM images it is immediately clear, that a monomer cannot be the stable cluster. Potentially the similarity to $i = 0$ behavior of the island size distribution is related to the C-predeposition, that restricts island formation to the areas with low C concentration and thus offers preferential sites of nucleation. This would be similar to island nucleation at point defects, where $i = 0$ has been found, with the difference of much larger average island size in our case.

Fig. 7-15 shows the scaled island size distributions of the samples where Ge has been deposited at 550°C onto the C-precovered surface, again for a) 0.5 ML and b) 1ML Ge coverage. Even here, both distributions closely resemble each other, indicating that the scaling is applicable because of 3D growth. The distributions reveal the dominance of small islands, then

decay rapidly in an exponential manner. The tail of the distributions includes large island sizes with $s/S_{Av} \geq 6$. The nature of these distributions is not yet clear. Its shape does not correspond to any theoretically predicted distribution. Possibly the leveling and island count algorithm used for the evaluation of the islands overestimates the mean island sizes for the large flat islands on small terraces, because it may also count large protruding terrace edges as islands. This would lead to a shift of the scaled distribution to considerably lower s/S_{Av} ratio and may explain the high count for the small islands.

The essence of this section is, that for both temperatures the distributions do scale with coverage for coverages as high as 0.5 and 1 ML. This is another strong support for the immediate 3D growth, i.e. the Volmer-Weber mode of this system, since for 2D growth the percolation limit leading to massive island coalescence would already be exceeded, so that scaling would not be applicable. The scaled distributions are different for the different growth temperatures, which can be related to the kinetics on the C-precovered surface. Very likely the C-restructuring in the form of the c(4×4) reconstructed areas plays a crucial role for the determination of the scaled island size distribution shapes. This relationship may be explored in more detail in a future work.

7.5 Evolution of morphology towards multilayer Ge coverage

When reaching multilayer Ge coverage at the substrate temperature of 550°C, as presented in chapter 6.2, the c(4×4) reconstructed areas finally disappeared completely. An example is given in Fig. 7-16 for 2.5 ML Ge. Note, that the coverages above 1 ML have been deposited at a higher deposition rate of 0.16 ML/s Ge. No c(4×4) reconstructed areas are detected anymore. But the rows with periodically missing dimers, that are already present at 0.5 ML and 1 ML, are found even at this Ge thickness as indicated by arrows in Fig. 7-16. This kind of reconstruction rows, where every fourth dimer position is decorated by a bright spot and the remaining dimers are missing, are attributed to intermixing of Ge with the C-rich structure. This observation implies, that at a certain thickness beyond 1 ML Ge starts to wet also the C-rich areas. This may be related to the fact, that the 3D islands do not only grow in height but more rapidly in lateral size, thus extending over the initially c(4×4) reconstructed areas. It may also be attributed to thermodynamics, since the increased overall Ge concentration can drive the system towards a SiGeC alloy by interdiffusion. The island shapes remain irregular. The island density at 2.5 ML compared to 1 ML is reduced by a factor of three to a value of about $\sim 1 \cdot 10^{11}$ cm^2, i.e., coalescence or a rearrangement of islands takes place. The RMS roughness on the other hand remains roughly constant at (0.16 ± 0.02) nm.

Fig. 7-17 depicts the evolution of RMS roughness and island density depending on the Ge coverage for deposition at 550°C. Up to a Ge coverage of 1 ML the island density and the RMS roughness are to a wide extent governed by the c(4×4) restructuring of the surface,
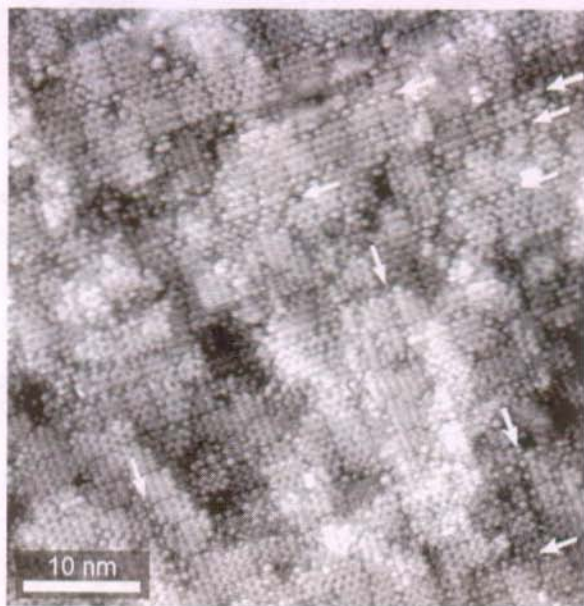
Fig. 7-16: STM image of 2.5 ML Ge on 0.11 ML C / Si(001), deposited at a rate of 0.16 ML/s at a substrate temperature of 550°C. The island density is decreased to ~$1 \cdot 10^{11}$ cm^2 indicating coalescence. No c(4×4) reconstruction is detected anymore. The rows with missing dimer pattern (indicated by the arrows), that presumably stems from intermixing of with the carbon rich areas, is also observed here. Its appearance decays towards Ge-coverages higher than 2.5 ML, indicating that the C-rich areas are covered more and more with Ge.

restricting Ge nucleation to C-less Si(2×1) regions. The lateral extension of islands is thereby limited. Between 1 ML and 2.5 ML the RMS roughness seems to pass through a maximum and the island density decreases simultaneously. This transition is attributed to the process of increasing Ge coverage on the C-rich areas with simultaneous island coalescence.

In the final state of disappeared c(4×4) areas at 2.5 ML, the 3D islands are surely still centered above the initially (2×1) reconstructed substrate areas with low or no C content. This strongly supports the model given in section 6.3, Fig. 6-17 b) to explain the PL emission of these samples.

We are aware, that the comparison including different growth rates for coverages < 1ML and >2.5 ML is not unambiguous. A higher deposition rate could favor the overgrowth or the intermixing of the C-rich areas, since the faster Ge atom impingement causes on average a higher Ge concentration on top of these areas. On the other hand, at higher Ge flux a higher overall island density is expected, if the diffusion rate remains comparable. However, the surface diffusion, that is according to our experimental findings different on C-rich c(4×4) and on Si(2×1) areas, probably changes in the course of the disappearing c(4×4) and becomes more homogeneous over the whole surface.
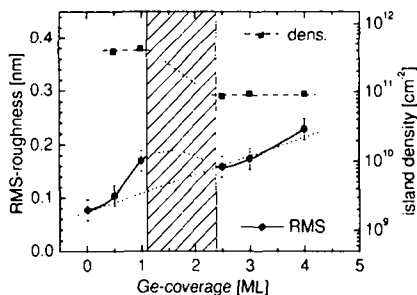
Fig. 7-17: Evolution of RMS roughness (solid line) and island density (dashed line) as a function of Ge coverage. Ge deposition was done at a substrate temperature of 550°C. Note, that the Ge flux is different for coverage < 1ML and > 2.5 ML (see text). The transition region between 1 and 2.5 ML is attributed to the process of Ge overgrowth/intermixing of/with the C-rich areas, accompanied by island coalescence.

Conclusion

The basic observation of this chapter is, that on the C-restructured Si(001) surface the Ge starts forming 3D islands right from the beginning of deposition. Hence the growth mode is Volmer-Weber growth and no Ge wetting layer is formed. Especially the formation of high-density but isolated ultra-small Ge islands at lower growth temperature is a promising result offering good prospects for potential light emitters based on SiGe technology. However, the evaluation of their optical properties and of Si capping remain topics for future work.

The irregular islands at higher coverage (above 2.5 ML) arise from the small islands by coalescence and a gradual intermixing or coverage of the C-rich areas with germanium. These findings have some implications on the results from the previous chapter. First of all they back the spatially indirect recombination model for the origin of PL emission. It is clear now, that the second model given in Fig. 6-17 b) is applicable, since the GeC dots are clearly lying above the areas containing no carbon. The patches with high C-concentration are thus positioned in between the 3D-islands. Possibly, they are covered with a very thin Ge layer, that interconnects the island, or have intermixed into a SiGeC alloy. This layer will then become thicker with increasing Ge coverage and, hence, reduce the well defined carrier confinement of electrons in the C-rich Si areas and of holes in the Ge-dot. So finally, this can explain the rapid decay of PL emission with increasing Ge deposition observed in the previous chapter, that has its maximum around 2.5 ML Ge and almost vanishes at 4 ML already.

So far, the nucleation of GeC islands is a self-organized, but somewhat random process, that is governed by the growth kinetics in the presence of the random distribution of the c(4×4) domains and monatomic substrate steps. It would now be desirable to intentionally influence the island formation by control of some other external parameters, in order to ameliorate island distribution and lateral order. One such parameter, that can relatively easily be controlled, is

the step distribution on the initial Si((X)1) substrate. Exploiting the step structure of vicinal substrates it is possible to create preferential nucleation sites for islands. This has already successfully been used to tailor size and arrangement of larger SiGe islands, where in addition the elastic interaction between the islands is important. [107, 108]

The Si((X)1) surface forms almost exclusively single height steps up to a miscut angle of 2° in [110] direction. [109] The average terrace width at 2° is about 4 nm. If the miscut is tilted towards [100] instead, steps become zigzag-shaped due to alternating sections of S_A and S_B character (compare Fig. 4-6). If the tilt angle is chosen large enough, one might obtain an overall slope consisting of small square shaped terraces in the ideal case (e.g. 4×4 nm²). Carbon deposition onto this checkerboard surface will favor c(4×4) domain formation at the step edges then, which might force the subsequent Ge island formation to be restricted to the remaining (2×1) area on each terrace. Ideally one can think of obtaining single Ge islands per terrace that are arranged in a regular square pattern. In this approach, the miscut angle towards [100] direction would determine the limits for Ge island size and density simultaneously.

This suggestion may be a viable approach to a more controlled tailoring of the GeC dots.

8 Conclusion and Outlook

The present thesis gives a detailed description of all stages of self-organized Ge quantum dot formation on Si(001), mediated by the presence of a submonolayer C-coverage. A long term goal of this work is to contribute to the development of light emitting Si structures, that can potentially be implemented into future Si based optoelectronic devices.

The ultra-high vacuum scanning tunneling microscope for the in-situ investigation of the surface morphology evolution has been especially designed and build within this work to suit the demands of the existing SiGe MBE system. This included the solution of experimental challenges, like the requirement of atomic resolution capability despite the large thin 4-inch substrates. For a more comprehensive picture of the surface morphology, the STM observations were combined with RHEED for in-situ monitoring of the epitaxial growth and the long range surface symmetry. Deeper insights into the evolution of Ge dots after they have been embedded in Si were gathered by cross sectional TEM. Photoluminescence spectroscopy has been applied for the optical characterization.

Starting from clean Si(001) (2×1), the modification of this surface by submonolayer C-predeposition into domains of a C-rich c(4×4) reconstruction has been shown. The development of a structural model for this reconstruction, which is supported by density functional theory and total energy calculations, has revealed the atomic composition, that comprises a complex of six C-atoms per c(4×4) unit cell. This complex consists of a C surface dimer and its four next nearest neighbors in the first sub-surface layer. The two adjacent Si dimers, that are pulled towards each other by the strain from the C-complex, are the features that are observed in the STM images.

The c(4×4) reconstructed domains have a profound impact on the subsequent Ge growth. On the C-precovered surface the Ge island formation proceeds in Volmer-Weber mode and no wetting layer is formed, which is a result from the strain induced repulsive interaction between Ge and C atoms. This is in contrast to the Stranski-Krastanov mode of Ge growth on bare Si(001). The evolution of the Ge nucleation proceeds via the formation of very small multilayer islands in between the C-rich c(4×4) domains and at step edges at coverages below 1 ML, which grow in size upon further Ge deposition. The 3D character of the small islands becomes less pronounced with increasing growth temperature. Gradually, Ge starts to intermix with the c(4×4) areas, favored by higher substrate temperatures and by higher coverage. At 2.5 ML and 550°C the carbon reconstruction of 0.1 ML C has completely disappeared. Simultaneously the Ge dots grow in size and height. Up to a Ge coverage of 4 ML the Ge dot shape is irregular without distinct facets. Facet formation resulting in hut-cluster like dot shape

with flat top is observed at Ge coverages of more than 5 ML at 550°C and 0.11 ML predeposited C. In general, on C-precovered Si(001) the dot formation sets in at lower coverage than on bare Si(001). In all cases where dots are present on both, bare and C-restructured surfaces, those on the C-precovered Si(001) surface are smaller and denser than their equivalents on bare Si prepared under otherwise identical growth conditions. This reflects the different kinetic limitations on both types of surfaces.

The PL investigations of GeC dots on 0.03 to 0.3 ML C / Si(001) in the Ge coverage range of 2.5 to 4 ML and growth temperatures between 350°C and 750°C reveal, that the optimum luminescence properties are obtained between substrate temperatures of 450°C and 550°C and a Ge coverage of 2.5 ML for 0.11 ML C. These samples exhibit intense dot related PL lines, consistent with TEM cross sections, that show the most pronounced dots at the same parameters.

The photoluminescence of these GeC dots, however, is governed by non radiative Auger recombination, although the PL lines are much more intense than the Si bulk signals. This recombination path hampers an efficient radiative recombination, especially at high excitation density.

To significantly reduce Auger recombination, it is necessary to limit the occupation of the dots, which would be possible by reducing the dot size and increasing their density. Here, the submonolayer Ge coverages may provide a solution. Especially for less than 1 ML Ge and a growth temperature of 350°C, the formation of isolated ultra-small three-dimensional Ge islands with sizes of 3 - 5 nm in diameter and a density of nearly 10^{12} cm^{-2} has been observed (see chapter 7). Such small dots are in addition predicted to posses per se a much higher radiative transition probability than larger ones, [9] and may serve as efficient sources of luminescence. However, the optical characterization of these small dots has not yet been performed and is a task for future work. This would include the challenge of capping such tiny Ge islands with silicon without loosing the dots by Ge segregation or intermixing. This task may also take advantage from the repulsive interaction between Ge and the C in the areas dividing adjacent Ge dots.

To overcome the randomness of the self-organized growth, other external parameters could be used. One parameter, that seems to be applicable to improve lateral order as well as size distribution of the ultra-small dots, is the substrate miscut angle. A miscut in [100] direction, that leads in the ideal case to a checkerboard like terrace distribution, in conjunction with the preferential c(4×4) formation at steps could favor the nucleation of single Ge dots on each square terrace, determining simultaneously the maximum size and the position of the dots.

For the larger GeC dots, where PL has already been detected, a reduction of the size distribution and an increase of lateral order would also be desirable to reduce the spread in energy levels and thus the optical line width. A popular method for this is the fabrication of quantum dot superlattices by stacking several dot layers separated by thin Si spacers. This method has been successfully applied to Ge and SiGe dots on bare Si [110, 111] and is mediated by the

strain fields that extend from the dots to the surface of the Si spacer layer. [112, 113] This strain fields lead to a vertical alignment of the dot positions in subsequent layers as well as to a gradual equilibration of the dots sizes. However, the only report available on this approach for the C-induced GeC dots [114] states that the presence of C prevents completely a vertical alignment. In contrast, preliminary results from our own experiments indicate, that vertical alignment is possible upon proper choice of C-content, Ge coverage and Si spacer thickness. So it seems worth to devote some further efforts to this question.

A completely different approach to the fabrication of well controlled nanostructures is confined nucleation, making use of dislocation patterns that arise during heteroepitaxial growth. For example this has been successfully realized by Brune *et al.* in the metallic system Ag on Pt(111), [115] where a regular hexagonal dislocation network occurs after the second ML of Ag deposition. Single Ag islands have been nucleated in each mesh of this network, leading to a regular arrangement and extremely narrow size distribution. A similar hexagonal dislocation network with a periodicity of about 4 nm can be fabricated on Si(111) after deposition of 3 ML Ge, using Sb as a surfactant. [116] This may serve as a template for a subsequent SiGe or Ge dot formation. A similar technique using the rectangular dislocation network of relaxed SiGe buffer layers, where Ge islands form preferentially and with very homogeneous size at the dislocation lines, [117] may also be worth to be considered. In the later case, however, the dots are usually large and not very dense. Anyway, both approaches are worth being considered for future work.

Concerning the experimental equipment, there is some potential for upgrading, too, in order to expand the possibilities and convenience of handling of the UHV-STM. First of all, a magazine to store several tunneling tips within the STM chamber would be desirable to reduce delays in case of the destruction of a tip. In addition, a substrate heater can be relatively easily installed in the STM chamber, as this had been foreseen during the design already, which would open up some new possibilities. The effect of annealing on the morphology of nanostructures could be observed in-situ, like coalescence of islands or intermixing. Furthermore the nucleation of nanostructures from the gas phase could be investigated, provided a simple gas inlet for e.g. germane is added, which may then be an alternative for growth in the regime of low coverages.

Although this work has been restricted to MBE grown samples, in the future advantage will be taken of all possibilities of the versatile UHV-growth system. Besides MBE, this includes the deposition by chemical vapor deposition in the UHV-CVD reactor, by plasma enhanced CVD, as well as etching experiments on nanostructures in a hydrogen plasma.

References

[1] L. Canham, *Phys. World* 5(3), 41 (1992).

[2] S. S. Iyer and Y. H. Xie, *Science* 260, 40 (1993).

[3] M. Arienzo, S. S. Iyer, B. S. Meyerson, G. L. Patton, and M. C. Stork, *Appl. Surf. Sci.* 48/49, 377 (1991).

[4] G. Abstreiter, *Phys. World* 5(3), 36 (1992).

[5] J. D. Cressler, *IEEE Spectrum* 32(3), 49 (1995).

[6] K. Brunner, O. G. Schmidt, W. Winter, K. Eberl, M. Gluck, and U. König, *J. Vac. Sci. Technol. B* 16(3), 1701 (1998).

[7] E. F. Steigmeier, R. Morf, D. Grützmacher, H. Auderset, B. Delley, and R. Wessicken, *Appl. Phys. Lett.* 69(27), 4165 (1996).

[8] S. Schuppler, S. L. Friedman, M. A. Marcus, D. L. Adler, Y. H. Xie, F. M. Ross, Y. J. Chabal, T. D. Harris, L. E. Brus, W. L. Brown, E. E. Chaban, P. F. Szajowski, S. B. Christman, and P. H. Citrin, *Phys. Rev. B* 52(7), 4910 (1995).

[9] B. Delley and E. F. Steigmeier, *Phys. Rev. B* 47(3), 1397 (1993).

[10] G. Abstreiter, P. Schittenhelm, C. Engel, E. Silveira, A. Zrenner, D. Meertens, and W. Jäger, *Semicond. Sci. Technol.* 11(11s), 1521 (1996).

[11] O. G. Schmidt, C. Lange, K. Eberl, O. Kienzle, and F. Ernst, *Appl. Phys. Lett.* 71(16), 2340 (1997).

[12] O. Leifeld, B. Müller, D. Grützmacher, and K. Kern, *App. Phys. A* 66(Suppl.), S993 (1998).

[13] O. Leifeld, D. Grützmacher, B. Müller, and K. Kern, in *Material Research Society Symposium Proceedings Vol. 533: Epitaxy and Applications of Si-based Heterostructures, 1998*, edited by E. A. Fitzgerald, D. C. Houghton, and P. M. Mooney, pp. 183-9, Materials Research Society (Warrendale, PA, 1998).

[14] F. K. Men and J. L. Erskine, *Phys. Rev. B* 50(15), 11200 (1994).

[15] R. I. G. Uhrberg, J. E. Northrup, D. K. Biegelsen, R. D. Bringans, and L. E. Swartz, *Phys. Rev. B* 46(16), 10251 (1992).

[16] H. Wang, f. L. Rong, and X. Wang, *Phys. Rev. B* 36(14), 7712 (1987).

[17] K. Miki, K. Sakamoto, and T. Sakamoto, *Appl. Phys. Lett.* 71(22), 3266 (1997).

[18] M. L. Shek, *Surf. Sci.* 414, 353 (1998).

[19] H.J. Güntherodt, R. Wiesendanger, *Scanning Tunneling Microscopy I, II and III* (Springer-Verlag, Berlin Heidelberg, 1992),

[20] F. Besenbacher, *Rep. Prog. Phys.* 59(12), 1737 (1996).

[21] H. Neddermeyer, *Rep. Prog. Phys.* **59**(6), 701 (1996).

[22] R. M. Feenstra, *Surf. Sci.* 965 (1994).

[23] R. Butz, H. Wagner, and K. Besocke, *Thin Solid Films* **183**, 339 (1989).

[24] O. G. Schmidt and K. Eberl, *Phys. Rev. Lett.* **80**(15), 3396 (1998).

[25] K. Besocke, *Surf. Sci.* **181**(1-2), 145 (1987).

[26] PRODAS 3.4, A. Schummers, (ProScope GmbH, D-52499 Baesweiler, 1996)

[27] P.M. Morse, K.U. Ingard, *Theoretical Acoustics* (Princeton University Press, Princeton - N. J., 1986), p. 216

[28] M. Amrein, in *Procedures in scanning probe microscopies*, (John Wiley&Sons, Chichester, U.K., 1998), p. 3.

[29] J. P. Ibe, P. J. Bey, S. L. Brandow, R. A. Brizzolara, N. A. Burnham, D. P. DiLella, K. P. Lee, C. R. K. Marrian, and R. J. Colton, *J. Vac. Sci. Technol. A* **8**(4), 3570 (1990).

[30] D. K. Biegelsen, F. A. Ponce, J. C. Tramontana, and S. M. Koch, *Appl. Phys. Lett.* **50**(11), 696 (1987).

[31] L. A. Hockett and S. E. Creager, *Rev. Sci. Instrum.* **64**(1), 263 (1993).

[32] J. Tersoff, *Phys. Rev. B* **41**(2), 1235 (1990).

[33] J. Tersoff and D. R. Hamann, *Phys. Rev. B* **31**(2), 805 (1985).

[34] J. Tersoff, *Phys. Rev. B* **39**(2), 1052 (1989).

[35] K. Takayanagi, Y. Tanishiro, M. Takahashi, and S. Takahashi, *J. Vac. Sci. Technol. A* **3**, 1502 (1985).

[36] W. Kern and D. Puotinen, *RCA Rev.* **31**, 187 (1970).

[37] U. Köhler, J. E. Demuth, and R. J. Hamers, *J. Vac. Sci. Technol. A* **7**(4), 2860 (1989).

[38] E. A. Wood, *J. Appl. Phys.* **35**, 1306 (1964).

[39] S. J. Jenkins and G. P. Srivastava, *Journal of Physics: Condensed Matter* **8**(36), 6641 (1996).

[40] O. L. Alerhand and E. J. Mele, *Phys. Rev. B* **35**(11), 5533 (1987).

[41] P. C. Kelires and E. Kaxiras, *J. Vac. Sci. Technol. B* **16**(3), 1687 (1998).

[42] R. J. Hamers, P. Avouris, and F. Bozso, *Phys. Rev. Lett.* **59**(18), 2071 (1987).

[43] D. J. Chadi, *Phys. Rev. Lett.* **59**(15), 1691 (1987).

[44] Y. W. Mo, R. Kariotis, B. S. Swartzentruber, M. B. Webb, and M. G. Lagally, *J. Vac. Sci. Technol. A* **8**(1), 201 (1990).

[45] B. S. Swartzentruber, *Phys. Rev. B* **55**(3), 1322 (1997).

[46] H. Rücker, M. Methfessel, E. Bugiel, and H. J. Osten, *Phys. Rev. Lett.* **72**(22), 3578 (1994).

[47] K. Brunner, W. Winter, and K. Eberl, *Phys. Bl.* **52**(12), 1237 (1996).

[48] A. R. Bean and R. C. Newman, *J. Phys. Chem. Solids* **32**, 1211 (1971).

[49] K. Brunner, W. Winter, K. Eberl, N. Jin-Phillipp, and F. Phillipp, *J. Cryst. Growth* **175/176**, 451 (1997).

[50] S. Zerlauth, H. Seyringer, C. Penn, and F. Schäffler, *Appl. Phys. Lett.* **71**(26), 3826 (1997).

[51] S. Zerlauth, C. Penn, H. Seyringer, G. Brunthaler, G. Bauer, and F. Schäffler, *J. Vac. Sci. Technol. B* **16**(3), 1679 (1998).

[52] H. J. Osten, J. Griesche, and S. Scalese, *Appl. Phys. Lett.* **74**(6), 836 (1999).

[53] H. J. Osten, M. Methfessel, G. Lippert, and H. Rücker, *Phys. Rev. B* **52**(16), 12179 (1995).

[54] P. C. Kelires and E. Kaxiras, *Phys. Rev. Lett.* **78**(18), 3479 (1997).

[55] T. Ide and T. Mizutani, *Phys. Rev. B* **45**(3), 1447 (1992).

[56] R. Tromp, R. J. Hamers, and J. E. Demuth, *Phys. Rev. Lett.* **55**(12), 1303 (1985).

[57] R. Butz and H. Lüth, *Surf. Sci.* **411**, 61 (1998).

[58] P. C. Kelires and J. Tersoff, *Phys. Rev. Lett.* **63**(11), 1164 (1989).

[59] O. Leifeld, D. Grützmacher, B. Müller, K. Kern, E. Kaxiras, and P. C. Kelires, *Phys. Rev. Lett.* **82**(5), 972 (1999).

[60] R. Car and M. Parrinello, *Phys. Rev. Lett.* **55**(22), 2471 (1985).

[61] I. Stich, R. Car, M. Parrinello, and S. Baroni, *Phys. Rev. B* **39**(8), 4997 (1989).

[62] P. C. Kelires, *Int. J. Mod. Phys. C* **9**(2), 357 (1998).

[63] A. A. Darhuber, J. Stangl, G. Bauer, P. Schittenhelm, and G. Abstreiter, *Thin Solid Films* **294**(1-2), 296 (1997).

[64] A. J. Steinfort, P. O. Scholte, A. Ettema, F. Tuinstra, M. Nielsen, E. Landemark, D. M. Smilgies, R. Feidenhansl, G. Falkenberg, L. Seehofer, and R. L. Johnson, *Phys. Rev. Lett.* **77**(10), 2009 (1996).

[65] U. Köhler, O. Jusko, B. Müller, H. M. Horn-von, and M. Pook, *Ultramicroscopy* **42-44**, 832 (1992).

[66] M. Hammar, F. K. LeGoues, J. Tersoff, M. C. Reuter, and R. M. Tromp, *Surf. Sci.* **349**(2), 129 (1996).

[67] F. M. Ross, J. Tersoff, and R. M. Tromp, *Phys. Rev. Lett.* **80**(5), 984 (1998).

[68] H. Sunamura, N. Usami, Y. Shiraki, and S. Fukatsu, *Appl. Phys. Lett.* **66**(22), 3024 (1995).

[69] P. Schittenhelm, M. Gail, K. Brunner, J. F. Nützel, and G. Abstreiter, *Appl. Phys. Lett.* **67**(9), 1292 (1995).

[70] G. Capellini, L. DiGaspare, F. Evangelisti, and E. Palange, *Appl. Phys. Lett.* **70**(4), 493 (1997).

[71] Y. W. Mo and M. G. Lagally, *J. Cryst. Growth* **111**, 876 (1991).

[72] M. Tomitori, K. Watanabe, M. Kobayashi, and O. Nishikawa, *Appl. Surf. Sci.* **76/77**, 322 (1994).

[73] Y. W. Mo, D. E. Savage, B. S. Swartzentruber, and M. G. Lagally, *Phys. Rev. Lett.* **65**(8), 1020 (1990).

[74] D. J. Eaglesham and M. Cerullo, *Phys. Rev. Lett.* **64**(16), 1943 (1990).

[75] D. E. Jesson, G. Chen, K. M. Chen, and S. J. Pennycook, *Phys. Rev. Lett.* **80**(23), 5156 (1998).

[76] J. Tersoff and R. M. Tromp, *Phys. Rev. Lett.* **70**(18), 2782 (1993).

[77] W. Seifert private communication, (1999).

[78] B. Vögeli, M. Kummer, and H. Von Känel, in *Material Research Society Symposium Proceedings Vol. 533: Epitaxy and Applications of Si-based Heterostructures, 1998*, edited by E. A. Fitzgerald, D. C. Houghton. and P. M. Mooney, pp. 209-14, Materials Research Society (Warrendale, PA, 1998).

[79] O. G. Schmidt, C. Lange, K. Eberl, O. Kienzle, and F. Ernst, *Thin Solid Films* **321**, 70 (1998).

[80] K. Eberl, O. G. Schmidt, S. Schieker, N. Jin-Phillipp, and F. Phillipp, *Solid-State Electron.* **42**(7-8), 1593 (1998).

[81] O. Leifeld, E. Müller, D. Grützmacher, B. Müller, and K. Kern, *Appl. Phys. Lett.* **74**(7), 994 (1999).

[82] O. Leifeld, R. Hartmann, E. Müller, E. Kaxiras, K. Kern, and D. Grützmacher, *Nanotechnology* **10**, 122 (1999).

[83] B. J. Spencer and J. Tersoff, in *Material Research Society Symposium Proceedings Vol. 399: Evolution of Epitaxial Structure and Morphology, 1995*, edited by A. Zangwill, D. E. Jesson, D. Chambliss, and R. Clarke, pp. 283-8, Materials Research Society (Warrendale, PA, 1996).

[84] E. Mateeva, P. Sutter, J. C. Bean, and M. G. Lagally, *Appl. Phys. Lett.* **71**(22), 3233 (1997).

[85] J. Weber and M. I. Alonso, *Phys. Rev. B* **40**(8), 5683 (1989).

[86] Landolt-Börnstein, *Numerical data and functional relationships in science and technology* (Springer-Verlag, Berlin, 1982), Vol. 17(a) and 17(b)

[87] K. Nakagawa and M. Miyao, *J. Appl. Phys.* **69**(5), 3058 (1991).

[88] S. Fukatsu, K. Fujita, H. Yaguchi, Y. Shiraki, and R. Ito, *Appl. Phys. Lett.* **59**(17), 2103 (1991).

[89] D. Grützmacher, R. Hartmann, P. Schnappauf, U. Gennser, E. Müller, D. Bächle, and A. Dommann, *Thin Solid Films* **321**, 26 (1998).

[90] S. Fukatsu, H. Sunamura, Y. Shiraki, and S. Komiyama, *Thin Solid Films* **321**, 65 (1998).

[91] D. Grützmacher, R. Hartmann, O. Leifeld, U. Gennser, C. David, E. Müller, and J.-C. Panitz, in *Proceedings of SPIE 3630: Silicon-based Optoelectronics* edited by D. C. Houghton and E. A. Fitzgerald, pp. 171-82, The Society of Photo-Optical Instrumentation Engineers (Bellingham, WA, 1999).

[92] R. Hartmann, Growth and Characterization of semiconductor nanostructures in the system Si-Ge-C. Thesis, ETH Zürich, (1998),

[93] T. Schmidt, K. Lischka, and W. Zulehner, *Phys. Rev. B* **45**(16), 8989 (1992).

[94] J. Pietzsch and T. Kamiya, *Applied Physics A (Solids and Surfaces)* **42**, 91 (1987).

[95] R. Apetz, L. Vescan, A. Hartmann, C. Dieker, and H. Lüth, *Appl. Phys. Lett.* **66**(4), 445 (1995).

[96] F. Liu and M. G. Lagally, *Phys. Rev. Lett.* **76**(17), 3156 (1996).

[97] B. Müller, O. Jusko, G. J. Pietsch, and U. Köhler, *J. Vac. Sci. Technol. B* **10**(1), 16 (1992).

[98] G. Ehrlich and F. G. Hudda, *J. Chem. Phys.* **44**, 1039 (1999).

[99] R. L. Schwoebel and E. J. Shipsey, *J. Appl. Phys.* **37**, 3682 (1966).

[100] Y. W. Mo, J. Kleiner, M. B. Webb, and M. G. Lagally, *Phys. Rev. Lett.* **66**(15), 1998 (1991).

[101] J. A. Venables, G. D. T. Spiller, and M. Hanbucken, *Rep. Prog. Phys.* **47**, 399 (1984).

[102] J. G. Amar, F. Family, and M. L. Pui, *Phys. Rev. B* **50**(12), 8781 (1994).

[103] J. G. Amar and F. Family, *Phys. Rev. Lett.* **74**(11), 2066 (1995).

[104] M. C. Bartelt and J. W. Evans, *Phys. Rev. B* **54**(24), R17359 (1996).

[105] M. C. Bartelt and H. M. Evans, *Phys. Rev. B* **49**(19), 12675 (1992).

[106] W. Theis and R. M. Tromp, *Phys. Rev. Lett.* **76**(15), 2770 (1996).

[107] J. H. Zhu, K. Brunner, and G. Abstreiter, *Appl. Phys. Lett.* **73**(5), 620 (1998).

[108] K. M. Chen, D. E. Jesson, S. J. Pennycook, M. Mostoller, T. Kaplan, T. Thundat, and R. J. Warmack, *Phys. Rev. Lett.* **75**(8), 1582 (1995).

[109] B. S. Swartzentruber, N. Kitamura, M. G. Lagally, and M. B. Webb, *Phys. Rev. B* **47**(20), 16432 (1993).

[110] C. Teichert, M. G. Lagally, L. J. Peticolas, J. C. Bean, and J. Tersoff, *Phys. Rev. B* **53**(24), 16334 (1996).

[111] P. Schittenhelm, C. Engel, F. Findeis, G. Abstreiter, A. A. Darhuber, G. Bauer, A. O. Kosogov, and P. Werner, *J. Vac. Sci. Technol. B* **16**(3 (May June)), 1575 (1998).

[112] J. Tersoff, C. Teichert, and M. G. Lagally, *Phys. Rev. Lett.* **76**(10), 1675 (1996).

[113] F. Liu, S. E. Davenport, H. M. Evans, and M. G. Lagally, *Phys. Rev. Lett.* **82**(12), 2528 (1999).

[114] O. G. Schmidt, S. Schieker, K. Eberl, O. Kienzle, and F. Ernst, *Appl. Phys. Lett.* **73**(5), 659 (1998).

[115] H. Brune, M. Giovannini, K. Bromann, and K. Kern, *Nature* **394**, 451 (1998).

[116] B. Voigtländer and A. Zinner, *Surf. Sci.* **351**, L233 (1996).

[117] E. V. Pedersen, F. Jensen, S. Y. Shiryaev, J. W. Petersen, H. J. Lundsgaard, and L. A. Nylandsted, *Thin Solid Films* **321**, 92 (1998).

Acknowledgments

I would like to express my gratitude to all members of the Institute for Experimental Physics at the EPFL, and to the members of the Laboratory for Micro- and Nanotechnology at the Paul Scherrer Institute for their support and the creation of the friendly environment, in which I could accomplish this Ph.D. thesis. Nevertheless, there are many persons to whom I owe special thanks:

First of all I like to thank Prof. Dr. Klaus Kern, the director of my thesis, for giving me the opportunity to work in his group and at the EPFL and for guiding me throughout the entire thesis. Especially during the first year the profound STM experience of the group was indispensable for the fast realization of the new microscope.

I thank Dr. Jens Gobrecht, the leader of the Micro and Nanostructures Lab at PSI, for providing the excellent working conditions at the LMN.

I am grateful to Dr. Detlev Grützmacher for supervising the experimental part of the work. Our valuable discussions and his constructive and encouraging advice have contributed a lot to this work. Although very charged, he was never reluctant to help out in the lab for maintenance and repair of the epitaxy system.

Dr. Bert Müller, who supervised my work during the time at EPFL, continued to take care of my work, although remotely, until the end, which I highly appreciate. I also thank him for spending quite some time during the preparation of the manuscript of my thesis and for thoroughly reading and correcting it.

Next, I have to gratefully acknowledge the contribution of Prof. Dr. Efthimios Kaxiras, who carried out the computer simulations of chapter 5.

Rainer Hartmann, who has introduced me to the secrets of the MBE machine and who has done most of the PL measurements, has helped a lot to complete this work, which I appreciate very much.

Furthermore I would like to thank Dr. Elisabeth Müller at the ETHZ, our TEM expert, for providing lots of high resolution cross-sectional TEM images of our samples.

Thanks also to the technical staff at the EPFL and the PSI, especially André Guisolan and Michel Fazan at the IPE, Urs Rimann, Fredi Glaus, Thomas Neiger at the LMN for maintaining the necessary infrastructure for my experiments, Teresa Mezzacasa and Dieter Bächle for the cleanroom processes and Jürgen Mahler for the PC support.

I also appreciate the fast and reliable work of the PSI workshop, who build the pieces for the STM in a very short time.

Curriculum vitae

Personal

Name:	Oliver Leifeld
Address:	Schartenstrasse 127
	5430 Wettingen
	Switzerland
Date of birth:	09.07.1970, Paderborn, Germany
Nationality:	German

Education

Aug. 1976 - July 1980	Primary school in Paderborn
Aug. 1980 - May 1989	Secondary school, städtisches Pelizaeus-Gymnasium, Paderborn
June 1989 - Sept. 1990	military service
Oct. 1990 - Jan. 1996	Study of physics at the Faculty of Physics, University of Paderborn (Universität-Gesamthochschule Paderborn)
	Diploma thesis in the group for Physics and Technology of Optoelectronic Semiconductors, Prof. Dr. Klaus Lischka, entitled: "Molekularstrahlepitaxie von Cl-dotiertem n-ZnSe" (Molecular beam epitaxy of chlorine-doped n-ZnSe)
since April 1996	Ph. D. thesis at the Swiss Federal Institute of Technology Lausanne (Ecole Polytechnique Fédérale de Lausanne), 1015 Lausanne, Switzerland, Department of Physics, Institute of Experimental Physics, group of Prof. Dr. Klaus Kern, collaborating with:
	Laboratory of Micro- and Nanotechnology, Paul Scherrer Institute, 5232 Villigen-PSI, Switzerland

List of Publications

1. B. Buda, O. Leifeld, S. Völlmeke, F. Schmilgus, D. J. As, D. Schikora, and K. Lischka, "Initial roughness and relaxation behaviour of MBE grown ZnSe/GaAs", *Acta Physica Polonica A* **90**(5), 997 (1996).

2. B. Buda, C. Wang, W. Wrede, O. Leifeld, D. J. As, D. Schikora, and K. Lischka, "The influence of the early stage of ZnSe growth on GaAs(001) on the defect-related luminescence", *Semicond. Sci. Technol.* **13**(8), 921 (1998).

3. O. Leifeld, B. Müller, D. Grützmacher, and K. Kern, "A UHV STM for in situ characterization of MBE/CVD growth on 4-inch wafers", *App. Phys. A* **66**(Suppl.), S993 (1998).

4. O. Leifeld, D. Grützmacher, B. Müller, and K. Kern, "Ge-Quantum Dots on Si(001) tailored by carbon predeposition", in *Material Research Society Symposium Proceedings Vol. 533: Epitaxy and Applications of Si-based Heterostructures, 1998*, edited by E. A. Fitzgerald, D. C. Houghton, and P. M. Mooney, pp. 183-9, Materials Research Society (Warrendale, PA, 1998).

5. O. Leifeld, D. Grützmacher, B. Müller, K. Kern, E. Kaxiras, and P. C. Kelires, "Dimer pairing on the C-alloyed Si(001) surface", *Phys. Rev. Lett.* **82**(5), 972 (1999).

6. O. Leifeld, E. Müller, D. Grützmacher, B. Müller, and K. Kern, "In situ scanning tunneling microscopy study of C-induced Ge quantum dot formation on Si(100)", *Appl. Phys. Lett.* **74**(7), 994 (1999).

7. D. Grützmacher, R. Hartmann, O. Leifeld, U. Gennser, C. David, E. Müller, and J.-C. Panitz, "Optical properties of Si-Ge-C nanostructures deposited by MBE", in *Proceedings of SPIE 3630: Silicon-based Optoelectronics* edited by D. C. Houghton and E. A. Fitzgerald, pp. 171-82, The Society of Photo-Optical Instrumentation Engineers (Bellingham, WA, 1999).

8. O. Leifeld, R. Hartmann, E. Müller, E. Kaxiras, K. Kern, and D. Grützmacher, "Self organized growth of Ge quantum dots on Si (001) substrates induced by sub-monolayer C coverages", *Nanotechnology* **10**, 122 (1999).